Preparations, Characteristics, and Applications of Carbon-based Nanomaterials

Thesis written by

Lars Weber

to obtain the Doctor rerum naturalium (Dr. rer. nat.) at the

Technische Universität Ilmenau

Ilmenau, Germany, 2009

urn:nbn:de:gbv:ilm1-2010000061

In Dankbarkeit gewidmet meinen Eltern –

denen ich diese Ausbildung verdanke.

Abstract

Preparations, characteristics, and applications of dimeric fullerene oxides and well-aligned multi-walled carbon nanotube (MWCNT) arrays – both being carbon-based nanostructured materials – are reported.

Directed and specific syntheses and isolations of preparative amounts of dimeric fullerene oxides using conventional laboratory methods are presented. Oxidative and thermal properties, electronic absorption properties, and electron acceptor strength of dimeric fullerene oxides are given. The application of dimeric fullerene oxides to organic photovoltaics is reported.

Synthesis and electrochemical induced purification of well-aligned MWCNT arrays is presented. Capacitive and electron transfer (faradaic) properties of well-aligned MWCNT array electrodes are given. The application of well-aligned MWCNT array electrodes to non-enzymatic glucose detection is reported.

Kurzzusammenfassung

Es wird über Herstellungen, Eigenschaften und Anwendungen von dimeren Fullerenoxiden und von Anordnungen senkrecht ausgerichteter, mehrwandiger Kohlenstoffnanoröhren – beides nanostrukturierte Kohlenstoffmaterialien – berichtet.

Direkte und spezifische Synthesen sowie Isolationen von dimeren Fullerenoxiden in präperativen Mengen werden beschrieben. Oxidative und thermische Stabilität, elektronische Absorptionseigenschaften und Elektronenakzeptorstärke von dimeren Fullerenoxiden werden erörtert. Die Verwendung von dimeren Fullerenoxiden in Plastiksolarzellen wird beschrieben.

Die Herstellung und elektrochemische Reinigung von Anordnungen senkrecht ausgerichteter, mehrwandiger Kohlenstoffnanoröhren werden erläutert. Kapazitive Eigenschaften und Elektronenübertragungseigenschaften von Elektroden basierend auf solchen Anordnungen werden erörtert. Die nicht-enzymatische Glukosedetektion mittels solcher Kohlenstoffnanoröhren-Elektroden wird beschrieben.

List of Publications

Parts of this work have been published as scientific papers in peer-refereed journals and as scientific papers, lectures, and posters in scientific conferences.

Peer-refereed Papers

Lars Weber, Loredana Carta-Abelmann, Uwe Ritter, Peter Scharff, *Preparation and Characterization of the Dimeric C_{70} Fullerene Oxide $C_{140}O$*, Fullerenes, Nanotubes and Carbon Nanostructures, 16 (2008) 258-271.

Lars Weber, Markus Reinmöller, Uwe Ritter, *Diazoalkane Addition Reaction on the Fullerene Dimer $C_{120}O$ and Characterization of the Resulting Mono-adduct*, Carbon – Science and Technology, 1 (2008) 9-12.

Lars Weber, Steffi Sensfuss, Uwe Ritter, Peter Scharff, *Monocyclopropanated Fullerene Dimer $C_{120}O$ and Its Application in a Bulk Heterojunction Solar Cell*, Chemistry Letters, 37 (2008) 750-751.

Lars Weber, Steffi Sensfuss, Uwe Ritter, Peter Scharff, *Preparation, Characterization, and Application of Dimeric Fullerene-Oxides*, Fullerenes, Nanotubes and Carbon Nanostructures, 17 (2009) 187-207.

Lars Weber, Katharina Klöckner, Uwe Ritter, Peter Scharff, V*alidation of Doubling Exponent Models for the Impedance of Well-Aligned MWCNT Array Electrodes*, Russian Journal of Electrochemistry, (2009) accepted for publication.

Lars Weber, Uwe Ritter, Peter Scharff, *Electrochemical Characteristics of Well-aligned MWCNT Array Electrodes*, Fullerenes, Nanotubes and Carbon Nanostructures (2009) accepted for publication.

Conference Reports

Lars Weber, Steffi Sensfuss, Alexander Konkin, Uwe Ritter, Peter Scharff, *Oligomeric Fullerene Derivatives for Photoactive Layers of High Supra-Molecular Order*, Lecture and Scientific Paper, Proceedings of the International Symposium on Technologies for Polymer Electronics (TPE 08), Rudolstadt, Germany (May 20-22, 2008) 93-97.

Lars Weber, Uwe Ritter, Peter Scharff, *Non-enzymatic Glucose Detection Using MWCNT Array Electrodes*, Lecture, Proceedings of the German-Ukrainian Symposium on Nanoscience and Nanotechnology, Essen, Germany (October 22-25, 2008) 57.

Lars Weber, Uwe Ritter, Peter Scharff, *Non-enzymatic Glucose Detection Using MWCNT Array Electrodes*, Poster, Proceedings of the Ninth International Conference on the Science and Application of nanotubes (NT08), Montpellier, France (June 29-July 4, 2008) 425.

Lars Weber, Uwe Ritter, Peter Scharff, *MWCNT Array Electrodes in Non-enzymatic Detection of Biomolecules*, Poster, E-MRS 2009 Spring Meeting, Strasbourg, France (June 8-12, 2009).

Acknowledgements

This work was realized at the Department of Chemistry of the Technische Universität Ilmenau. I thank all people who contributed to the success of this work.

Many thanks go to Univ.-Prof. Dr. rer. nat. habil. Dr. h.c. Prof. h.c. Peter Scharff for the chance to work in his department on exciting and future-orientated research topics.

My special thanks go to Priv.-Doz. Dr. rer. nat. habil. Uwe Ritter for his unfailing support, substantial interest, and freedom of job design.

Sincere, heartfelt thanks go to Susann Günther, Sabine Heusing, Katrin Risch, Doreen Schneider, and Carmen Siegmund for pulling out all the stops at the laboratory.

Warm thanks go to Katharina Klöckner and Markus Reinmöller for their creativity and commitment.

Cordial thanks go to Dr. rer. nat. Steffi Sensfuss from the TITK in Rudolstadt and Dr. rer. nat. Alexander Konkin from the ZMN in Ilmenau for their patience and fruitful cooperation.

Thank you,

Lars Weber

Table of Contents

List of Abbreviations

Abbreviation	Meaning
BHJ	bulk hetero junction
CNT	carbon nanotube
CPE	constant phase element
CV	cyclic voltammetry, cyclic voltammogram
CVD	chemical vapor deposition
EIS	electrochemical impedance spectroscopy
Fc/Fc^+	ferrocene/ferricenium redox couple
HOMO	highest occupied molecular orbital
HPLC	high pressure liquid chromatography
IR	infra-red
LESR	light-induced electron spin resonance
LUMO	lowest unoccupied molecular orbital
M3EH-PPV	semiconducting polymer (*Figure 1.14*)
MALDI-TOF	matrix assisted laser desorption/ionization-time of flight
MS	mass spectrometry
MWCNT	multi-walled carbon nanotube
NMR	nuclear magnetic resonance
ODCB	ortho-dichlorobenzene
P3HT	semiconducting polymer (*Figure 1.14*)
RT	room temperature
SEM	scanning electron microscopy
SWCNT	single-walled carbon nanotube
TEM	trans electron microscopy
TGA	thermogravimetric analysis
UV-vis	ultraviolet-visible

Lists of Symbols and Indices

Latin Symbols

Symbol	Meaning
C	capacitance [F]
E^1_{red}	first half-wave reduction potential [V vs. Fc/Fc^+]
f	frequency [Hz]
I	voltammetric current [A]
Q	constant of a CPE [F]
q	constant, which is related to a CPE
R	resistance [Ohm]
r	resistance per unit length [Ohm/m]
W	Warburg diffusional element [Ohm $s^{0.5}$]
Z	Impedance [Ohm], Re(Z): real part; Im(Z): imaginary part

Greek Symbols

Symbol	Meaning
α	exponent of a CPE [-]
β	exponent of transition line models [-]
ν	sweep rate [mV/s]
ω	angular frequency [rad/s]

Indices

Symbol	Meaning
a	anodic
c	cathodic
int	internal of MWCNT arrays
s	solution

1. Introduction

Nanoscience and nanotechnologies have huge potential to bring benefits in areas such as electronics, optoelectronics, information technology, biotechnology, and medicine. Nanoscience and nanotechnologies are attracting rapidly increasing investments from governments and from businesses in many parts of the world. The total global investment in nanotechnologies is currently around €5 billion, €2 billion of which comes from private sources. The worldwide market for nanotechnologies is predicted to be $1 trillion by 2015 [Roy04].

Nanoscience and nanotechnologies encompass a wide range of materials, tools, techniques, approaches, and potential applications that cut across many scientific disciplines, from chemistry and physics to biology, engineering, and medicine. Although there is no sharp distinction between them, nanosciene and nanotechnologies are commonly defined as follows [Roy04]:

- Nanoscience is the study of phenomena and manipulation of materials at atomic, molecular and macromolecular scales, where properties differ significantly from those at a larger scale.
- Nanotechnologies are the design, characterization, production, and application of structures, devices, and systems by controlling shape and size at the nanometer scale.

Two principal factors cause the properties of nanostructured materials to differ significantly from other materials. Firstly, nanomaterials have a relatively larger

surface area compared to the same mass of material produced in a larger form. This can make materials more chemically reactive and affect their mechanical or electrical properties. Secondly, quantum effects can begin to dominate the behavior of matter at the nanoscale affecting the optical, electrical, and magnetic characteristics of materials [Roy04].

Nanostructured materials can be nanoscale in all three dimensions, in two dimensions or in one dimension. Examples for three dimensional nanomaterials are nanoparticles, quantum dots, dendrimers, and fullerens. Two dimensional nanomaterials are for instance biopolymers, nanowires, inorganic nanotubes, and carbon nanotubes (CNTs). Finally, organic thin films as well as engineered layers and surfaces are examples for one-dimensional nanomaterials [Bon03, Roy04].

In this work, preparations, characteristics, and applications of dimeric fullerene oxides as well as well-aligned multi-walled carbon nanotube (MWCNT) arrays – both carbon-based nanostructured materials – were developed:

- Dimeric fullerene oxides were synthezised and isolated, physicochemically characterized, and applied to organic photovoltaics. In chapter 1.1, the area of research is introduced. Experimental procedures are explained in chapter 2. Finally, in chapter 3.1, research results are discussed in detail.
- Well-aligned MWCNT array electrodes were fabricated, electrochemically characterized, and applied to electrochemical non-enzymatic glucose detection. In chapter 1.2, the field of research is presented. Experimental procedures are given in chapter 2. Finally, research results are extensively considered in chapter 3.2.

To put this work into context, structures, properties, and potential applications of fullerenes and carbon nanotubes are briefly summarized in the following paragraphs.

Fullerenes

Fullerenes are a family of carbon allotropes, molecules composed entirely of carbon, in the form of hollow spheres. Fullerenes are built up of fused pentagons and hexagons. The pentagons provide curvature. The smallest stable, and almost abundant fullerene is C_{60} (*Figure 1.1*). The next stable homologue is C_{70} (*Figure 1.1*) followed by the higher fullerenes C_{74}, C_{76}, C_{78}, C_{80}, C_{82}, C_{84}, and so on. The building principle of fullerenes is a consequence of the Euler theorem, which says that for the closure of each spherical network of n hexagons, 12 pentagons are required, with the exception of n = 1.

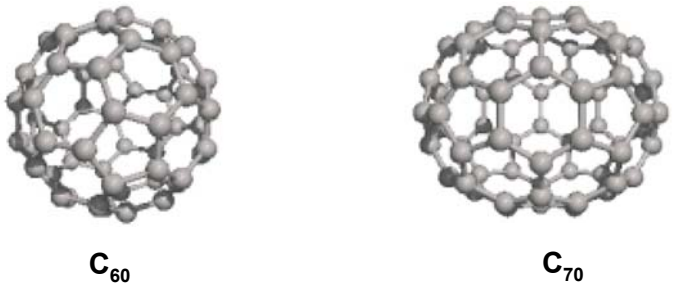

Figure 1.1. *Chemical structures of the fullerenes C_{60} and C_{70} [Roy04].*

Production routes to fullerenes include vaporization of graphite (e.g. by resistive or arc heating), sooting flames, and pyrolysis of hydrocarbons. Besides a fullerene fraction, the raw product of fullerene productions contains by-products such as soot, slag, and further carbon structures. Fullerene fractions can be isolate from product

mixtures either by sublimation or by extraction. To separate fullerenes from a fullerene fraction, chromatographic methods are used.

Fullerene chemistry is exceedingly rich and comprises nucleophilic-, electrophilic-, radical-, and cyclo-additions, polymerization, hydrogenation, halogenation, as well as the formation of transition metal complexes, heterofullerens and endohedral fullerenes.

Due to their intrinsic properties, fullerenes have great potential as building blocks for nanotechnological applications. Fullerenes show an extremely high hardness, which is attractive for protective coatings. Fullerenes are chemically reactive and can be linked to polymer structures to create new copolymers with specific physical and mechanical properties. Fullerenes can also be used as polymer additive to make composites and modify physical properties and performance characteristics of polymers. Fullerenes are powerful antioxidants, react readily and at a high rate with free radicals, and consequently have potential in physiological and non-physiological applications, where oxidation and radical processes are destructive (e.g. cell damage, food spoilage, plastics deterioration, and metal corrosion). The size of C_{60} is similar to many biological active molecules, including drugs, which gives C_{60} potential as a foundation for creating a variety of biologically active variants for medical applications (such as drug delivery or enzyme/protein blocker). Fullerenes have shown considerable potential as catalysts, non-metallic magnetic and superconductive material. Due to their intrinsic electrical properties, fullerenes have significant potential for use in fuel cells, batteries, photodetectors, and organic electronics such as organic field effect transistors (OFETS) and organic photovoltaics (OVP).

Structures, production, chemical and physical properties, as well as potential applications of fullerenes have been comprehensively summarized in well-written text books [Kad00, Hir05, Fow07, Lan07A, Lan07B].

Carbon Nanotubes

Carbon nanotubes (CNTs) are molecular-scale tubes of graphitic carbon. There are two types of CNT: single-walled carbon nanotubes (one tube) and multi-walled carbon nanotubes (several concentric tubes). Both of these are typically a few nanometers in diameter and several micromeres (10^{-6} m) to centimeters long. *Figure 1.2* illustrates single-walled nanotubes (SWCNTs) and multi-walled nanotubes (MWCNTs) [Roy04].

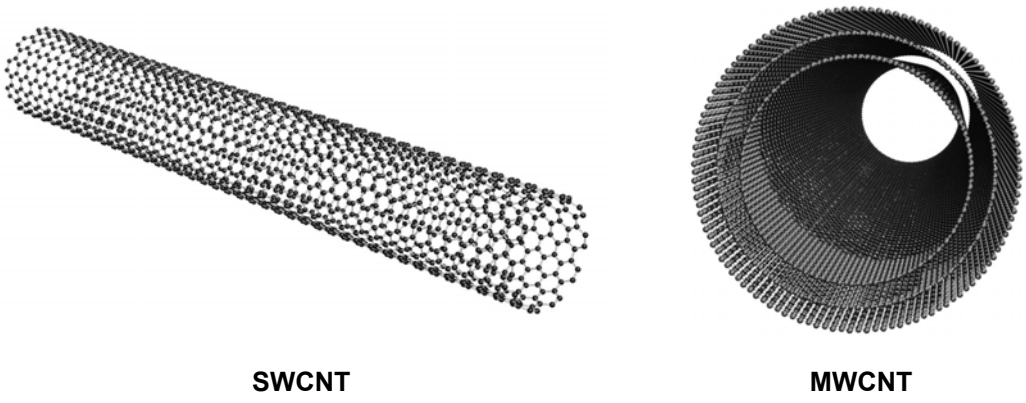

Figure 1.2. *Schematic of a single-walled carbon nanotube (SWCNT) and a multi-walled carbon nanotube (MWCNT) [Roy04].*

CNTs can be produced by chemical vapor deposition (CVD), arc discharge and laser ablation techniques. Each method allows the synthesis of bulk amounts of CNT material consisting of entangled, bundled, and crystalline CNT structures. Self-

assembled, vertically aligned CNT architectures directly grown on substrates with control on the nanometer scale can only be synthesized with CVD techniques [Bra09].

As-synthesized CNTs contain carbonaceous impurities and catalyst residue. Purification methods of CNTs can basically be classified into two categories, namely chemical and physical. The chemical method purifies CNTs based on selective oxidation, wherein carbonaceous impurities are oxidized at a faster rate than CNTs, and the dissolution of metallic impurities by acids. Chemical oxidation includes the most frequently used gas phase (using air, O_2, Cl_2, H_2O, etc.) and liquid phase oxidation (using acid treatment and refluxing, etc.), as well as the rarely applied electrochemical oxidation. The physical method separates CNTs from impurities based on the differences in their physical size, aspect ratio, gravity, and magnetic properties. Predominantly, the merits of chemical and physical purification are combined in multi-step purifications [Hou08].

CNTs are characterized by low density, large aspect ratio, high tensile strength, high elastic modulus, and high heat conductivity. In addition, CNTs are chemically modifiable (e.g. by covalent tip, sidewall and defect functionalization, endohedral and non-covalent functionalization) and electrocatalytically active. Depending on the helicity of the tubes, single CNTs are either electrically conducting or semi-conducting. For statistical reasons, in MWCNTs electrical conductivity normally dominates.

Due to their intrinsic properties, CNTs are attractive for various applications including electronics, field emitter, composites, sensors, probes, energy storage, and biomedicine [Bra09].

Structures, production, chemical and physical properties, as well as possible applications of CNTs have been well summarized in excellent text books [Sai98, Dre01, Sma01, Rei04, Mey05, Rot05, Con06, Loi06, Hie08, Jor08, Har09].

1.1. Dimeric Fullerene Oxides

In this chapter, the research area of dimeric fullerene oxides is briefly discussed and the preparations, characteristics, and applications of dimeric fullerene oxides developed in this work are elucidated and put into context.

Dimeric fullerene oxides can be classified as fullerene dimers. In a stricter sense, fullerene dimers are molecules, in which two fullerene cages are directly covalently linked. Examples of C_{60}-based dimers are shown in *Figure 1.3* and include:

- the cyclobutane-like bridged dimer C_{120} [Kom98],
- heteroatom-bridged dimers sharing a five-membered ring such as the furan-like bridged, dimeric fullerene oxide $C_{120}O$ [Leb95, Smi95], the methylene-bridged dimer $C_{120}CH_2$ [Smi95], the silicon bridged-dimer $C_{120}SiPh_2$ (Ph = phenyl, C_6H_5) [Fuj02A], or the germanium-bridged dimer $C_{120}GePh_2$ [Mur03],
- heteroatom-bridged dimers sharing a cyclobutane ring and two indirect intercage links (that is, the dimers share two five-membered rings) such as the bis-furanoid bridged dimer $C_{120}O_2$ [Gro97A, Gro98], the bis-methylene-bridged dimer $C_{120}C_2H_4$ [Dra00A], or the furan-cyclobutane-thiophene bridged dimer $C_{120}OS$ [Gie99],
- exo- and endohedral functionalized C_{120} dimers such as R-C_{61}-(1,3 Ph)-C_{61}-R (R = $(OC_6H_3)_2$) or $^3He@C_{120}C(CO_2C_2H_5)_2$, [Fuj01A, Fuj01B, Fuj02B, Kno00, Kom00A], as well as

- single-bonded dimers such as $RC_{60}C_{60}R$ (R = H, halo, alkyl, fluoroalkyl) [Sch95, Osa96, Yos99] and aza[60]fullerenyl dimers [Nub96].

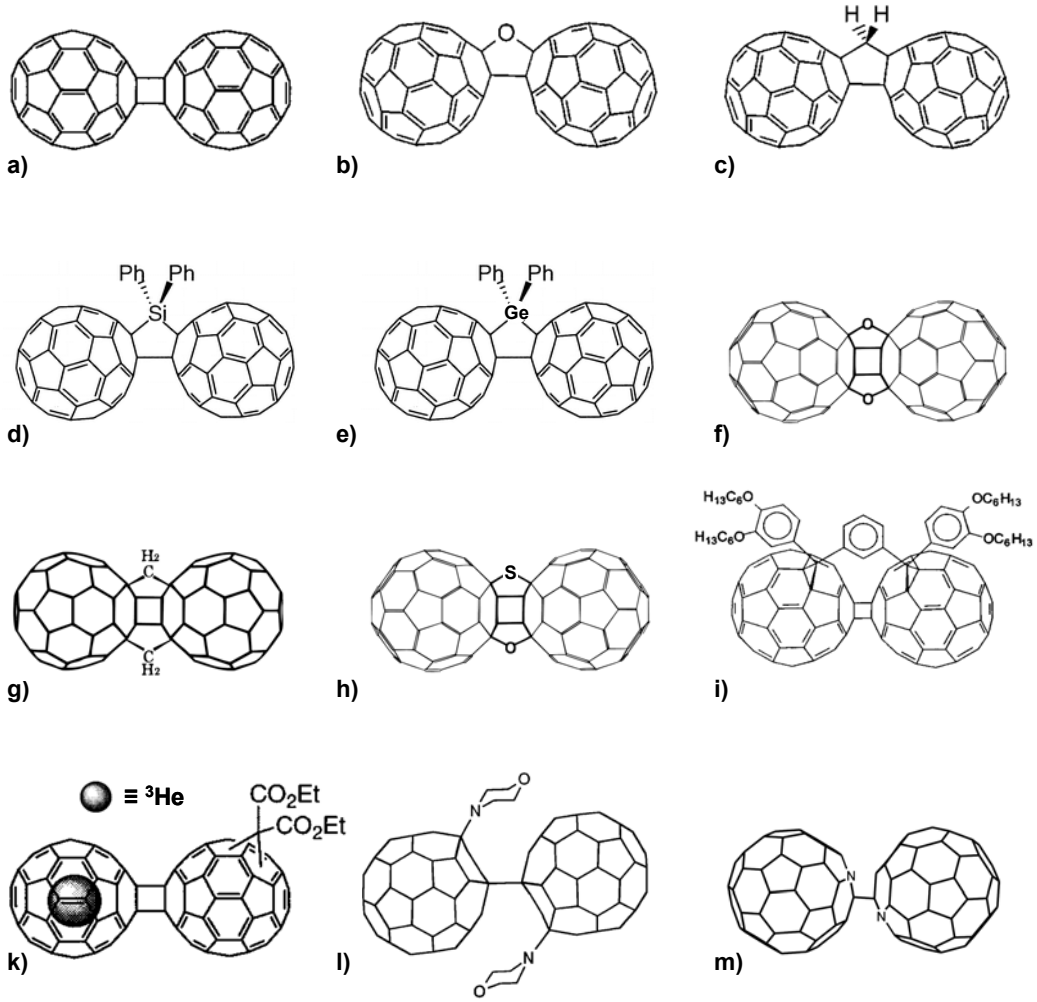

Figure 1.3. *C_{60}-based dimers: a) C_{120}, b) $C_{120}O$, c) $C_{120}CH_2$, d) $C_{120}SiPh_2$ (Ph = C_6H_5), e) $C_{120}GePh_2$, f) $C_{120}O_2$, g) $C_{120}C_2H_4$, h) $C_{120}OS$, i) R-C_{61}-(1,3 Ph)-C_{61}-R (R = $(OC_6H_3)_2$), k) $^3He@C_{120}C(CO_2C_2H_5)_2$, l) ($C_{60}$-Morpholine)$_2$, m) aza[60]fullerenyl dimer.*

Examples of C_{70}-containing dimers are shown in *Figure 1.4* and comprise:

- the cyclobutane-like bridged dimers C_{130} [Kom00B, Tag02] and C_{140} [Leb00A, Leb00B, For02],
- the furan-like bridged, dimeric fullerene oxides $C_{130}O$ [Eis98A, Tak98, Tak01] and $C_{140}O$ [Kud02], as well as
- single-bonded dimers like aza[70]fullerenyl dimers [Has97].

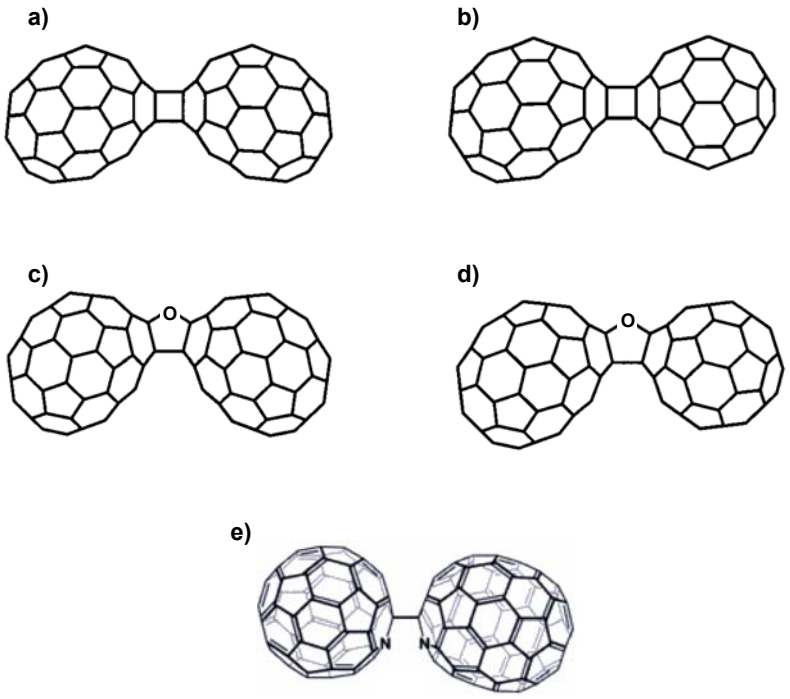

Figure 1.4. *C_{70}-containing dimers: a) C_{140}, b) C_{130}, c) $C_{140}O$, d) $C_{130}O$, e) aza[60]fullerenyl dimer.*

The interest manifested in fullerene dimers is related to their utilization in fullerene polymer science [Ekl00] and organic electronics (this work), to their use as systems for investigating intra-molecular charge transfer [Bal96] and interaction between

electron spins in molecules [Zha06], and to their exploitation as precursor for further fullerene based materials [Gro97B, Gro97C].

The relatively simple material class of fullerene dimers proved to be rather difficult to study owing, in general, to the low solubility of fullerene dimers. The extensive fundamental research on C_{60} fullerene dimers including preparation, structural characteristics, physicochemical properties, and chemistry of dimeric fullerens has been well reviewed [Shi04, Seg00]. As yet, fullerene dimers were not brought to applications.

In addition to the classification as fullerene dimers, dimeric fullerene oxides can be regarded as fullerene oxide structures. Examples of fullerene oxide structures are shown in *Figure 1.5* and include:

- monomeric fullerene oxides such as $C_{60}O_n$ or $C_{70}O_n$ (n = 1-6) [Hey06],
- dimeric fullerene oxides such as $(C_{60})_2O_n$ (n = 1-10) [Leb95, Smi95, Gro98, Res01], $C_{60}C_{70}O_n$ (n = 2-3) [Eis98A, Tak98, Tak01], $(C_{70})_2O_n$ (n = 1-3) [Jaf99, Kud02, Zha04],
- trimeric fullerene oxides such as $(C_{60})_3O_n$ (n = 2-6) [Den96, Gro96, Gro97C],
- linear, un-branched oligomeric $(C_{60}O)_n$ fullerene oxides [Bri05, Khl05],
- highly complex and topologically disordered polymeric fullerene oxide networks of the type $(C_{60})_mO_n$ [Zha03, Khl05, Win06], as well as
- odd- and even-numbered fullerene oxide structures with probably modified cage structures such as $C_{58}O_n$ (n = 1, 2) [Den95, Pen97, Res01], $C_{59}O_n$ (n = 1-4) [Den95, Pen97, Res01], $C_{68}O_n$ (n = 1-3) [Den96], $C_{118}O_n$ (n = 1, 3) [Gro96,

Gro97C], $C_{119}O_n$ (n = 2-4) [Res01], $C_{178}O_3$ [Gro96], and $C_{179}O_2$ [Gro96, Gro97C].

The most stable fullerene oxide structures show [6,6] closed ring junctions and intact fullerene moieties. The most stable monomeric fullerene oxides are methanofullerenes showing [6,6] closed epoxide structures (epoxyfullerenes, *Figure 1.5 a) and c)-g)*) [Hey06]. The proposed structures of the most stable oligomeric and polymeric fullerene oxides show intact fullerene cages connected by furanoid oxo-bridges (*Figure 1.5 h), l), and m)*) [Leb95, Smi95, Den96, Gro97A, Eis98A, Eis98B, Gro98, Kra98A, Kra98B, Kud02, Bri05, Khl05] and potentially additionally functionalised by epoxide groups (*Figure 1.5 i) and k)*) [Gro98]. Fullerene oxide structures showing open [5,6] ring junctions (homofullerenes, fulleroides, *Figure 1.5 b)*) are less stable and can be transformed to fullerene epoxides by irradiation [Hey06, Tsy04].

The interest manifested in fullerene oxides is related to their utilization as precursor for further fullerene based materials [Elv93, Bec95, Gro97B] and to their promising thermal, electronic, and optical properties. Potential applications of fullerene oxides include quantum information processing (QIP) [Zha06], energy storage [Kaw97], and photosensitive systems (this work). The extensive fundamental research on preparation and characterization of fullerene oxide structures has been well reviewed [Hey06].

In the following paragraphs, preparations, characteristics, and applications of dimeric fullerene oxides developed in this work are briefly elucidated.

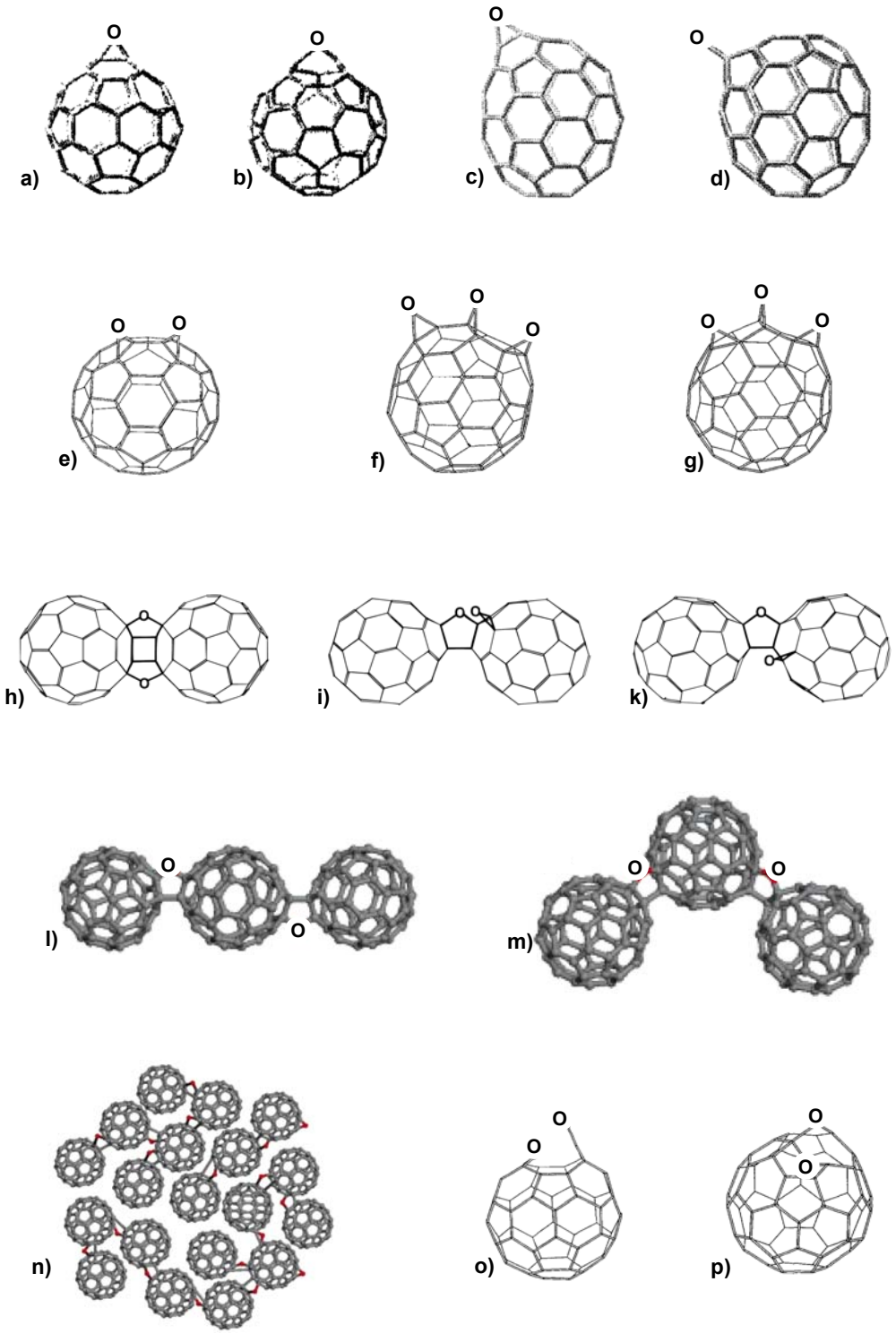

Figure 1.5. *Fullerene oxide structures: a) $C_{60}O$: [6,6]-closed epoxide, b) $C_{60}O$: [5,6]-open oxidoannulene (fulleroid), c) and d) isomers of $C_{70}O$, e) $C_{60}O_2$, f) and g) isomers of $C_{60}O_3$, h), i), and k) isomers of $C_{120}O_2$, l) and m) isomers of $C_{180}O_2$, n) fullerene oxide network, o) and p) isomers of $C_{59}O_2$.*

Preparations of Dimeric Fullerene Oxides

In this work, the dimeric fullerene oxides $C_{120}O$, $C_{130}O$, and $C_{140}O$ were synthesized in preparative amounts by solid-state thermolysis of fullerene/fullerene-oxide mixed powders. *Figure 1.6* exemplifies the two-step synthesis of theses dimeric fullerene oxides using the synthesis of $C_{120}O$.

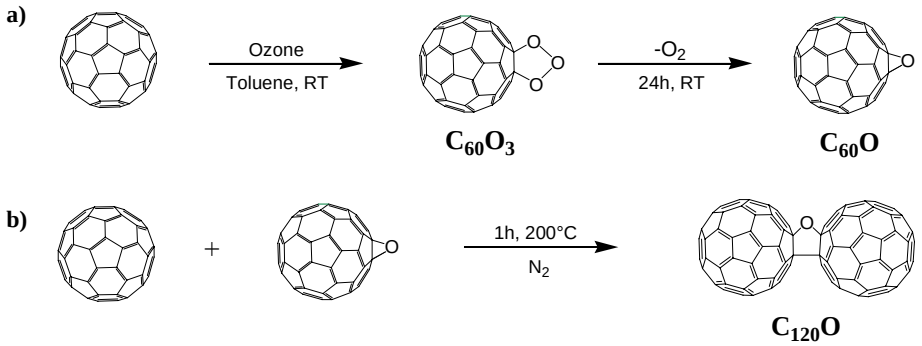

Figure 1.6. *Synthesis route to dimeric fullerene oxides: a) fullerene-oxidation using ozone, b) solid-state thermolysis of fullerene/fullerene-oxide mixed powder.*

For $C_{120}O$, directed and specific preparations of preparative amounts are reported in the literature. $C_{120}O$ can be synthesized by solid-state thermolysis [Leb95] and thermolysis in solution [Smi95] of C_{60}/C_{60}-oxide mixed powders and separated from the resulting product mixtures nearly quantitatively by preparative flash chromatography [Smi95, Kom98, Leb98] or precipitation [Gro96, Gro97B]. As a consequence, the structure-properties relationship of $C_{120}O$ has been characterized rather comprehensively. In addition to comprehensive spectroscopic studies [Leb95, Smi95, Eis98A, Eis98B, Kra98A, Kra98B, Leb98, Sol99, Fuj01C, Yam02, Wan08], which include the structure determination, the characterization of $C_{120}O$ contains the specification of electrochemical [Bal96, Dun03] and thermal properties [Gro96,

Tay98A, Gar03, Zha06], a study on crystals containing $C_{120}O$ [Olm99], as well as theoretical studies [Fow97, Tia00]. Semi-empirical calculations predict $C_{120}O$ to have one energy minimized structure with C_{2V} symmetry [Fow97], and a ^{13}C-NMR-based study [Smi95] has clearly shown that the C_{60} cages in $C_{120}O$ are connected by a furanoid (C_4O) bridge and that $C_{120}O$ has C_{2V} symmetry. *Figure 1.7* shows the structure of $C_{120}O$.

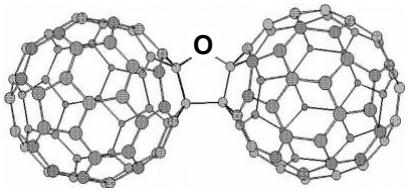

Figure 1.7. *Chemical structure of $C_{120}O$ (C_{2V} symmetry).*

In this work, $C_{120}O$ was synthesized by solid-state thermolysis of C_{60}/C_{60}-oxide mixed powder and isolated from the product mixture by precipitation yielding $C_{120}O$ material of 85 % purity. This $C_{120}O$ material was used as precursor to prepare well-soluble $C_{120}O$ derivatives. To characterize $C_{120}O$ by mass- (MS), infra-red- (IR-), and ultraviolet-visible- (UV-vis-) spectroscopy (see Appendix), as well as by cyclic voltammetry (CV), and thermogravimetric analyses (TGA), highly pure $C_{120}O$ was prepared by semi-preparative high pressure liquid chromatography (HPLC).

Dimeric C_{70} fullerene oxides were first detected in MALDI-TOF analyses of the epoxyfullerene $C_{70}O$ [Jaf99] and thereafter synthesized with poor yields of 2-3 % by hydrothermal treatment and solid-state thermolysis of $C_{70}/C_{70}O$ mixed powders [Kud02]. Three isomers of $C_{140}O$ were separated from the product mixture using HPLC and characterised by mass-, UV-vis-, IR-, Raman-, and ^{13}C-NMR-spectroscopy, but not definitely assigned structurally [Kud02]. In addition, $C_{140}O$ was

synthesized by neutron irradiation of $C_{70}/C_{70}O$ mixed powder and assigned by HPLC and mass spectroscopy, but the yields of the synthesis were not specified in the literature [Zha04]. Finally, semi-empirical calculations predict $C_{140}O$ to have seven isomers, whereof three have nearly equal low energies (*Figure 1.8*) [Fow97].

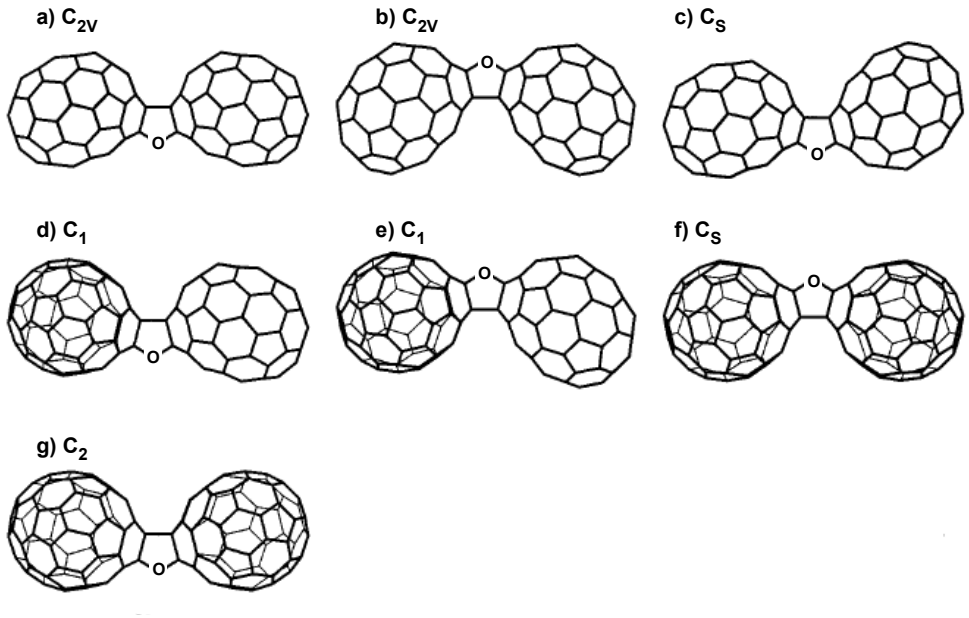

Figure 1.8. *Isomeric structures and corresponding symmetries of $C_{140}O$, the isomers a)-c) show nearly equal low energies [Fow97].*

In this work, a solid-state thermolysis of C_{70}/C_{70}-oxide mixed powder yielding a product mixture containing as main product 35 % $C_{140}O$ as well as a separation of this product mixture by precipitation resulting in $C_{140}O$ material of 97 % purity were developed. The obtained $C_{140}O$ material was characterized by HPLC, mass-, IR-, and UV-vis-spectroscopy (see Appendix), as well as by CV, and TGA.

$C_{130}O$ was extracted from fullerene soot [Tak98] and synthesized by solid-state thermolysis [Eis98A] and hydrothermal treatment [Tak01] of fullerene mixed powders, but the yields of these production methods were not specified in the

literature. $C_{130}O$ was characterized by mass-, IR- [Tak98] and Raman [Eis98A] spectroscopy. Semi-empirical calculations predict $C_{130}O$ to have three isomers (*Figure 1.9*) [Fow97] and three isomers of $C_{130}O$ were experimentally proven [Eis98A].

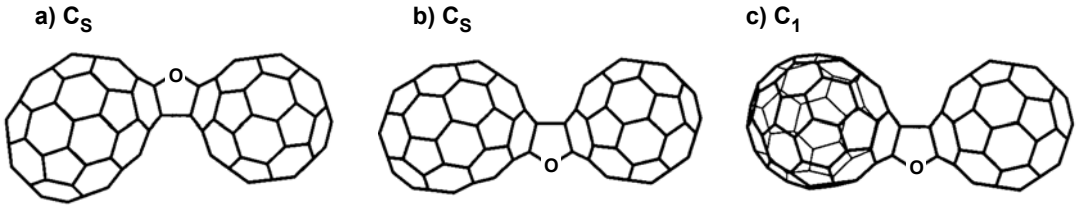

Figure 1.9. *Isomeric structures and corresponding symmetries of $C_{130}O$ [Fow97].*

In this work, a solid-state thermolysis of a fullerene (C_{60} and C_{70})/fullerene-oxide (C_{60}- and C_{70}-oxide) mixed powder yielding a product mixture containing 20 % $C_{130}O$ was developed. Highly pure $C_{130}O$ was prepared by semi-preparative HPLC and characterized by analytical HPLC, mass-, IR-, and UV-vis-spectroscopy (see Appendix), as well as by CV, and TGA.

Furthermore, highly pure, well-soluble mono-, bis-, and tris-adducts of a diazoalkane addition reaction and a Bingel cyclopropanation reaction on $C_{120}O$ were prepared in this work using conventional laboratory methods. *Figure 1.10* illustrates the diazoalkane addition reaction and the Bingel cyclopropanation reaction on $C_{120}O$. *Figure 1.11* illustrates the prepared mono-, bis-, and tris-adducts. As yet, functionalization of dimeric fullerene oxides was not reported in the literature.

The diazoalkan addition reaction was performed on $C_{120}O$ to make a dimeric analogue of the well-known methanofullerene [60]PCBM ($C_{60}R'$ in *Figure 1.12*) [Hum95], which is most frequently used as electron acceptor in fullerene-based organic

photovoltaics [Hop04]. In addition, the bis-adduct of the diazoalkane addition reaction is a dimeric analogue of bis[60]PCBM, which is the bis-adduct analogue of [60]PCBM and has shown to be a more efficient electron acceptor compared to [60]PCBM [Len08]. The Bingel cyclopropanation reaction was chosen to functionalize $C_{120}O$ because of its mild reaction conditions providing high yields and the exclusive formation of [6,6]-bridged adducts [Bin93].

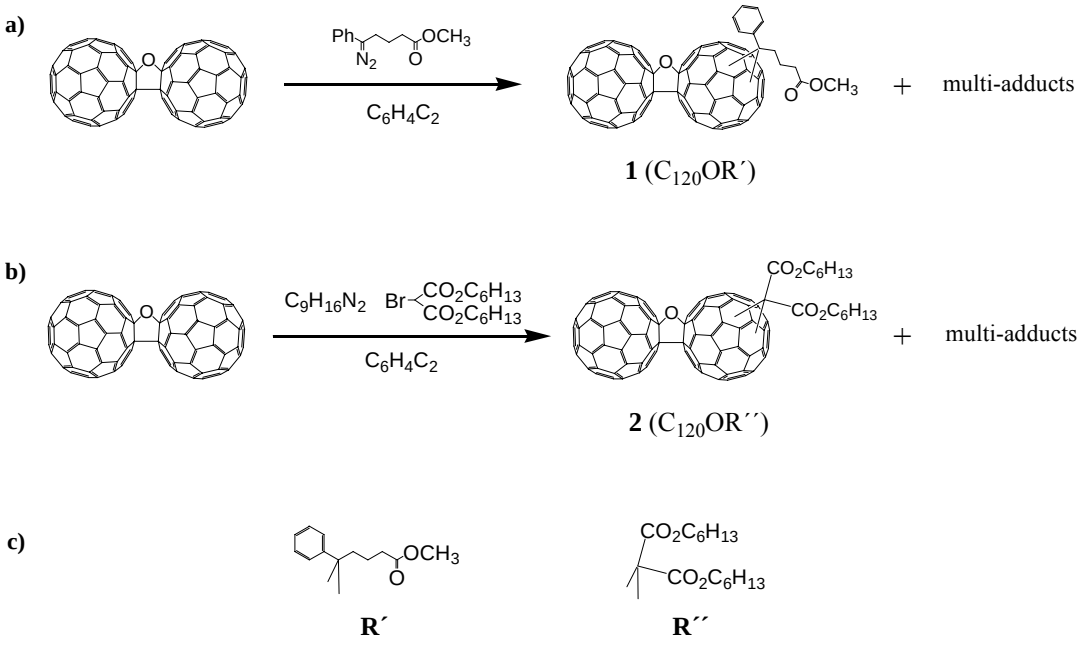

Figure 1.10. *Syntheses of $C_{120}O$ adducts: a) diazoalkane addition reaction and b) Bingel cyclopropanation reaction on $C_{120}O$. c) Side chain labeling used throughout this work.*

All $C_{120}O$ adducts were characterized by analytical HPLC and mass spectroscopy. The mono-adducts **1** ($C_{120}OR´$) and **2** ($C_{120}OR´´$) were additionally characterized by ^{1}H-NMR-, IR-, and UV-vis-spectroscopy (see Appendix), as well as by CV, and TGA. In addition, the mono-adducts **1** and **2** were applied to organic photovoltaics.

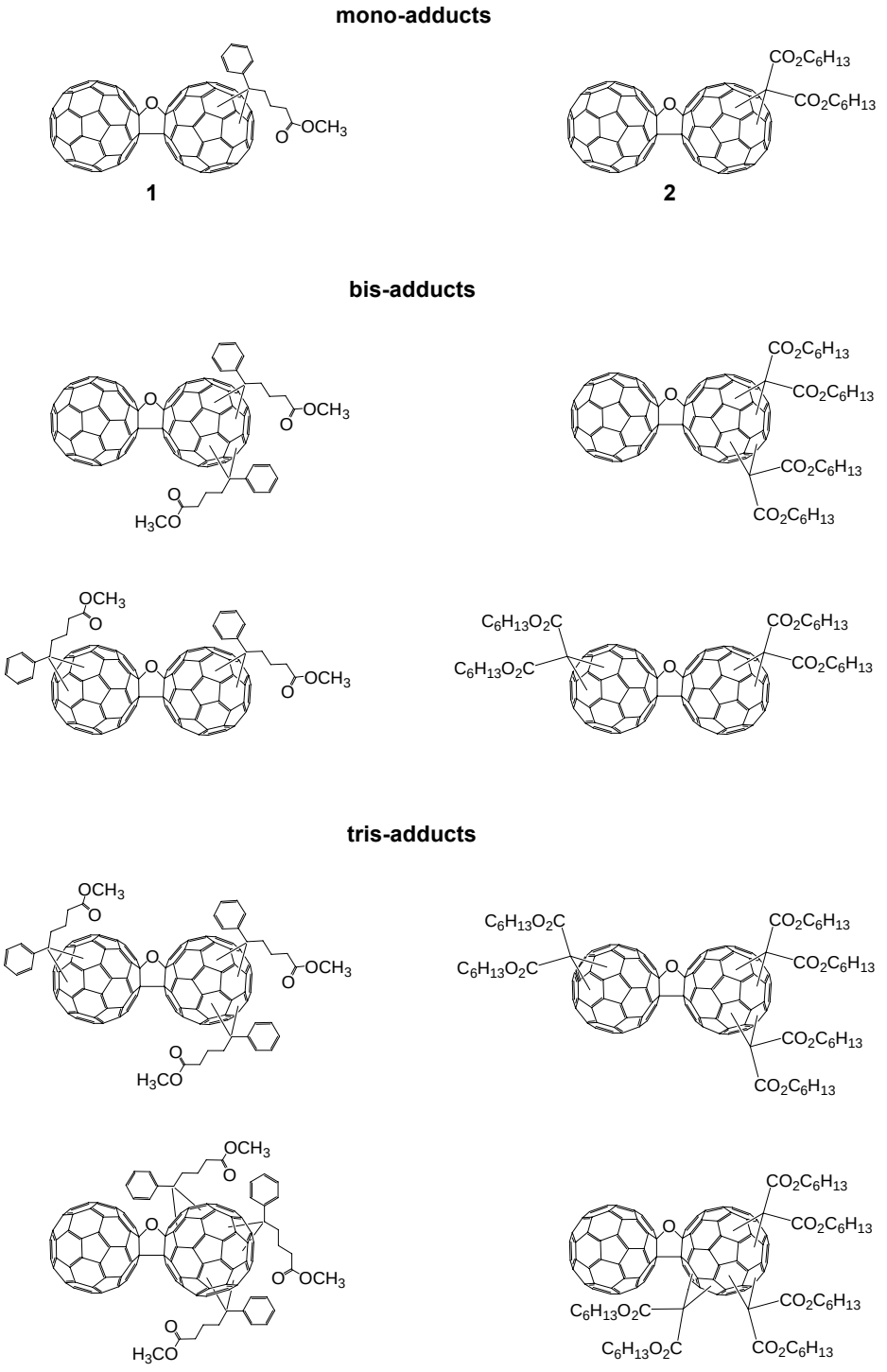

Figure 1.11. *Chemical structures of mono-, bis-, and tris-adducts of $C_{120}O$ obtained by diazoalcane addition reaction (left) and Bingel cyclopropanation reaction (right).*

Finally, a multi-step synthesis route to regio-controlled mono- and bis-functionalized dimeric fullerene oxides using solid-state thermolysis was developed in this work. *Figure 1.12* illustrates the multi-step synthesis route, which allows controlling the functionalization of the cages of dimeric fullerene oxides.

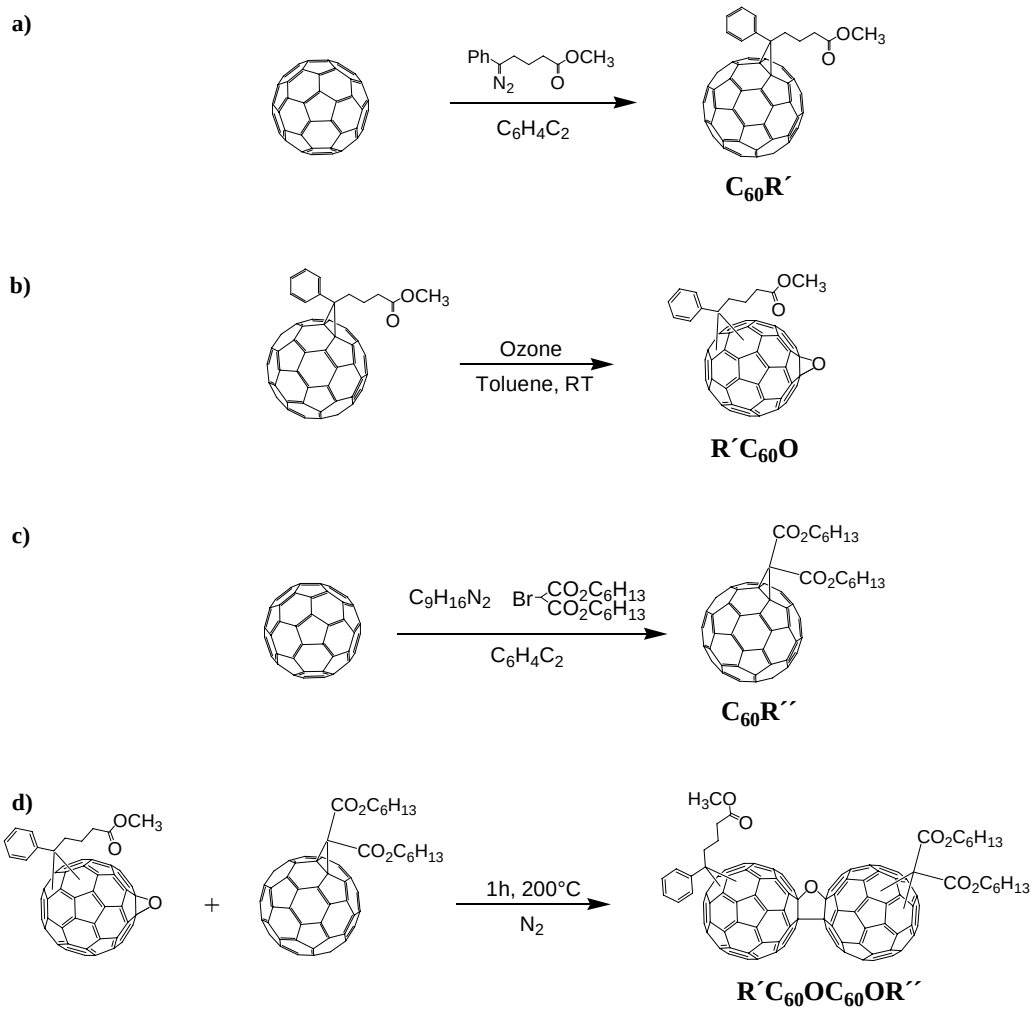

Figure 1.12. *Synthesis route to regio-controlled functionalized dimeric fullerene oxides: a) diazoalkane addition reaction on C_{60}, b) synthesis of a functionalized epoxy-fullerene, c) Bingel cyclopropanation reaction on C_{60}, and d) solid-state thermolysis of a functionalized epoxy-fullerene and a functionalized fullerene yielding a regio-controlled bis-functionalized dimeric fullerene oxide.*

In particular bis-functionalized dimers with different side chains are interesting. Bis-functionalized dimers with appropriate functionalities might be polymerized to block co-polymer chains or might self-assemble due to the mutual attraction of the side chains.

Moreovwe, the synthesis route is an attractive alternative to derivatizing hardly soluble dimeric fullerene oxides. Avoiding hardly soluble intermediate products, the synthesis concept has potential for making higher, soluble oligomeric fullerene oxides.

Characterization of Dimeric Fullerene Oxides

Oxidative and thermal stability, electronic absorption properties, and electron acceptor strength of the dimeric fullerene oxides $C_{120}O$, $C_{130}O$, and $C_{140}O$, and the $C_{120}O$ mono-adducts **1** ($C_{120}OR'$) and **2** ($C_{120}OR''$) were determined by TG analyses, UV-vis-spectroscopy, and CV studies. Comparisons were made with C_{60}, C_{70}, equimolar C_{60}/C_{70} mixtures, $C_{60}R'$, and $C_{60}R''$ (*Figure 1.12*).

A series of dimeric fullerenes was comprehensively characterized for the first time in this work.

Application of Dimeric Fullerene Oxides

Polymer solar cells are promising alternatives to the existing crystalline silicon-based technology. The light weight, semi-transparency, mechanical flexibility, and tunable properties of organic materials, as well as the low-cost fabrication already well developed for all kinds of plastic thin film applications, and the easy integration of

such thin films in a wide variety of devices make polymer solar cells interesting alternatives for the future generation of photovoltaic devices.

At present, the typical device structure of bulk-heterojunction (BHJ) polymer solar cells consists of two disordered, interpenetrating networks consisting of a semi-conducting polymeric donor and an organic acceptor making the photovoltaic active layer sandwiched between two asymmetrical work function (metal) electrodes [Hop04]. The two networks have the following two functions. Firstly, upon irradiation, opposite charges are generated in each network. Secondly, each network transports only one type of charge to the corresponding electrode [Hum04].

Among currently available acceptors, soluble fullerene derivatives have proven to be most efficient materials for solar cell applications [Sen04]. The most frequently used, best investigated, and probably not least therefore currently best available representative of fullerene based acceptor materials is [60]PCBM ($C_{60}R'$ in *Figure 1.12*) [Hop04, Hop06]. Fullerene derivatives are most efficient acceptor materials especially because of the high asymmetry between the ultrafast, photo-induced electron transfer from optically excited p-type hole conducting polymers onto the rather n-type electron conducting fullerenes and the nine orders of magnitudes slower backward electron transfer [Sen04]. This asymmetry allows the use of cell architectures with only one photoactive composite layer instead of donor-acceptor bi-layer devices. The advantage of a photoactive composite layer is an increased donor-acceptor interface and a shortened distance for photoexcitation diffusion to reach this interface [Ibr05].

Today, the power conversion efficiencies of polymer solar cells are low compared to inorganic semiconductor devices [Hop06]. Concepts for improvement include the

optimization of the device structure especially with respect to the electrode contacts, the adjustment of the absorption range of the cell to the terrestrial solar spectrum, the optimization of the band gap between the acceptor and the donor, and an improvement of the morphology of the photoactive blend [Hop04].

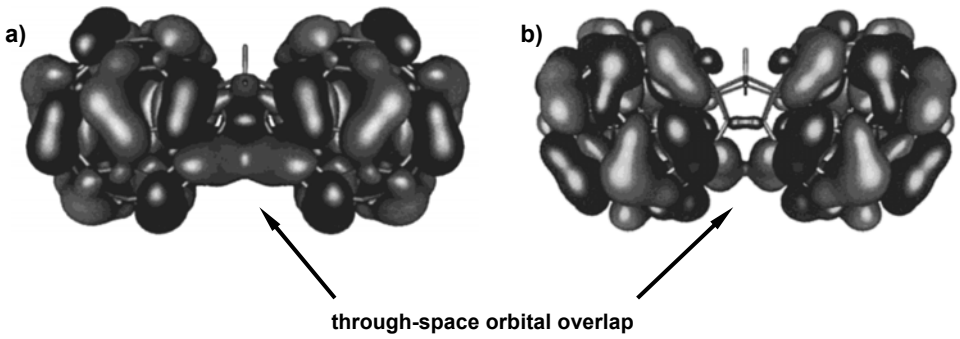

Figure 1.13. *Contour plots of a) HOMO and b) LUMO of $C_{122}H_4$, determined by semi-empirical molecular orbital calculations [Dra00A].*

Well-soluble dimeric fullerenes are valuable compounds to study the impact of well-defined oligomeric fullerene derivatives on the performance of fullerene-based organic electronics and in particular fullerene-based BHJ solar cells. For instance, the fullerene dimers $C_{120}O$, $C_{122}H_4$, $C_{120}SiPh_2$, and $C_{120}GePh_2$, in which the fullerene cages are directly covalently linked (*Figure 1.3*), show intercage electronic interaction (For dimers without direct intercage bonds, intercage electronic interaction was not observed.). This intercage electronic interaction can likely be related to a through-space orbital overlap existing in HOMO/LUMO for dimers with direct intercage bonds (*Figure 1.13*) [Dra00A] and should improve the electron transport properties (electron mobility) of fullerene-based organic electronics. Moreover, the longish shape of fullerene dimers offers the possibility to introduce anisotropy to fullerene-based organic electronics and – for instance – to make fullerene-based photoactive

layers with ordered interpenetrating networks, preferably directed towards the electrodes. Fullerene-based photoactive layers with regularly interpenetrating networks should show improved charge transport properties and a lowered percolation threshold of the fullerene component, which does not significantly contribute to the absorption of light by the photoactive blend [Hum04]. Finally, dimeric fullerenes should stabilize the original morphology of fullerene-based organic blends – mostly achieved by post-processing heat treatment – by delaying the aging process of fullerene aggregation leading to a degradation of the original blend morphology and consequently to a decrease of the performance of the blend.

In this work, the well soluble $C_{120}O$ mono-adducts **1** ($C_{120}OR'$) and **2** ($C_{120}OR''$) were applied as electron acceptor in BHJ polymer solar cells together with the semi-conducting polymer P3HT (*Figure 1.14*) as electron donor. In addition, photo-induced intermolecular electron transfer was proven for photoactive blends made of **1** as electron acceptor and the semi-conducting polymer M3EH-PPV [Kie06] (*Figure 1.14*) as electron donor.

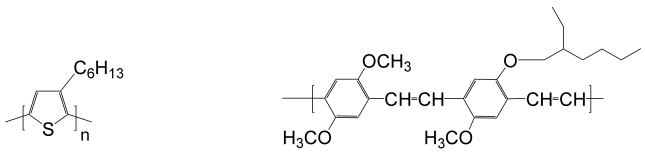

P3HT **M3EH-PPV**

Figure 1.14. *Chemical structures of the semi-conducting polymers P3HT and M3EH-PPV.*

The fullerene oxide $C_{120}O$ was chosen as skeletal backbone for the preparation and application of well-soluble dimeric fullerenes mainly for three reasons. Firstly, $C_{120}O$ shows intercage electronic interaction [Bal96], which is expected to improve the electron transport properties (electron mobility) of fullerene-based organic

electronics. Secondly, $C_{120}O$ is stable upon illumination [Leb00A], [Fuj01C], chemical [Fuj01C], photochemical [Fuj01C], and electrochemical [Bal96] one-electron reduction, as well as upon heating (up to 200°C) [Zha06], which is essential for the photovoltaic application itself, for post processing like thermal annealing, and for a stable morphology of the photovoltaic blends in general. Finally, simple, reliable, and efficient syntheses, as well as methods of isolation of $C_{120}O$ are available ensuring the disposability of preparative amounts of $C_{120}O$.

1.2. Well-aligned MWCNT Array Electrodes

In this chapter, the research field of CNT-based electrochemistry is briefly introduced and the fabrication, characteristics, and application of well-aligned MWCNT array electrodes developed in this work are explicated and put into context.

Carbon nanotubes are excellent electrode materials due to their high electrical conductivity, high aspect ratio, light mass, and mechanical strength, as well as being biocompatible, and relatively chemically inert in most electrolyte solutions, yet retaining a high electrochemical activity, and a wide operational potential window. CNTs are therefore extremely attractive for electrochemical applications such as capacitors, batteries, and (bio-)sensors.

The extensive fundamental research on the electrochemistry of CNTs has been well reviewed under various foci [Mau03, Bal04, Fra04, Laz04, Lin04, Gon05, Mer05, Mou05, Wan05, Bal06, Sin06, Wil06, Tro06].

CNT-based electrodes have been realized from SWCNTs and MWCNTs. The most common types of CNT-based electrodes studied up to now are listed below [Bal04]:

- Powder electrodes were fabricated by filling CNT powder into a microcavity, which was in contact with a metal wire.
- Paste electrodes were fabricated by dispersing CNTs in an organic liquid containing an appropriate binder and filling the mixture into a capillary.
- Composite electrodes were made by coating CNTs with polymers such as polypyrrole [Che01], polyaniline [Gao00], Teflon, or Nafion.

- Film electrodes were made by depositing films of CNTs on glassy carbon (GC) or metal supports. Typically, the CNTs were cast from an aqueous dispersion with or without a surfactant, or from a dispersion in N,N-dimethylformamide.
- Paper electrodes were made from "bucky" paper, which was prepared by vacuum filtration of CNT suspensions through a membrane filter. "Bucky" paper was composed of sheets of entangled CNT bundles held together by van-der-Waals interaction and probably some adhesive impurities.
- Single-nanotube electrodes have been constructed with single CNTs by attaching them to a sharpened platinum wire.
- Microbundle electrodes were made by attaching single CNT bundles to the end of a metal wire.
- CNT-based nanoelectrode arrays were fabricated by growing arrays of well-separated (low-density) CNT bundles or single CNTs on catalyst islands created on a substrate by electron beam lithography [Bal06, Tan08] or electrochemical deposition [Koe04, Tu03, Tu05].
- High-density, vertically aligned CNT array electrodes were made by directly growing forests of high-density vertically aligned CNTs on substrates.

CNT-based electrodes were modified by chemically (chemisorption) and physically (physisorption) linking modifiers to the CNTs, by intercalating modifiers into the CNTs, and by inserting/incorporation modifiers into the framework of the electrodes [Mau03, Bal04, Gon05, Mer05, Mou05, Wan05, Bal06, Wil06].

The CNT-based electrodes used in most of the up to now reported electrochemical studies were film and paste electrodes [Gon05]. Although those CNT-based

electrodes have been demonstrated to be useful for practical electrochemical applications, they have some drawbacks. Firstly, such electrodes are not suitable for fundamental investigations causing difficulties in determining the contributions of the CNTs to the electrochemical properties of the electrode. Moreover, in film electrodes, the CNTs are mechanically and electrically loose, and in paste electrodes, the binder brings impurities into the electrode and degrades the electrochemical performance of the CNTs. Finally, film and paste electrodes show a high contact resistance between the active material (CNTs) and the current collectors (graphite foil or metallic substrates).

Self-assembled, aligned and ordered CNT architectures directly grown on substrates by CVD are an attractive alternative to film and paste electrodes. Such architectures can be controlled on the nanometer scale, allow the exploitation of the whole CNT surface and an elegant electrode construction, require no binder, and show a low contact resistance.

The great potential of aligned and ordered CNT architectures for use in supercapacitors [Che02, Che04, Hon07A, Hon07B, Wei08, Ye05A, Ye05B, Zha08A], electrochemical (bio)-sensors [Ye03, Ye04, Roy06, Tan06, Ye06, Yun06, Pun08, Tan08], direct methanol fuel cells [Tan05], and nanoelectrode ensembles [Koe04, Tu03, Tu05] has been impressively demonstrated. In addition, basic electrochemical properties [Li02, Zha08B] and the electrochemical modification of CNT array electrodes were studied [Ye06].

However, the structure-properties relationship of CNT array electrodes was not systematically studied up to now. In this work, intrinsic electrochemical characteristics of high-density, vertically aligned MWCNT array electrodes were

determined in dependence on the deposit thickness of the arrays. The characteristics include capacitance, active surface area, internal resistance, as well as electron transfer resistance and were determined by cyclic voltammetry (CV) and electrochemical impedance spectroscopy (EIS). *Figure 1.15* shows a typical morphology of a MWCNT array used in this work and a single MWCNT of such an array.

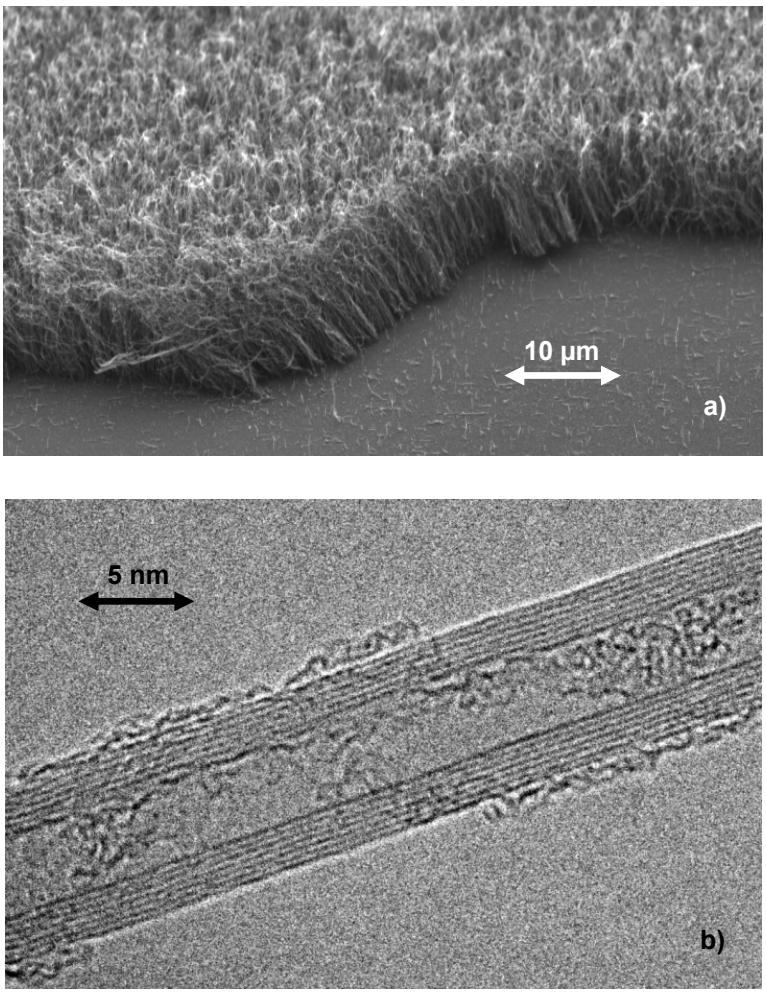

Figure 1.15. *a) SEM image of a well-aligned MWCNT array and b) TEM image of a single MWCNT of such an array.*

In addition, the great potential of aligned and ordered CNT architectures for electrochemical sensing was demonstrated in this work by applying well-aligned MWCNT array electrodes to non-enzymatic voltammetric and amperometric glucose detection. Enzyme-based electrochemical glucose detection is well established and shows high sensitivity and selectivity, but lacks stability due to the intrinsic unstable nature of enzymes. Furthermore, enzymatic glucose sensing is limited to a low oxygen concentration because the electron-mediating sites of the sensors compete with oxygen dissolved in the solution. Finally, enzymatic glucose sensors require enzyme immobilization, which lacks reproducibility and results in a complex electrode design. Possible applications of non-enzymatic glucose sensors include continuous monitoring in bio-chemical (fermentation) processes and human bodies (implants), as well as the use in clinical diagnostics [Par06] and lab-on-chip applications [Cho08].

CNT-based, non-enzymatic glucose detection has been studied at film [Kan07, Wan07], paste [Xie07, Xie08], and array electrodes [Ye04, Cui06, Cui07, Tan08].

The structure-properties relationship of MWCNT array electrodes determined in this work associated with the potential of such electrodes for non-enzymatic glucose detection demonstrated in this and other works contribute to the developing of non-enzymatic glucose sensors.

2. Experimental Section

In this chapter, experimental procedures used to prepare and apply dimeric fullerene oxides and well-aligned MWCNT array electrodes considered in this work are specified.

2.1. Preparations

Preparation of Monomeric C_{60} and C_{70} Derivatives

The monomeric fullerene derivatives shown in *Figure 2.1* were prepared as precursors for synthezising regio-controlled functionalized dimeric fullerene oxides and comparing physicochemical characteristics of functionalized monomeric and dimeric fullerenes.

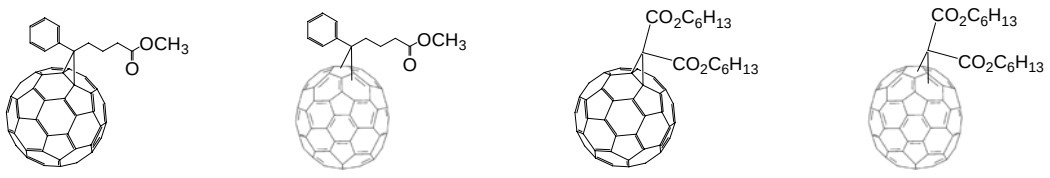

a) $C_{60}R'$ **b) $C_{70}R'$** **c) $C_{60}R''$** **d) $C_{70}R''$**

Figure 2.1. *Chemical structures of monomeric C_{60} and C_{70} derivatives.*

$C_{60}R'$ ([60]PCBM or $C_{60}C_{12}H_{14}O_2$) and $C_{70}R'$ ([70]PCBM or $C_{70}C_{12}H_{14}O_2$) were prepared according to literature procedures [Hum95, Wie03] *via* diazoalkane addition reactions using 4-benzoyl-methylbutyrate p-tosylhydrazone as diazo compound precursor and sodium methoxide as activating base. *Figure 1.12 a)* illustrates the synthesis of $C_{60}R'$.

$C_{60}R''$ ($C_{60}C(COOC_6H_{13})_2$) and $C_{70}R''$ ($C_{70}C(COOC_6H_{13})_2$) were prepared according to the method of Bingel [Bin93] using dihexyl bromomalonate as active methylene compound and DBU (1,8-diazabicyclo [5.4.0]undec-7-ene) as activating base. *Figure 1.12 c)* illustrates the syntheses of $C_{60}R''$.

Monomeric C_{70} derivatives were obtained as isomeric mixtures and used as such. *Figure 2.2* exemplifies three regio-isomers of $C_{70}R'$.

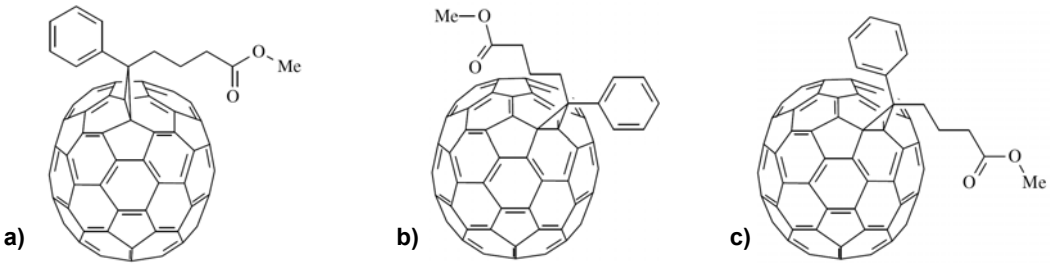

Figure 2.2. *Regio-isomers of $C_{70}R'$([70]PCBM, $C_{70}C_{12}H_{14}O_2$) [Wie03].*

Preparation of $C_{120}O$

$C_{120}O$ was produced according to a literature procedure [Leb95] by solid-state thermolysis of C_{60}/C_{60}-oxide mixed powder. The C_{60}/C_{60}-oxide mixture was prepared by HPLC-controlled oxidation of C_{60} dissolved in toluene using ozone as oxidizing agent (*Figure 1.6*). The oxidation was carried out by purging an oxygen/ozone gas mixture, which was produced by an ozone generator, through a stirred solution of C_{60} in toluene. The C_{60} ozonides initially formed by ozonization were allowed to dissociate into $C_{60}O_n$ epoxyfullerenes and molecular oxygen overnight [Hey06]. Subsequently, the solution was carefully filtered to remove precipitating reaction products. According to MS analyses, these precipitating reaction products were C_{60} fullerene oxides $C_{60}O_n$ (n = 1-7). After filtration, the solvent was evaporated to obtain the C_{60}/C_{60}-oxide mixed powder containing approximately C_{60} (~90 %), $C_{60}O$ (~10 %), and traces of $C_{60}O_2$, as determined by HPLC (*Figure 2.3*) and MS.

The solid-state thermolysis was carried out by heating the solid C_{60}/C_{60}-oxide mixture in air at 200 °C for 1 h. As determined by HPLC (*Figure 2.3*) and MS (*Figure 2.4*), the product mixture of the thermolysis contained $C_{120}O$ (~30 %), unreacted C_{60}, as well as traces of $C_{120}O_n$ and $C_{180}O_n$ (n = 2, 3) as by-products.

By adding n-hexane to a saturated ortho-dichlorobenzene (ODCB) solution of the product mixture, dimeric and trimeric reaction products were precipitated and separated from un-reacted C_{60} [Gro96, Gro97B]. As determined by HPLC (*Figure 2.3*) and MS, the precipitate contained up to 85 % $C_{120}O$.

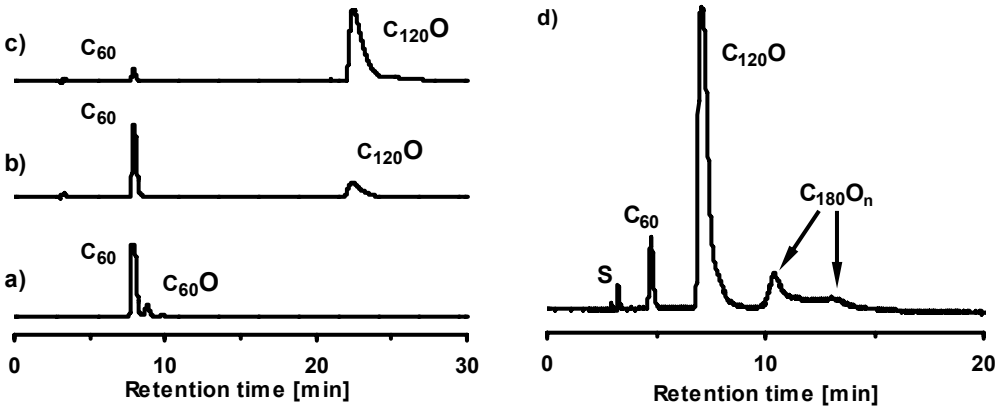

Figure 2.3. *HPLC charts of a) C_{60}/C_{60}-oxide mixed powder, b) the reaction product of the thermolysis, c) and d) the reaction product after removing un-reacted C_{60} (analytical Cosmosil Buckyprep column (4.6 x 250 mm²) eluted at 1 mL/min with a), b), and c) toluene, and d) toluene/ODCB (7/3, v/v), detection at 330 nm).*

The precipitate was used as starting material for the diazoalkane addition and the Bingel cyclopropanation reaction without further purification. To characterize $C_{120}O$ by mass-, IR-, UV-vis-spectroscopy, as well as by TGA and CV, highly pure $C_{120}O$ was prepared by semi-preparative HPLC using a Cosmosil Buckyprep column (250 x 20 mm²) eluted at 18 mL/min with toluene/ODCB (7/3, v/v).

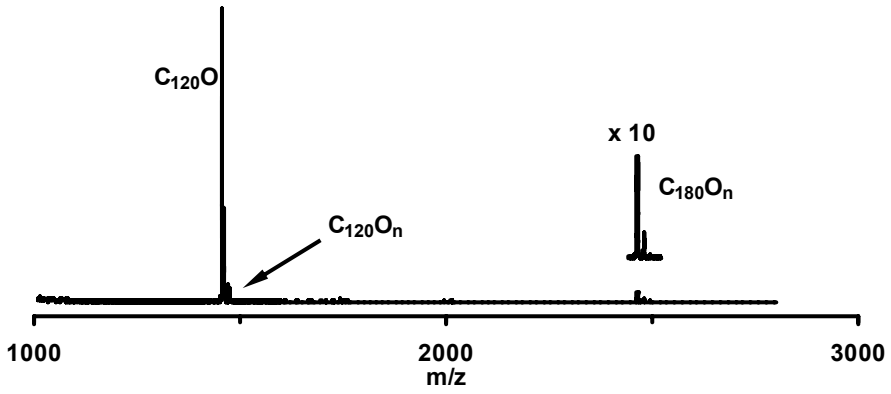

Figure 2.4. *Detail of the mass spectrum of the reaction product of the C_{60}/$C_{60}O$ thermolysis.*

Preparation of $C_{140}O$

In analogy to the $C_{120}O$ synthesis, $C_{140}O$ was produced by solid-state thermolysis of C_{70}/C_{70}-oxide mixed powder. *Figure 1.5* shows the chemical structure of $C_{70}O$ isomers.

The C_{70}/C_{70}-oxide mixture was prepared by ozonolysis of C_{70} dissolved in toluene and contained C_{70} (~85 %), $C_{70}O$ (~13 %), and $C_{70}O_n$ (~2 %, n = 2, 3), as determined by HPLC (*Figure 2.5*) and MS. After filtration, the solvent was evaporated to obtain the solid C_{70}/C_{70}-oxide mixture.

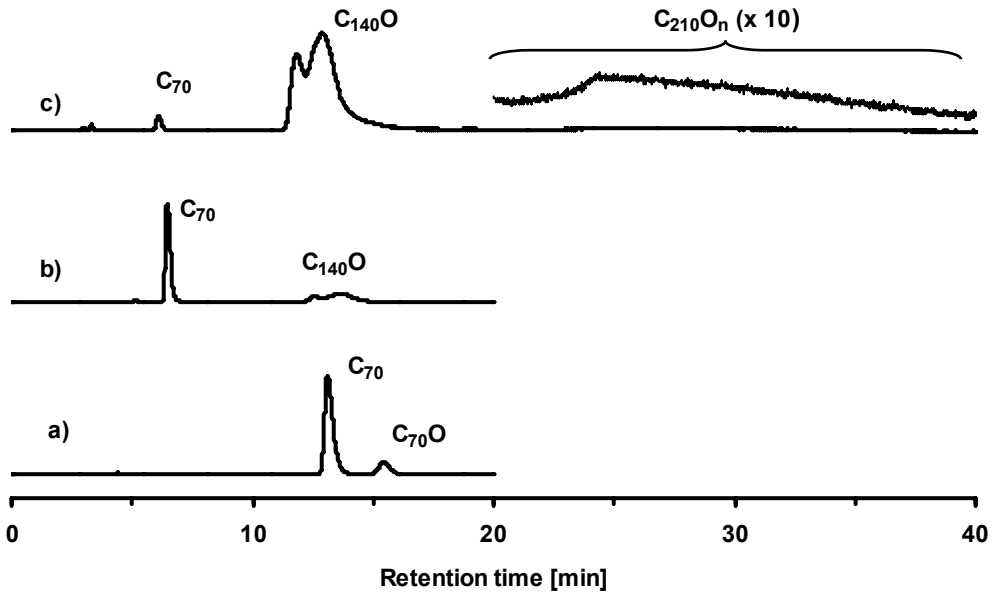

Figure 2.5. *HPLC charts of a) C_{70}/C_{70}-oxide mixed powder, b) the reaction product of the thermolysis, and c) the reaction product after removing un-reacted C_{70} (analytical Cosmosil Buckyprep column (4.6 x 250 mm²) eluted at 1 mL/min with a) toluene, b) and c) toluene/ODCB (7/3, v/v), detection at 330 nm).*

The solid-state thermolysis was carried out by heating the solid C_{70}/C_{70}-oxide mixed powder under nitrogen atmosphere at 200 °C for 1 h. As determined by HPLC (*Figure 2.5*) and MS (*Figure 2.6*), the product mixture of the thermolysis contained $C_{140}O$ (~35 %), un-reacted C_{70} (~60 %), as well as traces of dimeric and trimeric C_{70} fullerene poly-oxides of the form $C_{140}O_n$ (n = 2-5) and $C_{210}O_n$ (n = 2, 3).

The product mixture was worked off by precipitation caused by adding n-hexane to a saturated ODCB solution of the mixture. As determined by HPLC (*Figure 2.5*) and MS, the precipitate contained up to 97 % $C_{140}O$, 2 % C_{70}, as well as traces (~1 %) of dimeric and trimeric C_{70} poly-oxides ($C_{140}O_n$ (n = 3-5) and $C_{210}O_n$ (n = 2, 3)).

The precipitate was used without further purification to characterize $C_{140}O$ by analytical HPLC, mass-, IR-, UV-vis-spectroscopy, as well as by TGA and CV.

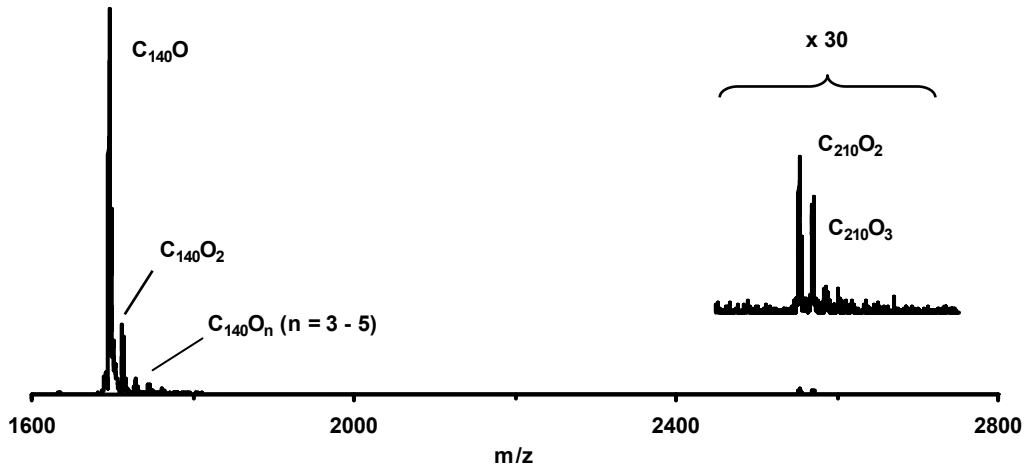

Figure 2.6. *Detail of the mass spectrum of the reaction product of the C_{70}/$C_{70}O$ thermolysis.*

Preparation of $C_{130}O$

$C_{130}O$ was produced by solid-state thermolysis of a mixed powder containing C_{60} and C_{70} (each 45 %), as well as C_{60}-oxide and C_{70}-oxide (each 5 %) (*Figure 2.7*). To obtain such a solid mixture, C_{60}/C_{60}-oxide and C_{70}/C_{70}-oxide solutions were separately prepared by HPLC-controlled oxidation of C_{60} and C_{70} dissolved in toluene using ozone as oxidizing agent. C_{60} and C_{70} were separately oxidized because dissolved C_{60} oxidizes easier upon exposure to ozone than dissolved C_{70} [Elv93]. The C_{60}/C_{60}-oxide (C_{70}/C_{70}-oxide) solution approximately contained 90 % non-oxidized C_{60} (C_{70}), 10 % $C_{60}O$ ($C_{70}O$), and traces of higher epoxies of the form $C_{60}O_n$ ($C_{70}O_n$) (n = 2-3). The solutions were carefully filtered and then united. Thereafter, the solvent was evaporated in order to obtain the solid fullerene mixture. The solid-state thermolysis was carried out by heating the solid mixture under nitrogen atmosphere at 200 °C for 1 h.

As determined by HPLC (*Figure 2.7*) and MS (*Figure 2.8)*, the product mixture of the thermolysis contained the dimeric fullerene oxides $C_{130}O$ (~20 %), $C_{120}O$ (~20 %) and $C_{140}O$ (~8 %), un-reacted C_{60} (~30 %) and C_{70} (~22 %), as well as traces of dimeric and trimeric fullerene poly-oxides of the form $C_{130}O_n$ (n = 2-5), $C_{120}O_n$ (n = 2-5), $C_{140}O_n$ (n = 2-4), $C_{180}O_n$ (n = 2, 3) and $C_{190}O_n$ (n = 2). By adding n-hexane to a saturated ODCB solution of the product mixture, the dimeric and trimeric reaction products were precipitated and separated from un-reacted C_{60} and C_{70}.

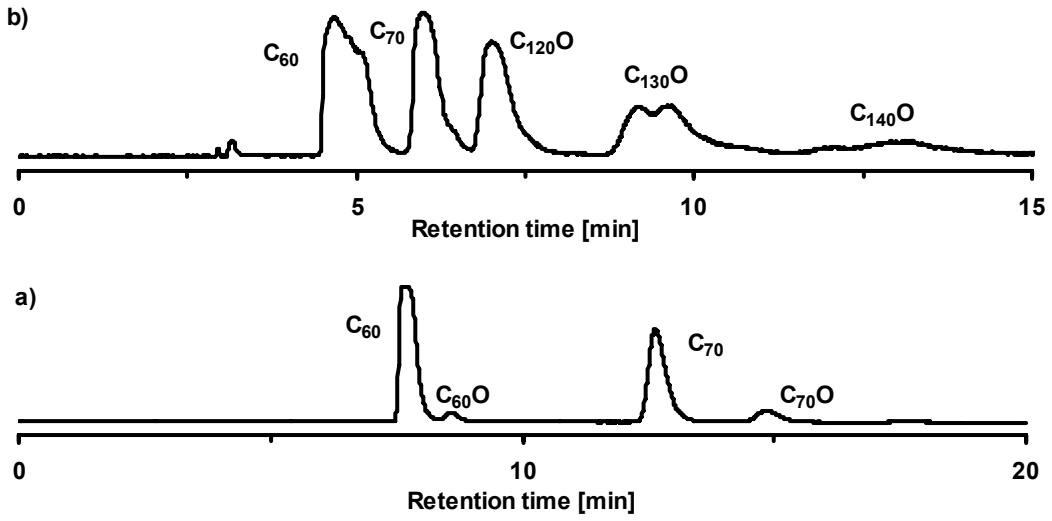

Figure 2.7. *HPLC charts of a) C_{60}/C_{60}-oxide/C_{70}/C_{70}-oxide mixed powder, and b) the reaction product of the thermolysis of such a powder (analytical Cosmosil Buckyprep column (4.6 x 250 mm²) eluted at 1 mL/min with a) toluene, and b) toluene/ODCB (7/3, v/v), detection at 330 nm).*

To characterize $C_{130}O$ by analytical HPLC, mass-, IR-, UV-vis-spectroscopy, as well as by TGA and CV, highly pure $C_{130}O$ was prepared by semi-preparative HPLC using a Cosmosil Buckyprep column (250 x 20 mm²) eluted at 18 mL/min with toluene/ODCB (7/3, v/v).

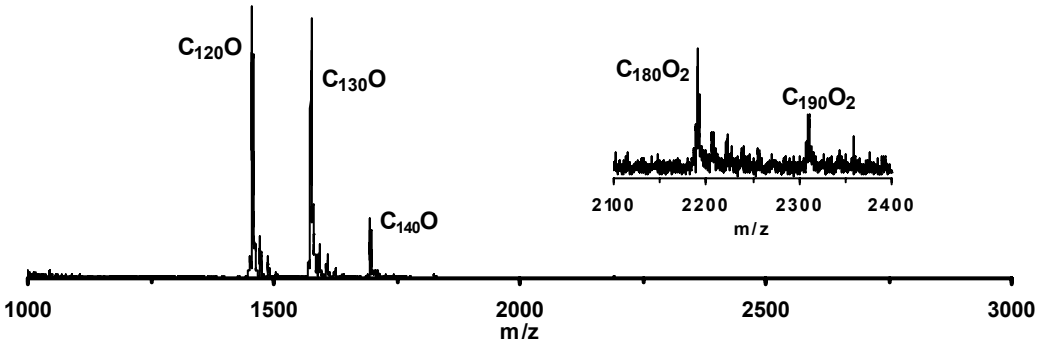

Figure 2.8. *Mass spectrum of the reaction product of the $C_{130}O$ synthesis.*

Diazoalcane Addition and Bingel Reaction on $C_{120}O$

In a typical procedure, the diazoalkane addition reaction on $C_{120}O$ was carried out by heating a stirred solution of $C_{120}O$ (100 mg, 0.07 mmol) in ODCB (200 mL) under nitrogen atmosphere to 70 °C, and thereafter adding a suspension of 4-benzoyl-methylbutyrate p-tosylhydrazone (52.5 mg, 0.14 mmol, 2 equiv.) and sodium methoxide (7.6 mg, 0.14 mmol, 2 equiv.) in pyridine (5 mL) to the stirred solution. The homogeneous reaction mixture was stirred under nitrogen at 70 °C for 24 h. Subsequently, the reaction mixture was concentrated by evaporating the volatile components under vacuum. *Figure 1.10* illustrates the diazoalkane addition reaction on $C_{120}O$.

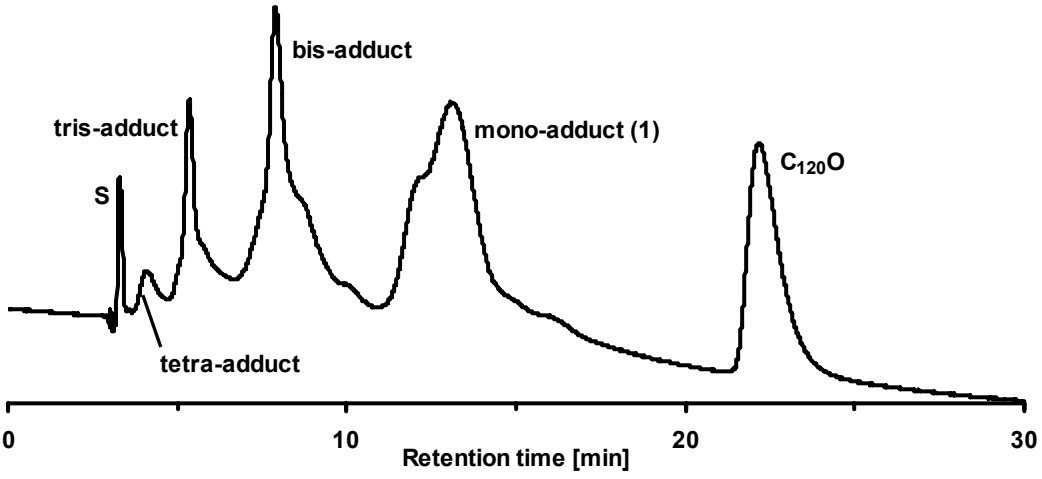

Figure 2.9. *HPLC chart of the product mixture of the diazoalkane additon reaction on $C_{120}O$ (analytical Cosmosil Buckyprep column (4.6 x 250 mm²) eluted at 1 mL/min with toluene, detection at 330 nm).*

As determined by HPLC (*Figure 2.9*) and MS (*Figure 2.10*), the product mixture of the diazoalkane addition reaction contained mono-adduct (~40 %, $C_{120}OR'$), bis- and

tris-adducts (~20 %, $C_{120}OR'_m$, m = 2, 3), un-reacted $C_{120}O$ (~40 %), as well as traces of dimeric and trimeric fullerene poly-oxides of the form $C_{120}O_nR'_m$ (n = 2, 3; m = 0-3) and $C_{180}O_nR'_m$ (n = 2-4; m = 0-2). The reaction product was separated by preparative flash chromatography using silica gel. Elution with carbon disulfide yielded un-reacted $C_{120}O$ followed by the mono-adduct. Subsequent elution with cyclohexane/toluene (1/1, v/v) yielded the bis-adducts. Further elution with toluene yielded the tris-adducts.

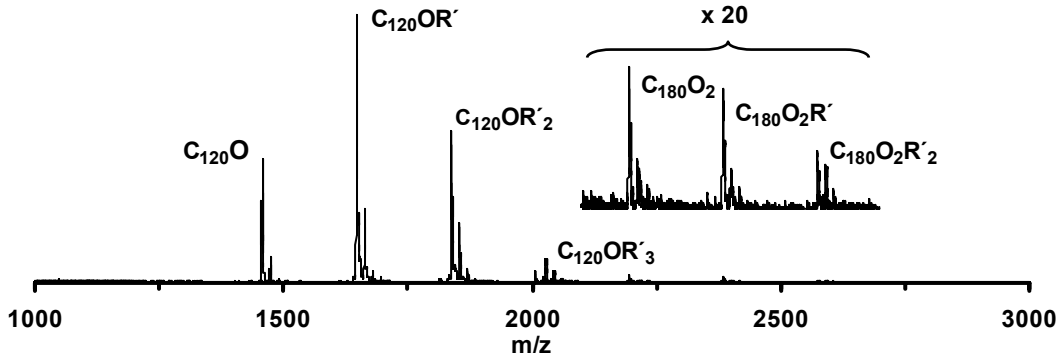

Figure 2.10. *Mass spectrum of the reaction product of the diazoalkane addition reaction on $C_{120}O$.*

In a typical procedure, the Bingel cyclopropanation reaction on $C_{120}O$ was performed by adding dihexyl bromomalonate (35.1 mg, 0.1 mmol, 1.5 equiv.) and 1,8-diazabicyclo[5.4.0]undec-7-ene (DBU, 19.8 mg, 0.13 mmol, 2 equiv.) to a stirred solution of $C_{120}O$ (100 mg, 0.07 mmol) in ODCB (200 mL) and thereafter stirring the reaction mixture at room temperature for five hours. *Figure 1.10* illustrates the Bingel reaction on $C_{120}O$. As determined by HPLC (*Figure 2.11*) and MS (*Figure 2.12*), the product mixture of the Bingel reaction contained mono-adduct (~40 %, $C_{120}OR''$), bis- and tris-adducts (~35 %, $C_{120}OR''_m$, m = 2, 3), un-reacted $C_{120}O$ (~25 %), as well

as traces of dimeric and trimeric fullerene poly-oxides of the form $C_{120}O_nR''_m$ (n = 2-3; m = 0-3) and $C_{180}O_nR''_m$ (n = 2-4; m = 0-2).

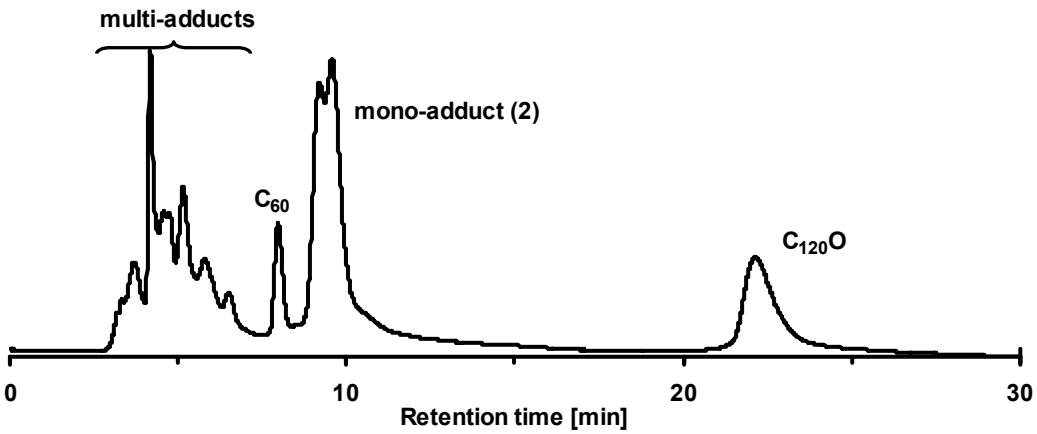

Figure 2.11. *HPLC chart of the product mixture of the Bingel reaction on $C_{120}O$ (analytical Cosmosil Buckyprep column (4.6 x 250 mm²) eluted at 1 mL/min with toluene, detection at 330 nm).*

The product mixture of the Bingel reaction was separated in analogy to the product mixture of the diazoalkane addition reaction.

According to MS analyses, both the reaction product of the diazoalkane addition reaction and that of the Bingel reaction occasionally contained traces of tetra-adducts.

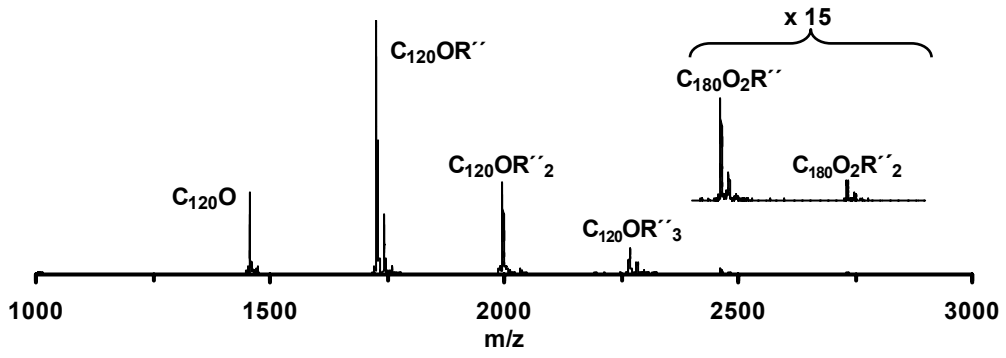

Figure 2.12. *Mass spectrum of the reaction product of the Bingel reaction on $C_{120}O$.*

Regio-controlled Functionalized Dimeric Fullerene Oxides

Regio-controlled mono- and bis-functionalized fullerene dimers were synthesized by solid-state thermolysis of mixtures containing the functionalized epoxy-fullerene R´C_{60}O or R´C_{70}O and a reactant fullerene. *Figure 1.12* illustrates the synthesis route to regio-controlled functionalized fullerene dimers. In *Table 2.1*, the converted mixtures and the resulting regio-controlled functionalized dimers are summarized. *Figure 2.13* illustrates the used functionalized epoxy-fullerenes and *Figure 2.1* shows the used reactant fullerene derivatives.

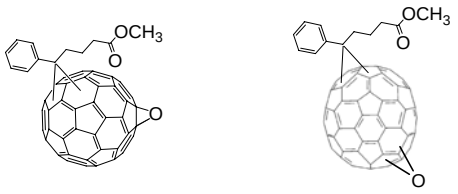

a) R´C_{60}O **b) R´C_{70}O**

Figure 2.13. *Functionalized monomeric epoxy-fullerenes.*

Table 2.1. *By solid-state thermolysis converted mixtures containing the functionalized epoxy-fullerene R´C_{60}O or R´C_{70}O and a reactant fullerene as well as molar masses of the resulting regio-controlled functionalized dimers.*

No.	Epoxide	Reactant	Dimer (M [g/mol])
a)	R´C_{60}O	C_{60}	R´$C_{60}OC_{60}$ (1646)
b)	R´C_{60}O	C_{60}R´	R´$C_{60}OC_{60}$R´ (1836)
c)	R´C_{60}O	C_{60}R´´	R´$C_{60}OC_{60}$R´´ (1916)
d)	R´C_{60}O	C_{70}	R´$C_{60}OC_{70}$ (1766)
e)	R´C_{60}O	C_{70}R´	R´$C_{60}OC_{70}$R´ (1956)
f)	R´C_{60}O	C_{70}R´´	R´$C_{60}OC_{70}$R´´ (2036)
g)	R´C_{70}O	C_{70}	R´$C_{70}OC_{70}$ (1886)
h)	R´C_{70}O	C_{70}R´	R´$C_{70}OC_{70}$R´ (2076)
i)	R´C_{70}O	C_{60}R´´	R´C_{70}O C_{60}R´´ (2136)
k)	R´C_{70}O	C_{70}R´´	R´C_{70}O C_{70}R´´ (2156)

To prepare the solid mixtures, the fullerene derivatives $C_{60}R'$ and $C_{70}R'$ were dissolved in toluene and subsequently partly oxidized using ozone as oxidizing agent. According to MS analyses (*Figure 2.14*), the side chain R´ was not affected by the oxidation. After the oxidation, the solutions were filtered and then united according to *Table 2.1* with solutions of the reactant fullerenes. Thereafter, the solvent of the prepared solutions was evaporated to obtain the solid fullerene mixtures. The solid-state thermolysis was carried out by heating the solid mixtures under nitrogen atmosphere at 200 °C for 1 h.

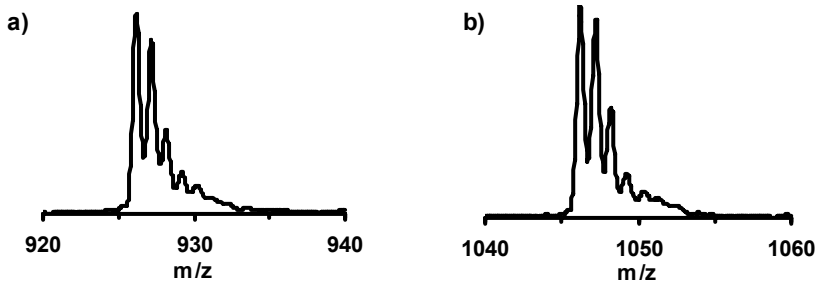

Figure 2.14. *Mass spectra of a) R´$C_{60}O$ (926 g/mol) and b) R´$C_{70}O$ (1046 g/mol).*

Preparation of Well-aligned MWCNT Arrays

Well-aligned MWCNT arrays were directly grown on silica substrates (~0.3 or 1 cm²) by thermal chemical vapor deposition (CVD) at 900 °C using ferrocene as catalyst source and benzene as carbon source. *Figure 2.15* shows a schematic of the CVD process and *Figure 2.16* illustrates the experimental set-up used for the CVD process. In brief, the growth process was carried out in a horizontal quartz tube (diameter: 3 cm, length: 70 cm) housed in a muffle furnace. The silica substrates were placed in the middle of the quartz tube. The quartz tube was constantly fed with argon (5 L/h) and gradually heated to 900 °C. After reaching 900 °C, a solution of ferrocene in benzene (2 wt. %) was added to the argon flow through a nozzle using a syringe pump and a flow rate of 10 mL/h. The solution was added for six (1 mL solution) or twelve minutes (2 mL solution). After adding the solution, the quartz tube was slowly cooled down to room temperature under constant argon feed. A detailed description of the synthesis is given in the literature [Kap08].

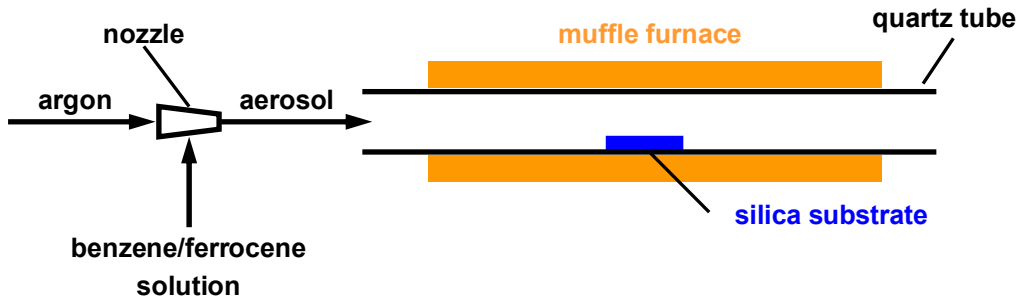

Figure 2.15. *Schematic of the CVD process.*

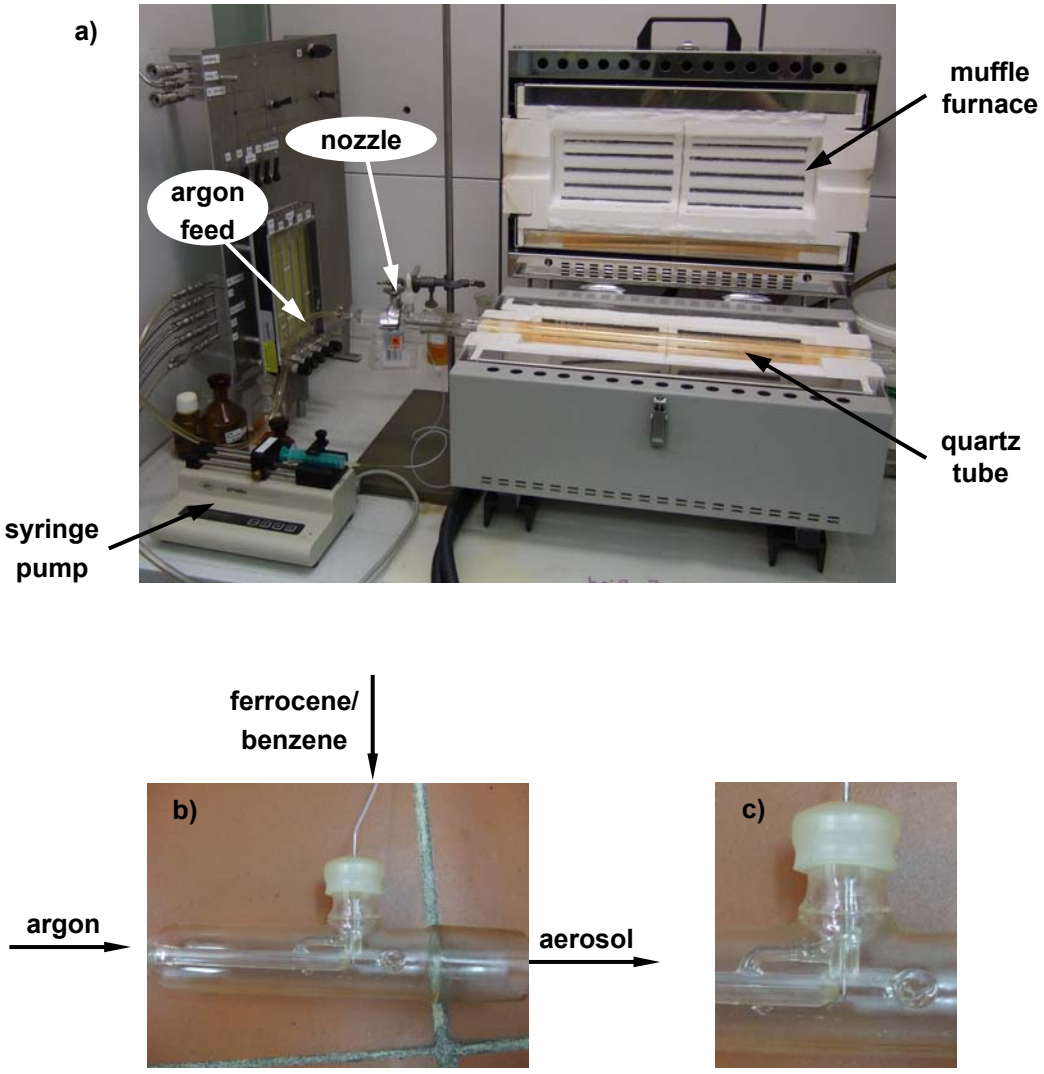

Figure 2.16. *a) Experimental set-up used to make well-aligned MWCNT arrays, b) nozzle used to spray the ferrocene/bencene solution into the tube, c) detail of the nozzle.*

2.2. Device Fabrication and Measurement

Bulk-heterojunction Solar Cell Devices

The well-soluble $C_{120}O$ mono-adducts **1** ($C_{120}OR'$) and **2** ($C_{120}OR''$) (*Figure 1.10*) were applied as electron acceptor in BHJ polymer solar cells together with the semiconducting polymer P3HT (*Figure 1.14*) as electron donor.

The BHJ solar cell devices were prepared using inidium tin oxide (ITO) glass substrates which were cleaned in an ultrasonic bath successively using methanol, acetone and isopropanol. To supplement these front (bottom) electrodes, hole transport layers of poly(3,4-ethylenedioxythiophene) doped with poly(styrene sulfonic acid) (PEDOT-PSS) were spun from aqueous dispersion solutions, before drying the substrates at 150 °C for 5 min. Next, photoactive layers consisting of P3HT:**1** or P3HT:**2** (1:0.8, w/w) were spin-coated from filtered chlorobenzene solutions on top of the PEDOT:PSS layers. The thicknesses of the photoactive layers typically were in the range of 100-150 nm. To complete the solar cell devices, aluminum (back electrode) cathodes were thermally deposited (80 nm) through a shadow mask, which defined a device area of 25 mm². The substrates were annealed for three minutes in a glove box at 150 °C. Except for the annealing, the cells were prepared under ambient conditions.

Current density versus voltage characteristics of the solar cells were recorded under AM1.5 conditions by illuminating the cells from the ITO side with 100 mW/cm² white light. All measurements were performed under ambient conditions.

MWCNT Array Electrodes

MWCNT array electrodes were made by attaching as-grown MWCNT arrays to platinum wires using conductive silver paint and insulating the splice with nail enamel. *Figure 2.17* shows a photo of a MWCNT array electrode. To remove metal catalyst residue and carbonaceous by-products, the MWCNT array electrodes were electrochemically purified in aqueous 0.1 M HCl solutions by repeated potential cycling between -0.7 and 1.5 V vs. 3 M KCl-Ag/AgCl.

To analyze the capacitive characteristics of the MWCNT electrodes, CV and EIS measurements were carried out in aqueous 0.1 M KCl solutions. To study the electron transfer (faradaic) characteristics of the MWCNT electrodes, CV and EIS measurements were performed on aqueous 0.1 M KCl solutions containing 5 mM $K_4Fe(CN)_6$ as redox probe.

Non-enzymatic glucose detection using MWCNT array electrodes was studied by cyclic voltammetry and amperometry in aqueous 0.1 M NaOH solutions containing 2-5 mM glucose.

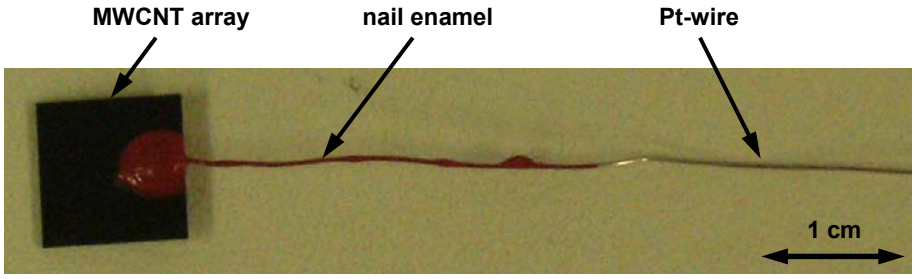

Figure 2.17. *Photo of a MWCNT array electrode.*

3. Results and Discussion

In this chapter, research results achieved in this work are discussed in detail. Results concerning dimeric fullerene oxides are regarded in chapter 3.1. Results regarding well-aligned MWCNT arrays are considered in chapter 3.2.

3.1. Dimeric Fullerene Oxides

In this chapter, preparations, characteristics, and applications of dimeric fullerene oxides developed in this work are extensively discussed.

3.1.1. Preparation of Dimeric Fullerene Oxides

Following, the preparations of $C_{120}O$, $C_{140}O$, $C_{130}O$, soluble mono-, bis-, and tris-adducts of $C_{120}O$, as well as the synthesis of regio-controlled functionalized dimeric fullerene oxides are considered in detail.

Preparation of $C_{120}O$

The solid state-thermolysis of C_{60}/C_{60}-oxide mixed powder described in the experimental section of this report yielded a product mixture containing $C_{120}O$ as main product, un-reacted C_{60}, as well as traces of dimeric and trimeric C_{60} poly-oxides of the form $C_{120}O_n$ (n = 2-5) and $C_{180}O_n$ (n = 2, 3) (*Figure 2.3* and *Figure 2.4*).

In general, the formation of dimeric and trimeric fullerene oxides can be related to thermal [3 + 2] cycloaddition reactions. Here, epoxyfullerenes react via epoxide ring-opening with an adjacent fullerene to form a rigid furan-type bridge linkage between the reactants [Tay98]. *Figure 3.1* illustrates the reaction mechanism using the formation of $C_{120}O$.

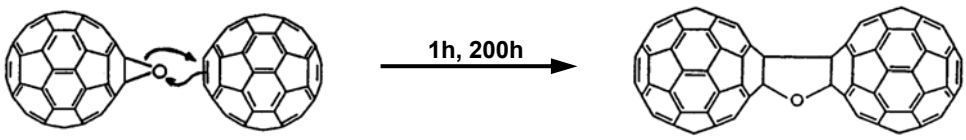

Figure 3.1. *Conjectured [3 + 2] cycloaddition mechanism for the formation of $C_{120}O$ from C_{60} and $C_{60}O$ [Tay98].*

The occurrence of dimeric and trimeric C_{60} poly-oxides was explained by the linking of two or three $C_{60}O_n$ (n = 0 - 3) monomer units, which were present in the reacting system. *Figure 1.5* illustrates chemical structures of monomeric, dimeric, and trimeric C_{60} poly-oxides.

$C_{120}O$ was dark brown to black as a solid. A solution of $C_{120}O$ in ODCB or toluene was brown-orange. By preparing saturated solutions, subsequently evaporating the solvent, and thereafter weighting the residue, the solubility of $C_{120}O$ was determined to be about 0.8 mg/mL in ODCB and 0.2 mg/mL in toluene.

Preparation of $C_{140}O$

The solid-state thermolysis of C_{70}/C_{70}-oxide mixed powder described in the experimental section of this report yielded a product mixture containing 35 % $C_{140}O$ as main product. This yield was determined by HPLC analysis using a Cosmosil Buckyprep column eluted with 1 mL/min toluene/ODCB (7/3, v/v) (*Figure 2.5*). According to the literature [Kud02], converting chemically pure $C_{70}/C_{70}O$ mixed powder by hydrothermal treatment or by solid state-thermolysis yielded a product mixture containing a total of 2-3 % dimeric C_{70} oxides. The yield of 2-3 % dimeric C_{70} oxides declared in the literature was based on a HPLC analysis using a Cosmosil Buckyprep column eluted with 1 mL/min toluene. To verify the origin of the significant difference in the yields of the syntheses, the product mixture of this work was additionally analyzed by HPLC using 1 mL/min toluene elution (*Figure 3.2*). This HPLC analysis resulted in a total of only 10 % dimeric C_{70} oxides. Therefore, the significant difference in the yields of dimeric C_{70} oxides declared in the literature and achieved in this work was ascribed to the different eluents used for the HPLC analyses. Different eluents lead to different results because larger fullerenes tend to be less soluble and as the solubility of fullerenes is far better in an ODCB/toluene mixture than in pure toluene.

The HPLC analysis of the product mixture using toluene elution showed four $C_{140}O$ peaks (*Figure 3.2*) and accordingly confirmed the formation of four $C_{140}O$ isomers. In this work, $C_{140}O$ was characterized as isomeric mixture.

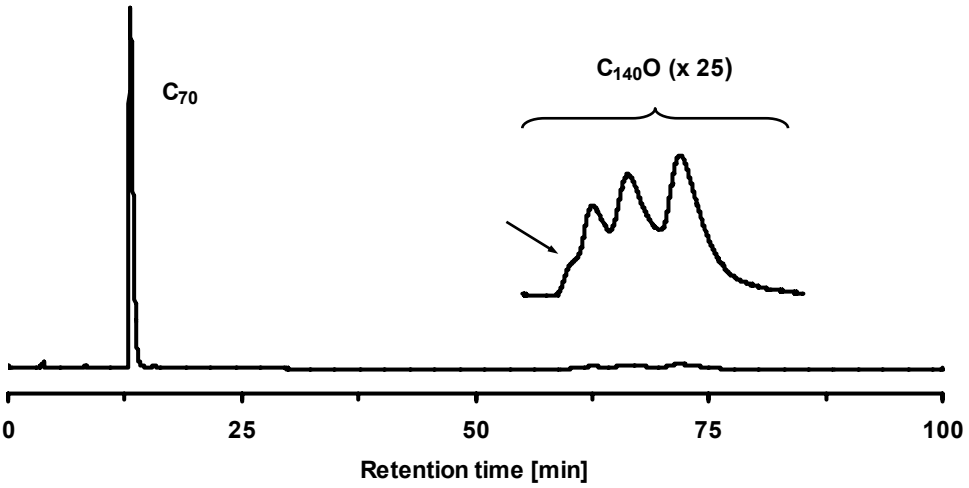

Figure 3.2. *HPLC chart of the reaction product of the C_{70}/C_{70}-oxide thermolysis (analytical Cosmosil Buckyprep column (4.6 x 250 mm²) eluted at 1 mL/min with toluene), detection at 330 nm).*

The product mixture obtained in this work contained $C_{140}O$ as the main product, as well as traces of dimeric and trimeric C_{70} poly-oxides of the form $C_{140}O_n$ (n = 2-5) and $C_{210}O_n$ (n = 2, 3) (*Figure 2.5* and *Figure 2.6*). The occurrence of theses compounds was explained by the linking of two or three $C_{70}O_n$ (n = 0-3) monomer units, which were present in the reacting system. Trimeric C_{70} fullerenes were unknown up to now.

$C_{140}O$ was dark brown to black as a solid. A solution of $C_{140}O$ in ODCB or toluene was brown-orange. The solubility of $C_{140}O$ in ODCB amounted at least 0.25 mg/mL. In toluene, the solubility clearly was lower than in ODCB.

Preparation of $C_{130}O$

The $C_{130}O$ synthesis described in the experimental section of this report yielded a product mixture containing the dimeric fullerene oxides $C_{130}O$ (20 %), $C_{120}O$ (20 %) and $C_{140}O$ (8 %), un-reacted C_{60} (30 %) and C_{70} (22 %), as well as traces of dimeric and trimeric fullerene poly-oxides of the form $C_{130}O_n$ (n = 2-5), $C_{120}O_n$ (n = 2-5), $C_{140}O_n$ (n = 2-4), $C_{180}O_n$ (n = 2, 3) and $C_{190}O_n$ (n = 2), as determined by HPLC (*Figure 2.7*) and MS analyses (*Figure 2.8*). The occurrence of dimeric and trimeric poly-oxides was explained by the linking of two or three monomeric fullerenes of the form $C_{60}O_n$ and $C_{70}O_n$ (n = 0-3), which were present in the reacting system. Trimeric fullerenes such as $C_{190}O_2$, in which C_{60} and C_{70} cages are linked, were unknown up to now.

The formation of $C_{120}O$ and $C_{140}O$ as by-products of the $C_{130}O$ synthesis was inevitable. However, the $C_{130}O$ yield of 20 % was satisfactory. Due to the similar solubility of $C_{120}O$, $C_{130}O$, and $C_{140}O$, an isolation of $C_{130}O$ by precipitation, which was used to isolate $C_{120}O$ and $C_{140}O$, was not possible. $C_{130}O$ had to be separated from $C_{120}O$ and $C_{140}O$ by preparative HPLC.

To verify the number of formed $C_{130}O$ isomers, $C_{130}O$ was analyzed by analytical HPLC using 1 mL/min toluene elution (*Figure 3.3*). This HPLC analysis showed three $C_{130}O$ peaks and accordingly verified three $C_{130}O$ isomers. The verification of three $C_{130}O$ isomers was in agreement with the literature [Eis98A]. In this work, $C_{130}O$ was characterized as isomeric mixture.

$C_{130}O$ was dark brown to black as a solid. A solution of $C_{130}O$ in ODCB or toluene was brown-orange.

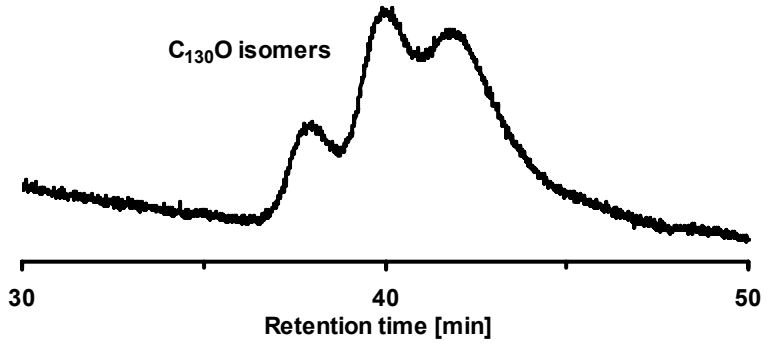

Figure 3.3. *HPLC chart of $C_{130}O$ (analytical Cosmosil Buckyprep column (4.6 x 250 mm²) eluted at 1 mL/min with toluene, detection at 330 nm).*

Diazoalkane Addition and Bingel Cyclopropanation Reaction on $C_{120}O$

The diazoalkane addition reaction and the Bingel reaction on $C_{120}O$ yielded product mixtures containing mono-, bis-, and tris-adducts of $C_{120}O$, un-reacted $C_{120}O$, as well as traces of dimeric and trimeric fullerene poly-oxides of the form $C_{120}O_nR_m$ and $C_{180}O_nR_m$ (R represents R´ or R´´) (*Figure 2.9*, *Figure 2.10*, *Figure 2.11*, and *Figure 2.12*). *Figure 1.11* illustrates the obtained mono-, bis-, and tris-adducts. The occurrence of dimeric and trimeric C_{60} poly-oxides and adducts of these poly-oxides in the product mixtures was due to the impurity of the $C_{120}O$ starting material by $C_{120}O_n$ and $C_{180}O_n$. The detection of functionalized trimeric fullerene oxides ($C_{180}O_nR_m$) is remarkable because these derivatives are the first functionalized trimeric fullerenes and indicate the possibility to synthesize higher, soluble fullerene oligomers.

The separation of the product mixtures by column chromatography yielded mono-, bis-, and tris-adduct fractions. *Figure 3.4* and *Figure 3.5* show mass spectra of the isolated mono-, bis-, and tris-adducts. *Figure 3.4* exemplarily shows the HPLC

analyses of the isolated fractions of the diazoalkane addition reaction. The mass spectra of the isolated fractions indicated a successful separation. Concluding, the separation method enables isolating preparative amounts of highly pure, functionalized fullerene dimers using conventional laboratory methods.

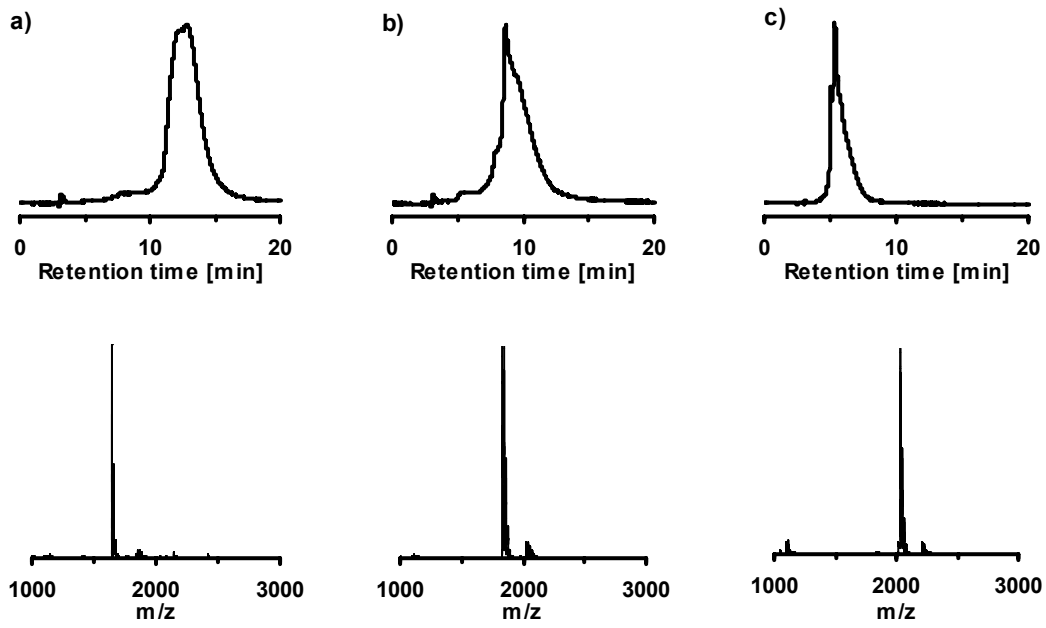

Figure 3.4. *HPLC charts (top, analytical Cosmosil Buckyprep column (4.6 x 250 mm²) eluted at 1 mL/min with toluene, detection at 330 nm) and mass-spectra (bottom) of a) the mono-, b) the bis-, and c) the tris-adduct fraction of the diazoalkane addition reaction on $C_{120}O$.*

To verify the number of formed isomers, the isolated $C_{120}O$ adducts were analyzed by analytical HPLC using 0.1 mL/min toluene/cyclohexane (1/1, v/v) elution. *Figure 3.5* exemplarily shows the HPLC analyses of the Bingel adducts. The analyses revealed five isomers for the mono-adduct (retention times [min]: 354, 368, 384, 416, 448) and seven isomers for the bis-adduct (retention times [min]: 93, 100, 107, 114, 121, 154, 167) of the diazoalkane addition reaction. For the Bingel-adducts, four mono-adduct isomers (retention times [min]: 242, 246, 255, 266) and ten bis-adduct isomers

(retention times [min]: 86, 90, 98, 107, 111, 122, 130, 235, 142, 152) were confirmed. The resolution of the method was not high enough to indicate the number of formed tris-adducts (*Figure 3.5*).

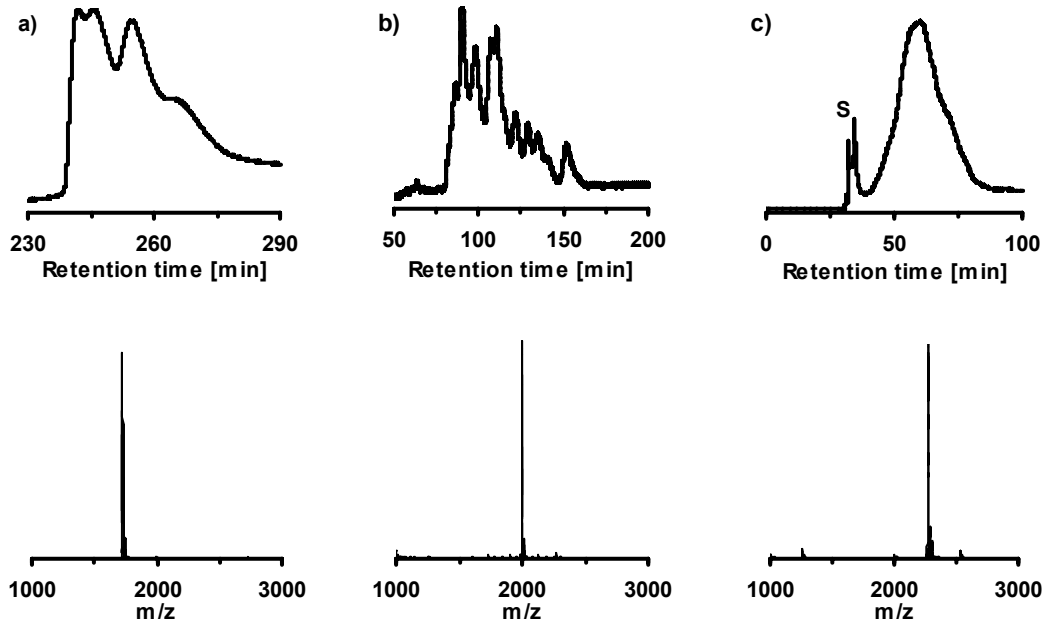

Figure 3.5. *HPLC charts (top, analytical Cosmosil Buckyprep column (4.6 x 250 mm²) eluted at 0.1 mL/min with toluene/cyclohexane (1/1, v/v), detection at 330 nm) and mass-spectra (bottom) of a) the mono-, b) the bis-, and c) the tris-adduct fraction of the Bingel reaction on $C_{120}O$.*

The mono-adducts **1** ($C_{120}OR'$) and **2** ($C_{120}OR''$) were characterized and applied as isomeric mixtures. The mono-adducts **1** and **2** were brown as solids and readily soluble in toluene, chlorobenzene, or ODCB. A solution of **1** in these solvents was orange to brown, a solution of **2** was wine red. After evaporation of the solvent of such a solution, **1** and **2** remained as homogeneous films.

Regio-controlled Functionalized Dimeric Fullerene Oxides

Figure 3.6 shows mass spectra of regio-controlled, mono- and bis-functionalized fullerene dimers synthesized by solid state-thermolysis of mixtures containing a functionalized epoxy-fullerenes and a reactant fullerene (*Figure 1.12*, *Figure 2.1*, *Figure 2.13*, and *Table 2.1*).

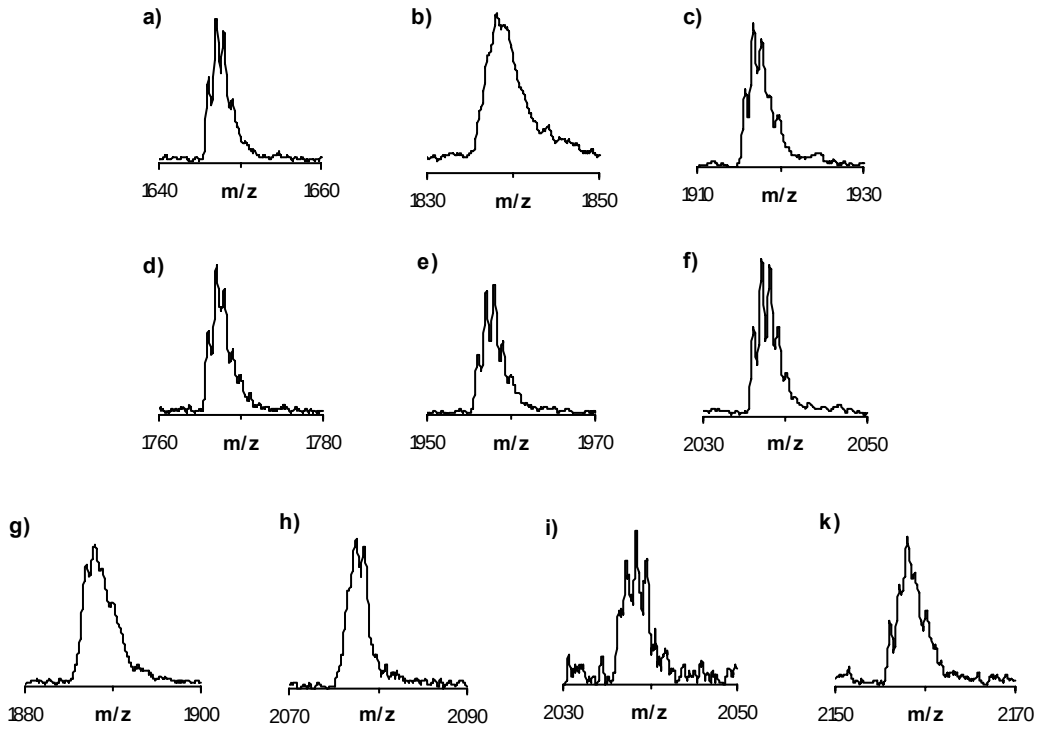

Figure 3.6. *Mass spectra of regio-controlled functionalized fullerene dimers. Characters a) to k) refer to Table 2.1.*

The results showed that the synthesis route allows controlling the functionalization of the cages of the dimeric fullerene oxides $C_{120}O$, $C_{130}O$, and $C_{140}O$. Yields of over 10 % were achieved without optimizing the syntheses. *Figure 3.7* exemplarily shows the HPLC analyses of the product mixtures of the reactions a), b), and e) specified in *Table 2.1*.

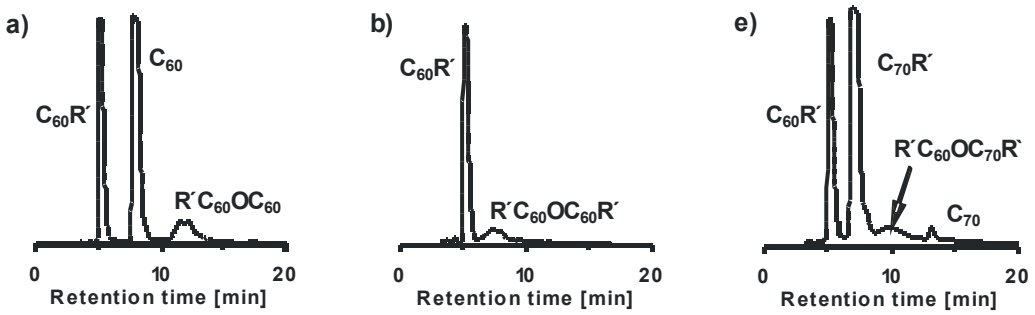

Figure 3.7. *HPLC charts of the product mixtures of the reactions a), b), and e) specified in Table 2.1.*

Remarkably, the synthesis route worked as well using the functionalized epoxy-fullerenes $R''C_{60}O$ and $R''C_{70}O$ illustrated in *Figure 3.8*.

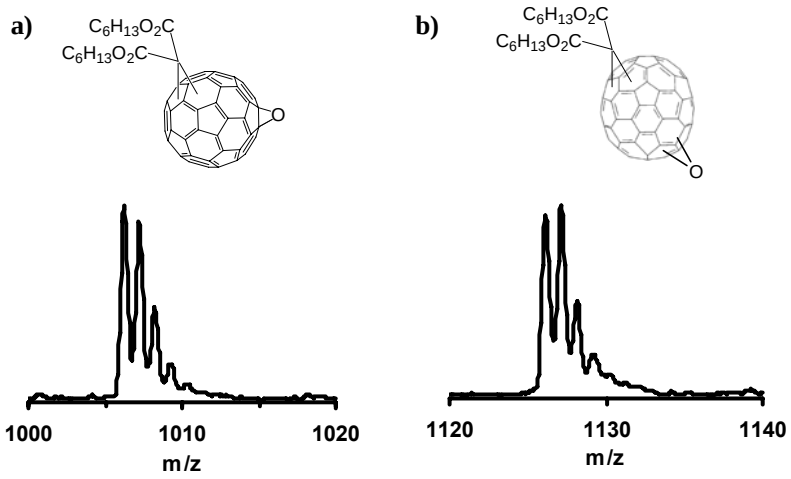

Figure 3.8. *Chemical structures and mass spectra of the functionalized monomeric epoxy-fullerenes a) $R''C_{60}O$ (1002 g/mol) and b) $R''C_{70}O$ (1126 g/mol).*

3.1.2. Physicochemical Characteristics of Dimeric Fullerene Oxides

In the following, oxidative and thermal stability, electronic absorption properties, and electron acceptor strength of the dimeric fullerene oxides $C_{120}O$, $C_{130}O$, and $C_{140}O$, and the $C_{120}O$ mono-adducts **1** ($C_{120}OR'$) and **2** ($C_{120}OR''$) are discussed in detail.

Oxidative and Thermal Stability

The oxidative and thermal properties of the dimeric fullerene oxides $C_{120}O$, $C_{140}O$, $C_{130}O$, **1** ($C_{120}OR'$), and **2** ($C_{120}OR''$) were investigated by thermogravimetric analyses (TGA) using synthetic air and nitrogen atmosphere. Comparison measurements were made with C_{60}, C_{70}, an equimolar C_{60}/C_{70} mixture, $C_{60}R'$, and $C_{60}R''$. The comparisons allowed the assessment of the relative stabilities of the compounds.

Figure 3.9 shows TG analyses recorded in synthetic air. The TGA traces of the dimers showed similar features. The traces showed a slight weight gain in the temperature range from 200 °C to 330 °C. This weight gain indicated the partial oxidation of the dimers by oxygen [Wie93]. With further increase of temperature, the weights initially decreased almost linearly up to about 400 °C and than still linearly but more rapidly. This two-stage weight loss indicated the oxidation of the compounds to CO and CO_2 [Wie93]. The comparison measurements showed qualitatively similar courses as the corresponding TGAs of the dimers, but the oxidation steps occured at higher temperatures. The partial oxidation occured in the temperature range from 300 °C to 400 °C. The gasification to CO and CO_2 started in the temperature range from 370 °C to 400 °C.

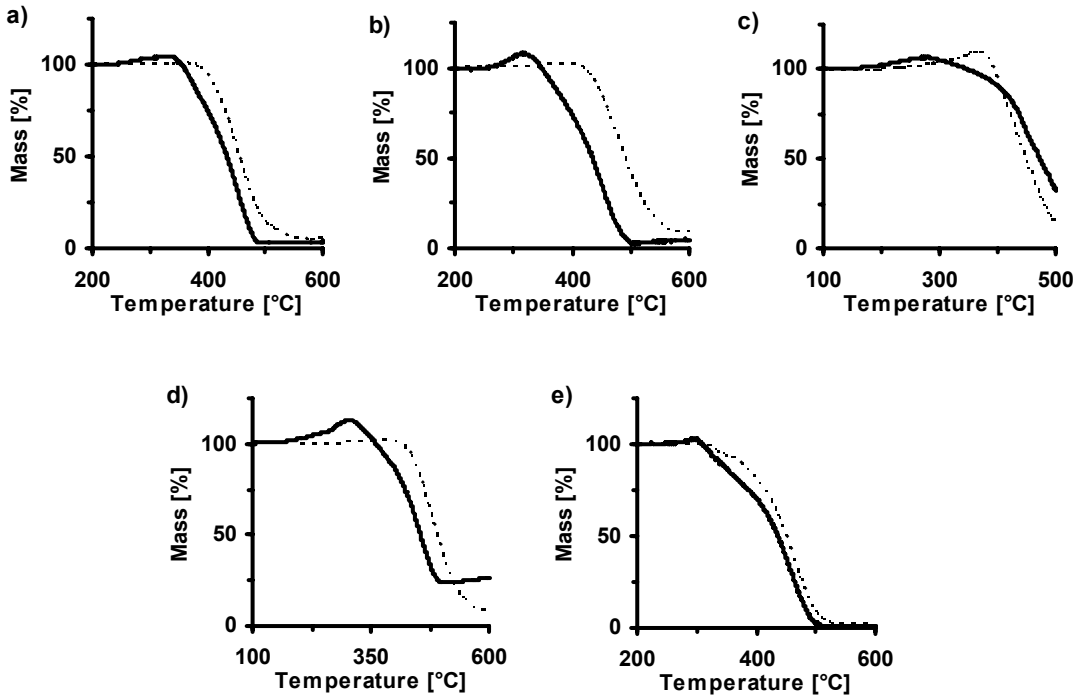

Figure 3.9. *TGAs recorded in synthetic air: a) $C_{120}O$ and C_{60}, b) $C_{140}O$ and C_{70}, c) $C_{130}O$ and an equimolar C_{60}/C_{70}-mixture, d)* ***1*** *($C_{120}OR'$) and $C_{60}R'$, and d)* ***2*** *($C_{120}OR''$) and $C_{60}R''$ (dimeric fullerene oxides: solid lines, monomeric fullerenes: dashed lines).*

Figure 3.10 shows the TG analyses recorded under nitrogen atmosphere. In the TGA traces of C_{60}, C_{70}, and $C_{60}R'$, the sample weights remained constant up to about 600 °C and then decreased nearly exponentially. The observed weight loss was attributed to sublimation [Muk01]. In the TGA curve of equimolar mixed C_{60}/C_{70}, the weight remained constant up to 580 °C and then decreased in two stages with the stage change occurring at 800 °C. The occurrence of two stages was explained by the different volatility of C_{60} and C_{70} [Gal92, Muk01]. In the TGA traces of the dimers $C_{120}O$, $C_{140}O$, $C_{130}O$, and **1**, the sample weights remained constant up to about 520 °C. With further increase of temperature, the weights steadily decreased with a distinct stage change at about 800 °C. Evidently, the compounds did not simply undergo a sublimation process, but also some other processes – presumably

dissociation and formation of larger fullerene structures by Diels-Alder-like reactions [Muk01] – occurred. In the TGA trace of $C_{60}R''$, the sample weight remained constant up to 300 °C. With further increase of temperature, the weight decreased with stage changes occurring at 400 °C and 800 °C. The TGA trace of **2** showed a qualitatively similar course as the TGA of $C_{60}R''$. In the TGA trace of **2**, the sample weight remained constant up to 250 °C and with further increase of temperature, the weight decreased with stage changes occurring at 400 °C and 550 °C. The course of the TGAs of $C_{60}R''$ and **2** were explained by thermal decomposition of the side chain (R´´), sublimation, and the formation of larger fullerene structures based on the formation of methanofullereneradicals as intermediate products [Dra00A, Dra00B]. *Figure 3.11* illustrates the formation of larger fullerene structures based on the formation of methanofullereneradicals.

All in all, the thermogravimetric analyses showed that both the oxidative and the thermal stability of the dimers were lower than that of the monomeric comparisson substances.

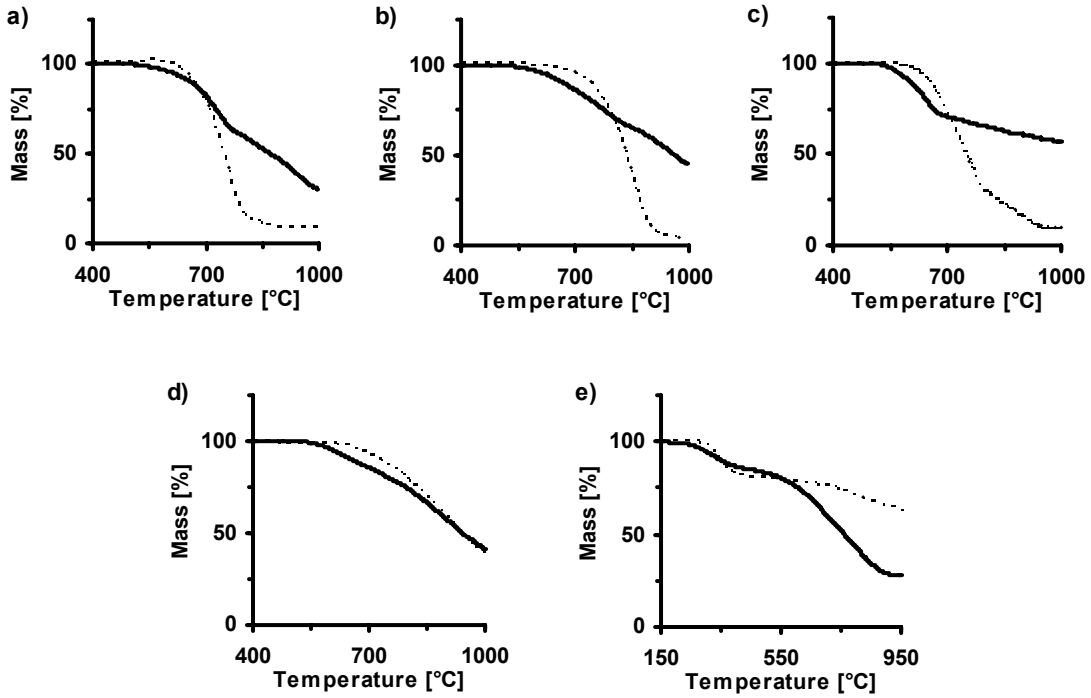

Figure 3.10. *TGAs recorded under nitrogen atmosphere: a) $C_{120}O$ and C_{60}, b) $C_{140}O$ and C_{70}, c) $C_{130}O$ and an equimolar C_{60}/C_{70}-mixture, d)* ***1*** *($C_{120}OR'$) and $C_{60}R'$, and d)* ***2*** *($C_{120}OR''$) and $C_{60}R''$ (dimeric fullerene oxides: solid lines, monomeric fullerenes: dashed lines).*

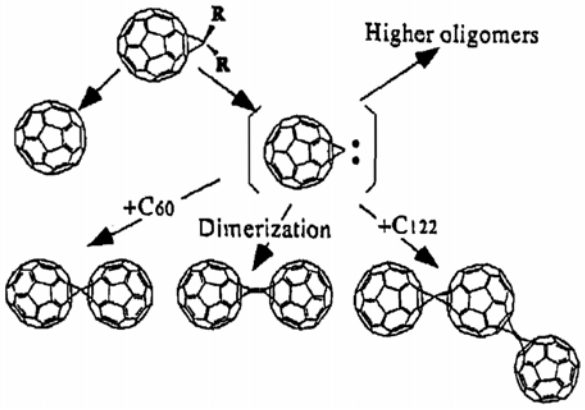

Figure 3.11. *Formation of larger fullerene structures based on the formation of methanofullereneradicals (R: -H, -$COOC_2H_5$, -Br) [Dra00B].*

To determine the stability of $C_{120}O$ and $C_{140}O$ in solution, carefully filtered ODCB solutions of $C_{120}O$ material (containing C_{60}, $C_{120}O$, and $C_{180}O_n$) and $C_{140}O$ material (containing C_{70} and $C_{140}O$) were stored at ambient temperature and atmosphere in darkness as well as under the influence of ambient light. *Figure 3.12* and *Figure 3.13* show the time-dependent HPLC-determined changes of the solution compositions.

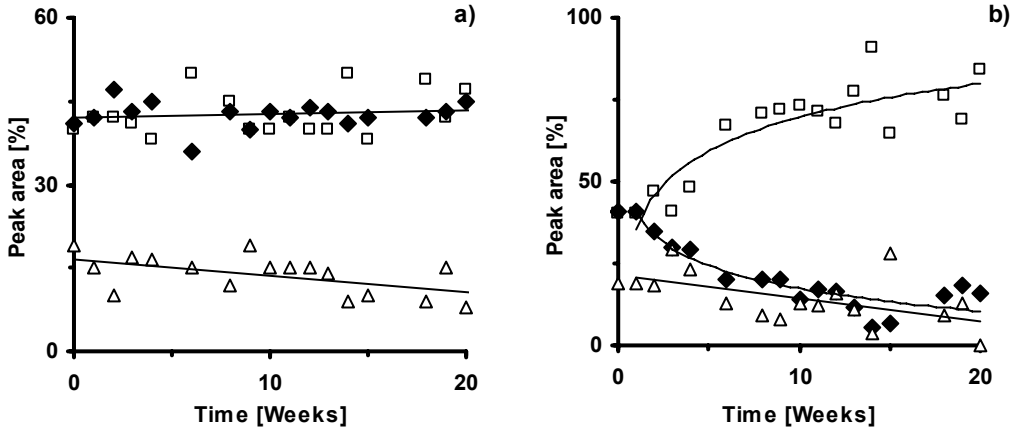

Figure 3.12. *HPLC-determined changes of a $C_{60}/C_{120}O/C_{180}O_n$ mixture dissolved in ODCB: a) in the dark and b) under ambient light (□ C_{60}, ♦ $C_{120}O$, Δ $C_{180}O_n$, analytical Cosmosil Buckyprep column (4.6 x 250 mm²) eluted at 1 mL/min with toluene/ODCB (7/3, v/v), detection at 330 nm).*

The studied dimeric and trimeric fullerene oxides ($C_{120}O$, $C_{180}O_n$, and $C_{140}O$) stored in the dark were stable for months (*Figure 3.12 a)* and *Figure 3.13*). For the solutions stored under the influence of light, the results were less definitive. *Figure 3.12 b)* and *Figure 3.13* show that the concentrations of monomeric fullerenes (C_{60} and C_{70}) increased and that those of dimeric and trimeric fullerene oxides ($C_{120}O$, $C_{180}O_n$, and $C_{140}O$) decreased. Additionally, the solutions coated the flask surfaces with a barely soluble brown-yellow film. The findings were explained by light-induced attachment of fullerene oxide colloids/aggregates to the glass surface of the flasks. For toluene

solutions of the fullerene oxide $C_{70}O$ such attachments were observed [Hey99]. A further explanation was light-induced oxidation of the fullerene oxides coming along with precipitation of the resulting poly-oxides. Above results showed that dimeric C_{60} and C_{70} fullerene oxides easier oxidize than C_{60} and C_{70}. Fullerene poly-oxides are more polar and consequently less soluble in ODCB than fullerene mono-oxides.

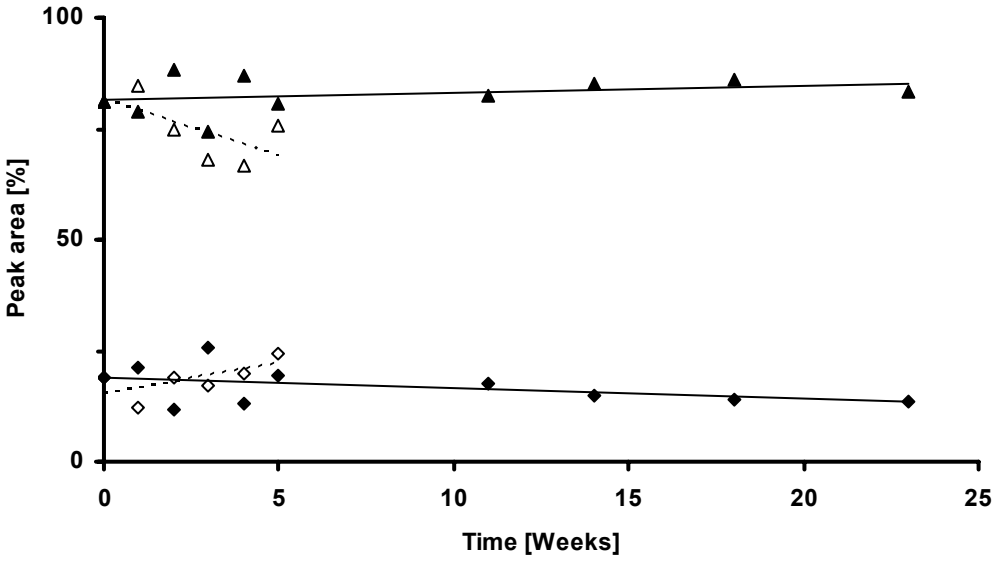

Figure 3.13. *HPLC-determined changes of $C_{140}O$ dissolved in ODCB: in the dark (filled symbols and under ambient light (not filled symbols), triangles: $C_{140}O$; diamonds: C_{70} (analytical Cosmosil Buckyprep column (4.6 x 250 mm²) eluted at 1 mL/min with toluene/ODCB (7/3, v/v), detection at 330 nm).*

Electronic Absorption Properties

Electronic absorption properties of $C_{120}O$, $C_{140}O$, $C_{130}O$, **1** ($C_{120}OR'$), and **2** ($C_{120}OR''$) were studied by UV-vis-spectroscopy on ODCB solutions of the compounds. *Figure 3.14* shows UV-vis spectra of the dimeric fullerene oxides $C_{120}O$, $C_{140}O$, $C_{130}O$, **1**, and **2**. Comparison measurements were made with C_{60}, C_{70}, an

equimolar C_{60}/C_{70} mixture, $C_{60}R'$, and $C_{60}R''$. Molar absorption values were scaled for comparison of the intensities.

In contrast to the comparison measurements, the spectra of the dimers were significantly broadened as the dimers were lower in symmetry than monomeric fullerenes. This was particularly valid for $C_{140}O$ and $C_{130}O$.

In the spectra of the C_{60} dimers $C_{120}O$, **1**, and **2**, the characteristic C_{60} UV band at 336 nm was blue shifted to 326 nm. The molar absorption of this band was approximately a factor two larger in the dimers than in the mononomeric C_{60} comparison compounds, suggesting nearly independent, superimposed absorptions by the two halves of the dimers. Throughout the visible region, the absorptions of the dimers $C_{120}O$, **1**, and **2** clearly exceeded the doubled absorptions of the comparison compounds. This enhanced absorption was attributed to the interaction of transition dipole moments of the two fullerene-cages of the $C_{120}O$ dimers [Bac01, Fuj02B]. The $C_{120}O$ dimers showed weak peaks at about 700 nm (*Figure 3.14* f)). Such weak peaks are typical of [6,6]-derivatized C_{60} species [Bac01].

In the spectra of $C_{140}O$ and $C_{130}O$, the prominent C_{70} absorption at 335 nm was greatly diminished. This is typical of [6,6]-derivatized C_{70} species [Smi96]. Throughout the visible region, the absorptions of $C_{140}O$ were approximately twice those of C_{70} and the absorptions of $C_{130}O$ were approximately those of an equimolar C_{60}/C_{70} mixture. This suggested independent, superimposed absorptions by the two halves of the dimers. The onset in the spectrum of $C_{140}O$ was at a longer wavelength (approx. 950 nm) compared to the onset in the spectrum of C_{70} (approx. 700 nm). This indicated that $C_{140}O$ has a smaller HOMO-LUMO gap than C_{70} [Leb00A]. The other dimers did not show a shift of the onset.

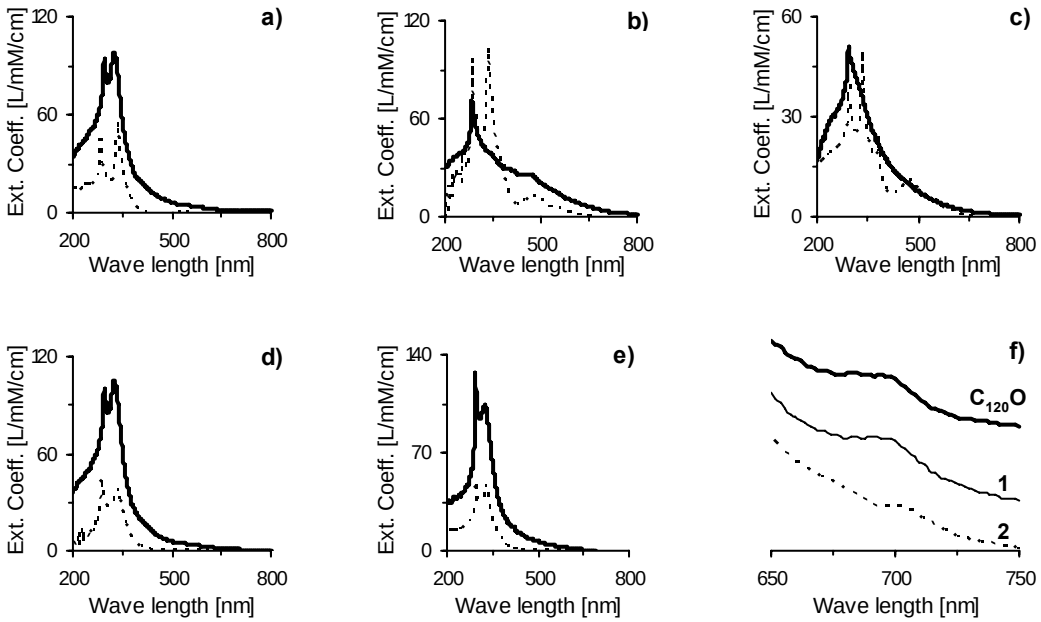

Figure 3.14. *UV-vis-spectra of a) $C_{120}O$ and C_{60}, b) $C_{140}O$ and C_{70}, c) $C_{130}O$ and an equimolar C_{60}/C_{70}-mixture, d) **1** ($C_{120}OR'$) and $C_{60}R'$, and e) **2** ($C_{120}OR''$) and $C_{60}R''$ (dimeric fullerene oxides: solid lines; monomeric fullerenes: dashed lines), as well as f) details of the UV-vis-spectra of $C_{120}O$, **1**, and **2** (ODCB solutions).*

Electron Acceptor Strength

The electron acceptor strength of the dimeric fullerene oxides $C_{120}O$, $C_{140}O$, $C_{130}O$, **1** ($C_{120}OR'$), and **2** ($C_{120}OR''$) was determined by cyclic voltammetry. *Figure 3.15* exemplifies CVs of the studied dimers. For all dimers, at least one chemically reversible and electrochemically quasi-reversible reduction and an associated first half-wave reduction potential (E^1_{red}) was proven.

The electron acceptor strength of a compound increases with its first half-wave reduction potential (E^1_{red}). *Table 3.1* shows the first half-wave reduction potentials (E^1_{red}) of the dimers $C_{120}O$, $C_{140}O$, $C_{130}O$, **1,** and **2** as determined by CV. For comparison, the first half-wave reduction potentials of C_{60}, C_{70}, $C_{60}R'$, and $C_{60}R''$, as

well as literature data are shown in *Table 3.1* too. The E^1_{red} values of $C_{120}O$, C_{60}, C_{70}, $C_{60}R'$, and $C_{60}R''$ measured in this work fairly agreed with the literature data.

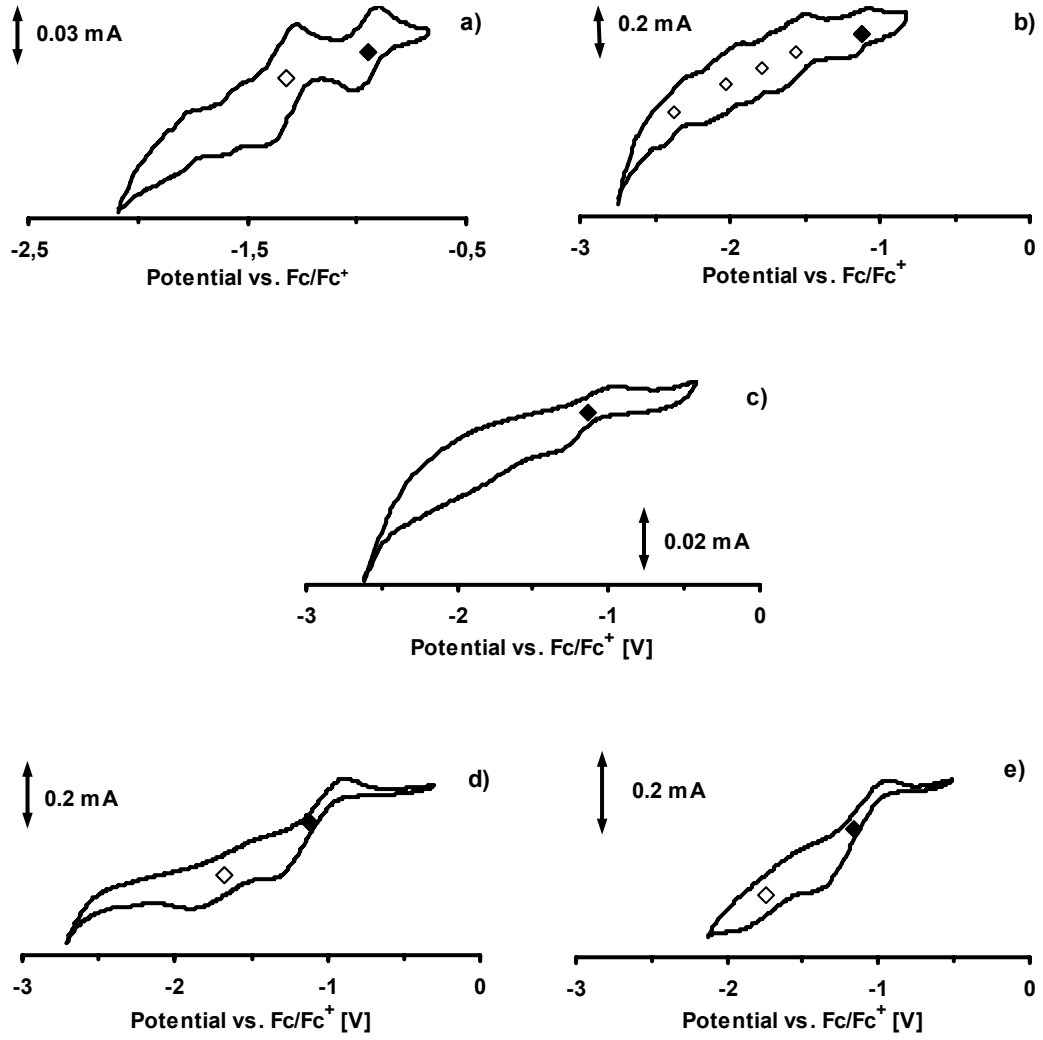

Figure 3.15. *CVs of a) $C_{120}O$, b) $C_{140}O$, c) $C_{130}O$, d)* ***1*** *($C_{120}OR'$), and e)* ***2*** *($C_{120}OR''$): ♦ first and ◊ subsequent half-wave reduction potentials. Experimental conditions: glassy carbon as working electrode, Pt-wire as pseudo reference electrode, Pt-foil as counter electrode; (TBA)PF_6 (tetrabutylammonium hexaflourophosphate, 0.1 M) as supporting electrolyte, deaerated toluene/acetonitrile (4/1, v/v) as solvent, scan rate 50 mV/s, room temperature, ~0.2 mM analyte.*

The E^1_{red} potentials of the studied compounds showed only minor differences. However, the data indicated that the C_{60} derivatives ($C_{60}R'$ and $C_{60}R''$) and the $C_{120}O$ derivatives (**1** and **2**) are less prone to reduction (i.e. show a negative shift in the E^1_{red} value) compared to C_{60} and $C_{120}O$. Such a trend is already well-known for monomeric fullerenes [Bal96] and here a similar trend was confirmed for $C_{120}O$ fullerenes.

Table 3.1. *First half-wave reduction potentials (E^1_{red}) as determined in this work and corresponding literature data (experimental conditions as indicated in Figure 3.15, all data in V vs. Fc/Fc^+), [a)] isomeric mixture, [b)] double peak, indicating the sequential addition of electrons to the two fullerene cages, proven after deconvolution of the CV, [c)] $R'' = C(COOC_2H_5)_2$.*

Compound	**$C_{120}O$**	**$C_{140}O$**[a)]	**$C_{130}O$**[a)]	**1**[a)]	**2**[a)]
E^1_{red}	-0.95	-1.12	-1.14	-1.12	-1.16
E^1_{red} (literature)	-0.84; -0.88 [b)] [Bal96] -1.1 [Dun03]	-	-	-	-
Compound	**C_{60}**	**C_{70}**		**$C_{60}R'$**	**$C_{60}R''$**
E^1_{red}	-1.12	-1.13		-1.14	-1.15
E^1_{red} (literature)	-0.77 – -1.17 [Kad00]	-0.85 – -1.02 [Kad00]		-1.14 [Hum95] -1.08 [Koo06]	-1.16 [c)] [Kad00]

3.1.3. Application of Dimeric Fullerene Oxides

The well-soluble $C_{120}O$ mono-adducts **1** ($C_{120}OR'$) and **2** ($C_{120}OR''$) were applied as electron acceptor in bulk heterojunktion (BHJ) polymer solar cells together with the semiconducting polymer P3HT (*Figure 1.14*) electron donor.

Figure 3.16 exemplifies current density-voltage curve of such devices. The devices showed normal curve progression. As determined by light optical microscopy, the

photoactive composite layers of the devices were homogenous and showed no crystallization, not at the boundary of the layer either (*Figure 3.18*).

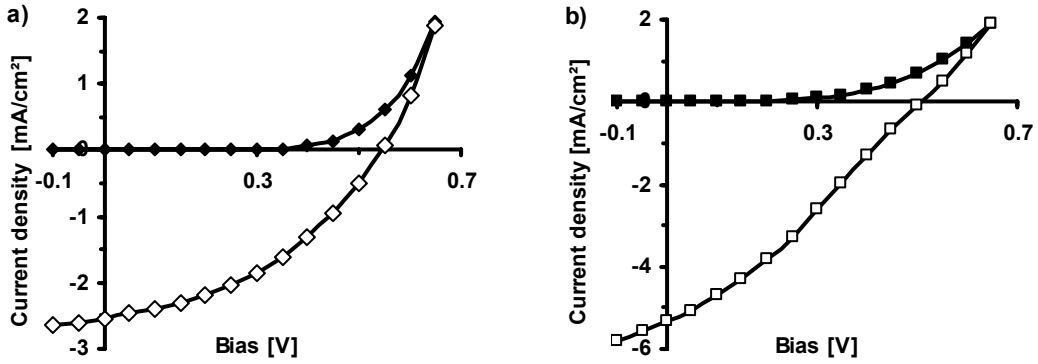

Figure 3.16. *a) Current density-voltage characteristic of a P3HT:**1** (1:0.8, w/w) device under illumination (◊) and in the dark (♦). Device parameters: I_{SC} [mA/cm²] = 2.54 (short circuit current), V_{OC} [mV] = 544 (open circuit voltage), FF [-] = 0.41 (filling factor), $\eta_{AM1.5}$ [%] = 0.57 (power conversion efficiency). b) Current density-voltage characteristic of a P3HT:**2** (1:0.8, w/w) device under illumination (□) and in the dark (■). Device parameters: I_{SC} [mA/cm²] = 5.31, V_{OC} [mV] = 524, FF [-] = 0.3, $\eta_{AM1.5}$ [%] = 0.82.*

The maximum photovoltaic power conversion efficiency of the devices was about 0.8 %. Considering that the performance of a BHJ solar cell has to be individually optimized for each and every materials combination [Hop04, Hop06], the results of this very initial introduction of well soluble dimeric fullerenes to organic electronics was successful.

Using light-induced electron spin resonance (LESR), photo-induced intermolecular electron transfer was proven for photoactive blends made of **1** as electron acceptor and P3EH-PPV (*Figure 1.14*) as electron donor. *Figure 3.18* shows an obtained X-band LESR spectrum. The LESR signals indicated positive polarons ($P^{+\bullet}$) on P3EH-PPV chains ($g_{iso} = 2.00293$) and anion radicals ($\mathbf{1}^{-\bullet}$) of **1** ($g_z = 1.9983$) (the

signal with $g_x \approx 2.0002$ corresponded to anion radicals of [60]PCBM present in the sample as impurity). The comparison of the integral intensity of the $P^{+\bullet}$ and the $\mathbf{1}^{-\bullet}$ signal showed an effective bimolecular charge separation process.

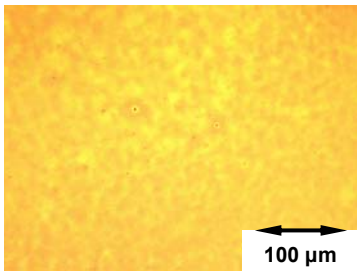

Figure 3.17. *Light optical microscope image of a P3HT:**2** blend (1:0.8, w/w).*

All in all, the well-soluble dimeric fullerene oxides **1** and **2** enable studying the impact of longish fullerene oligomers on the performance of fullerene-based organic electronics. In particular **1** enables a direct comparison to the most frequently used [60]PCBM.

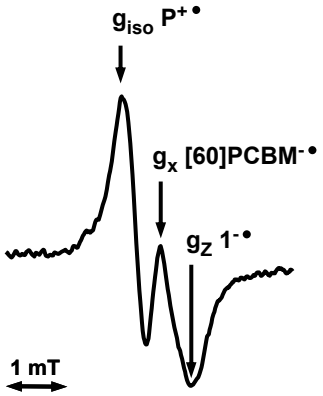

Figure 3.18. *Light induced X-band ESR spectra of a P3EH-PPV:**1** blend (1:1, w/w, film thickness 0.4 µm, recorded under Xe-lamp illumination (0.1 W/cm^2) at 77 K.*

3.2. Well-aligned MWCNT Arrays

In this chapter, fabrication, characteristics, and application of well-aligned MWCNT array electrodes developed in this work are extensively discussed.

3.2.1. Preparation of Well-aligned MWCNT Arrays

Well-aligned MWCNT arrays were directly grown on silica substrates by thermal chemical vapor deposition (CVD) at 900 °C using ferrocene as catalyst and benzene as carbon source. The morphology of the produced MWCNT arrays was investigated by scanning- (SEM) and trans-electron (TEM) microscopic analyses. *Figure 1.15* shows a typical morphology of the prepared well-aligned MWCNT arrays.

The MWCNT arrays contained by-products in the form of amorphous carbon and metal catalyst residue encased in the nanotube morphology as iron nanoparticles (*Figure 3.19*). The deposit thickness of the MWCNT arrays as determined by SEM ranged from 10-50 µm. The MWCNT were curly indicating that the tubes contained defects (*Figure 3.20*). The MWCNTs consisted of several tubes (*Figure 1.15* and *Figure 3.19 c)*). The diameters of the MWCNTs as determined by TEM ranged from 10 to 200 nm. The absolute mass of the MWCNT arrays as determined by weighting the substrates before and after the deposition of the MWCNTs ranged from 0.05-0.3 mg. The specific deposit mass of the MWCNT arrays was estimated by putting the deposit mass of the arrays in relation to the geometric area of the silica substrates and ranged from about 0.5 to 3.0 mg/cm².

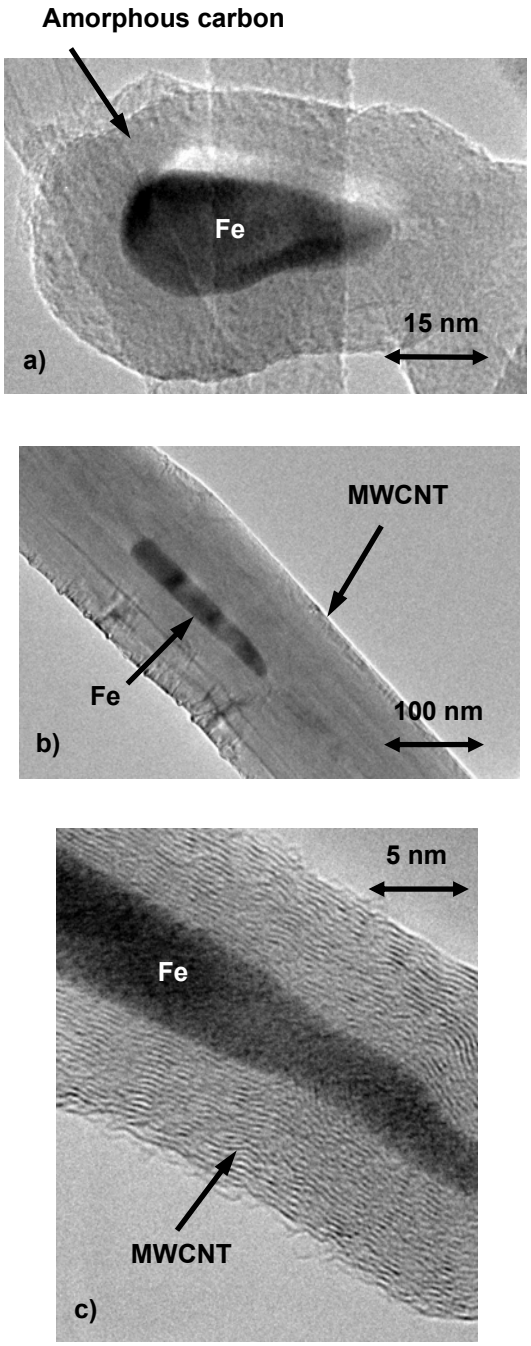

Figure 3.19. *TEM images of MWCNTs indicating impurities.*

The deposit thickness linearly depended on the deposited mass (*Figure 3.21*). Therefore, difference weighting was an easy way to estimate the deposit thickness of the MWCNT arrays. The deposit thickness increased with the reaction time (i.e. the addition time of the ferrocene solution) (*Figure 3.21*). A second, less quantifiable but also important synthesis parameter influencing the deposit thickness was the exact position of the substrates in the quartz tube.

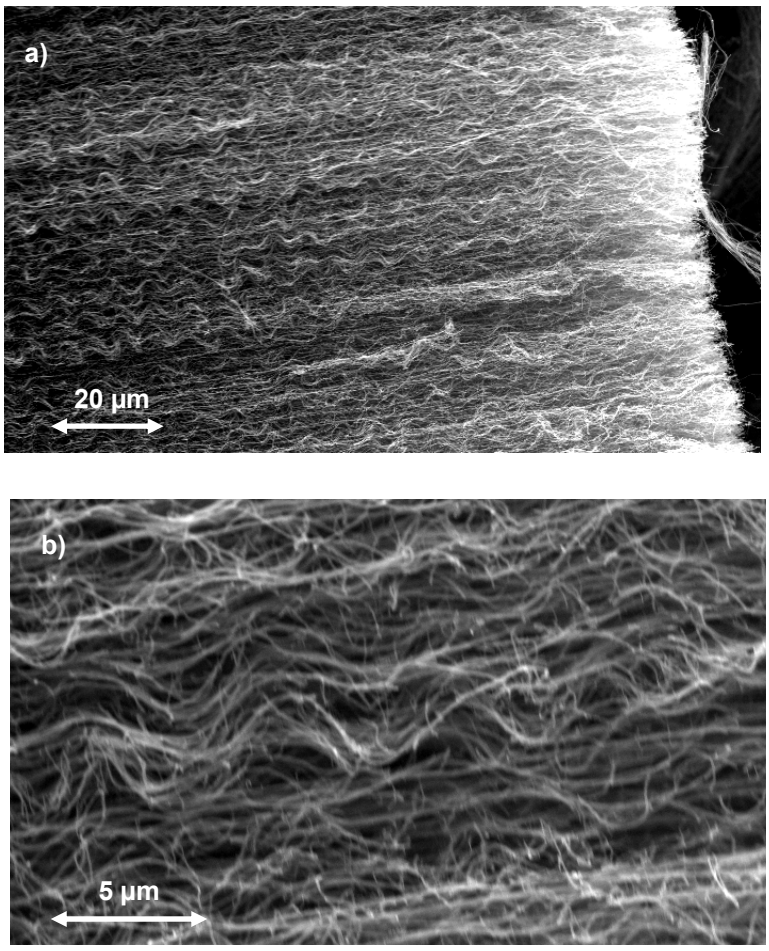

Figure 3.20. *SEM images of a well-aligned MWCNT array exemplifying the curly, defect rich structure of the MWCNT arrays.*

To remove metal catalyst residue and carbonaceous by-products, the MWCNT array electrodes were purified in aqueous 0.1 M HCl solution by repeated potential cycling (15-20 cycles) between -0.7 and 1.5 V vs. 3 M KCl-Ag/AgCl. *Figure 3.22* shows a typical set of CVs recorded during such a procedure. The course of the CVs was fairly complex. Various oxidation and reduction peaks occured in the CVs. Potential and current of all peaks depended on the cycle number. Continuous potential cycling finally resulted in a stable and reproducible current response with comparatively weak oxidation and reduction peaks (*Figure 3.22 b)*).

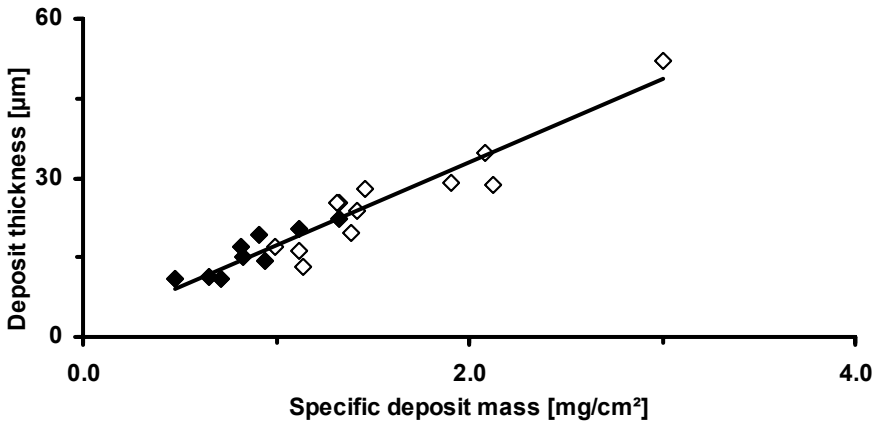

Figure 3.21. *Deposit thickness in dependence on the specific deposit mass of the MWCNT arrays: ♦ 6 min and ◊ 12 min reaction time.*

The complex course of the CVs was a result of an interaction between the oxidation of amorphous carbon and that of iron nanoparticles. Highly disordered carbon materials like amorphous carbon show a lower oxidative stability than carbon materials with fewer defects like CNTs. Thus, during repeated potential cycling carbonaceous by-products were oxidized resulting in an incremental removal or damage of the amorphous carbon. As a consequence, iron nanoparticles were exposed to the HCl solution, accordingly participated in electrochemical oxidation and

reduction reactions, and were finally dissolved in the solution. *Figure 3.23* shows that the iron concentration in the HCl solutions increased with the cycle number. The removal of carbonaceous by-products is discussed in the literature [Fan04].

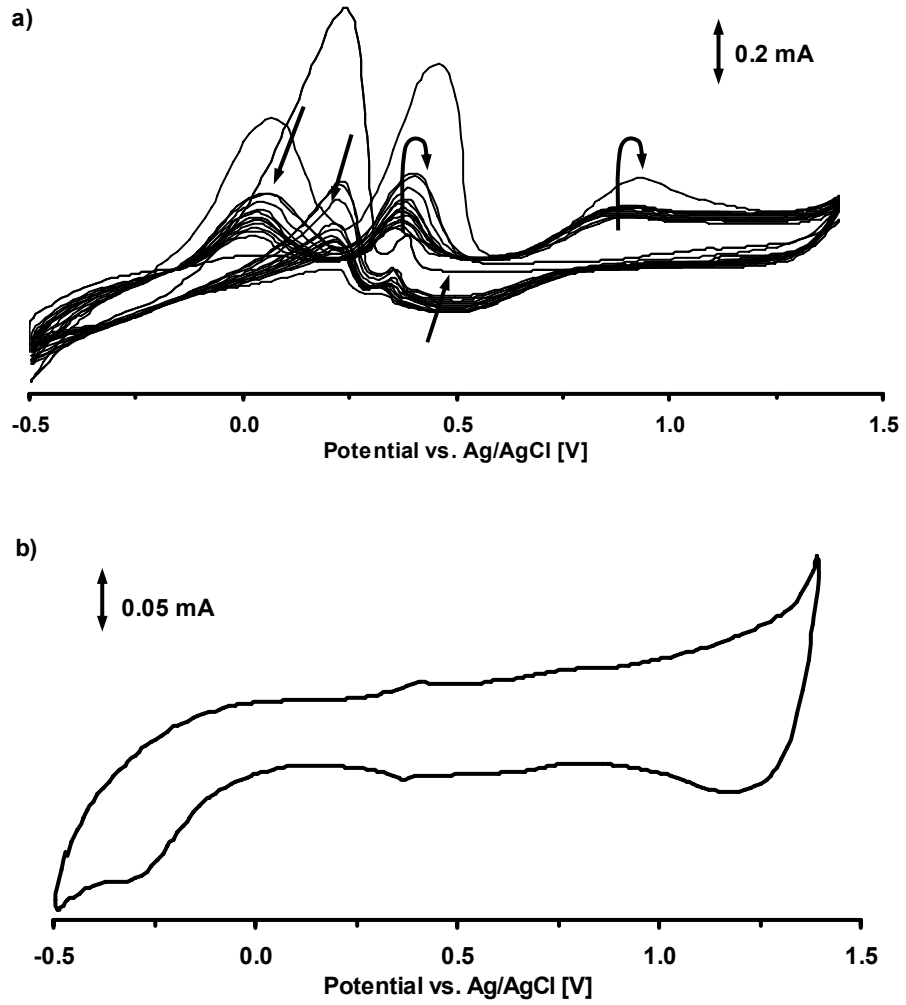

Figure 3.22. *a) Set of CVs recorded during repeated potential cycling a MWCNT array electrode in 0.1 M HCl (The arrows label the course of the peak currents). b) Last cycle of the treatment (counter electrode: Pt-foil, sweep rate 100 mV/s).*

All in all, electrochemically induced purification of as-grown MWCNT arrays represented a mild and on-line controllable method of purification in one exclusive

step and is therefore an attractive option to commonly used wet and gas phase purification, in particular for electrochemical applications of MWCNT arrays.

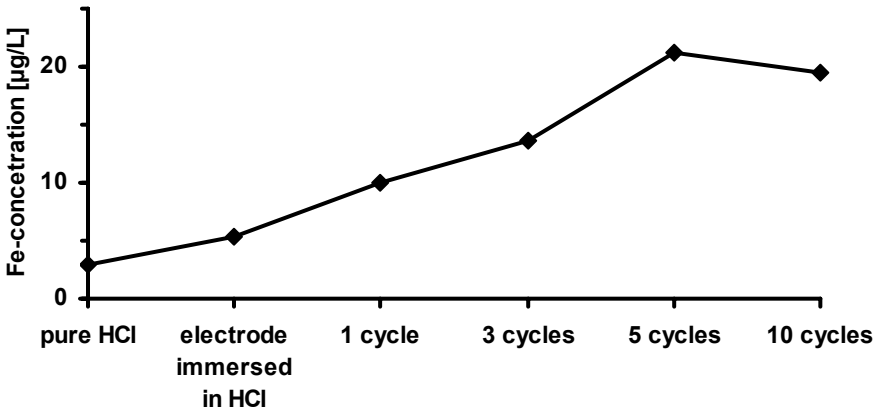

Figure 3.23. *Dependence of the Fe-concentration in a 0.1 M HCl solution on the cycle number of the CV-induced purification of a MWCNT array (determined by atomic absorption spectroscopy (AAS)).*

3.2.2. Electrochemical Characteristics of MWCNT Array Electrodes

In the following paragraphs, capacitive and electron transfer (faradaic) characteristics of the well-aligned MWCNT electrodes are considered in detail.

Capacitive Characteristics

To analyze capacitive characteristics of the MWCNT electrodes, CV and EIS measurements were carried out in aqueous 0.1 M KCl solutions.

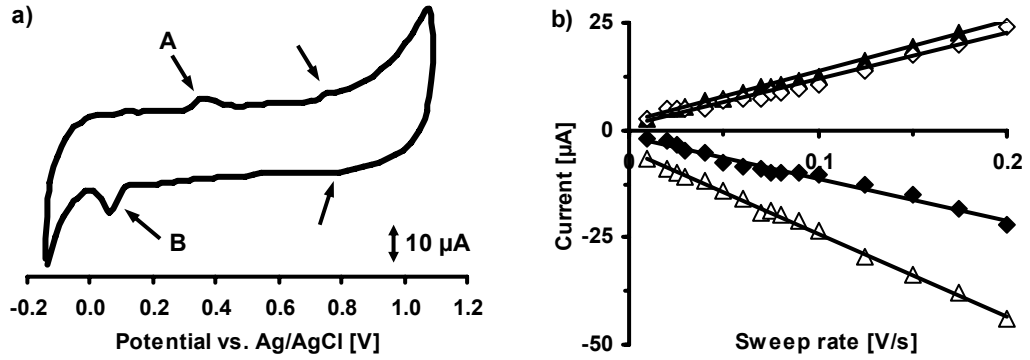

Figure 3.24. *a) CV of a MWCNT electrode (0.96 mg/cm²) in 0.1 M KCl (counter electrode: Pt-foil, sweep rate 60 mV/s), b) sweep rate-dependent anodic and cathodic currents of a MWCNT electrode (0.096 mg/cm²) in 0.1 M KCl (0.5 V vs. Ag/AgCl (◊ and ♦), peaks A (▲) and B (Δ) indicated in Figure 3.24 a)).*

Figure 3.24 shows a typical CV of a MWCNT electrode recorded in aqueous 0.1 M KCl solution. The anodic and cathodic current responses of the MWCNT electrodes were stable, reproducible, well-separated and showed weak and broad oxidation and reduction waves (marked by arrows in *Figure 3.24*). The anodic and cathodic current linearly depended on the voltage sweep rate. This is exemplified in *Figure 3.24 b)* for a fixed potential of 0.5 V vs. Ag/AgCl and for the peaks A and B indicated in *Figure 3.24 a)*. This linear dependence ruled out diffusion-controlled processes and indicated surface charging. Concluding, the weak redox waves originated from surface faradic reactions of redox active surface functional groups introduced during the preparation and from catalyst residue encased in the MWCNT morphology as iron nanoparticles (*Figure 3.19*). The currents were consequently attributed to a capacitance due to the formation of an ionic double-layer at the electrode/electrolytic solution interface – being proportional to the electrochemically active surface area – and pseudocapacitances due to surface faradic reactions of redox active surface functionalities [Li02, Che02, Bar00, Kim06].

At a potential of 0.5 V vs. Ag/AgCl, the capacitance C of the electrodes were estimated according to $C = 0.5 (I_a + |I_c|)/\nu$), where I_a and I_c were the anodic and cathodic voltammetric currents and ν was the sweep rate [Kim06]. The capacitance of the MWCNT electrodes linearly increased with the specific deposit mass of the MWCNT arrays (*Figure 3.25*)). Concluding, the full amount of the deposited mass contributed to the capacitance of the MWCNT electrodes. The average gravimetric capacitance of the electrodes was 1.6 F/g.

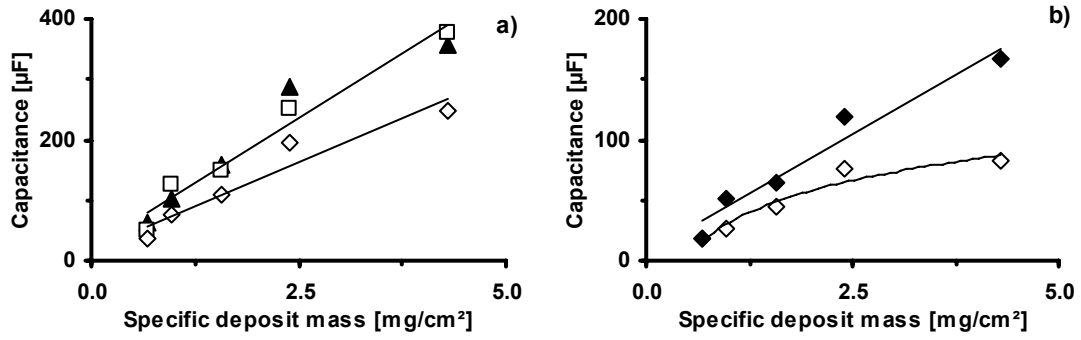

Figure 3.25. *Specific deposit mass-dependent capacitance of MWCNT electrodes in 0.1 M KCl: a) over-all capacitance as determined by CV (□), the low-frequency impedance data (▲), and the equivalent circuit A1 shown in Figure 3.29 (◊), b) capacitance as determined by CPE1 (◊) and CPE2 (♦) of equivalent circuit A1 shown in Figure 3.29 (0.1 M KCl).*

Using the area-related (specific) capacitance of a glassy carbon electrode (200 µF/cm²) as reference, the electrochemically active surface area of the electrodes was estimated [Sto03]. The specific active surface area of the MWCNT arrays – as determined by putting the active surface area of the arrays in relation to the geometric area of the silica substrates – was a multiple of the geometric area and increased systematically with the specific deposit mass and consequently with the deposit thickness (*Figure 3.26*).

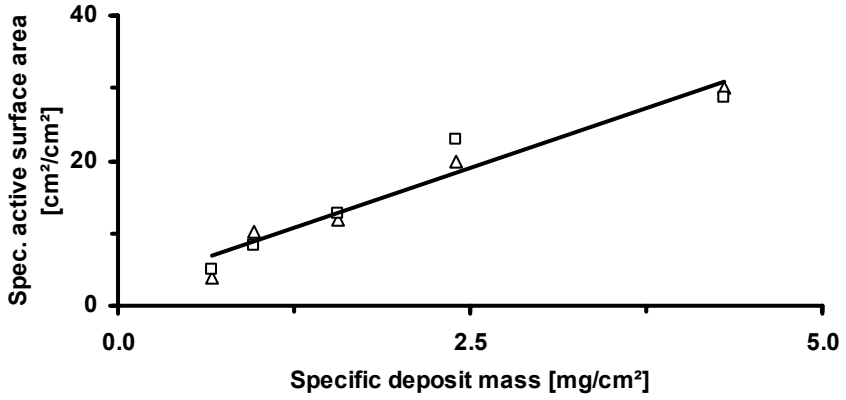

Figure 3.26. *Specific active surface area as determined by CV (Δ) and EIS (□) in dependence on the specific deposit mass of the MWCNT arrays.*

Figure 3.27 shows a typical Nyquist plot of the frequency depended impedance of a MWCNT electrode in aqueous 0.1 M KCl solution. The impedance spectra of the MWCNT electrodes showed the characteristic inflected form of porous capacitor electrodes [Bis00, Bar05].

At high frequencies (*Figure 3.27 a)*), the impedance of the MWCNT electrodes gave a straight line with a slope of about 45°, which was characteristic (at such frequencies) of porous electrodes. This porous-electrode effect was associated with a distributed resistance/capacitance (RC) network originating from the structural complexity of the porous MWCNT electrodes. The high-frequency real-axis intercept served to calculate the resistance R_s caused by the electrolytic solution (*Figure 3.27 a)*).

At low frequencies (*Figure 3.27 b)*), the impedance of the MWCNT electrodes gave an almost vertical line, in which almost pure capacitive behavior was manifested. Extrapolating the low frequency branch to the real axis gave an intercept, which equaled the sum of the solution resistance R_s and the effective internal resistance of

the distributed RC network of the porous electrodes R_{int} (*Figure 3.27 a)*) [Bar05]. The graphically determined internal resistance of the MWCNT electrodes decreased with increasing specific deposit mass and consequently with increasing deposit thickness of the MWCNT arrays (*Figure 3.28*). This indicated a deposit thickness-dependent morphology, which was attributed to the not finally clarifed growth mechanism of MWCNT arrays [Kap08].

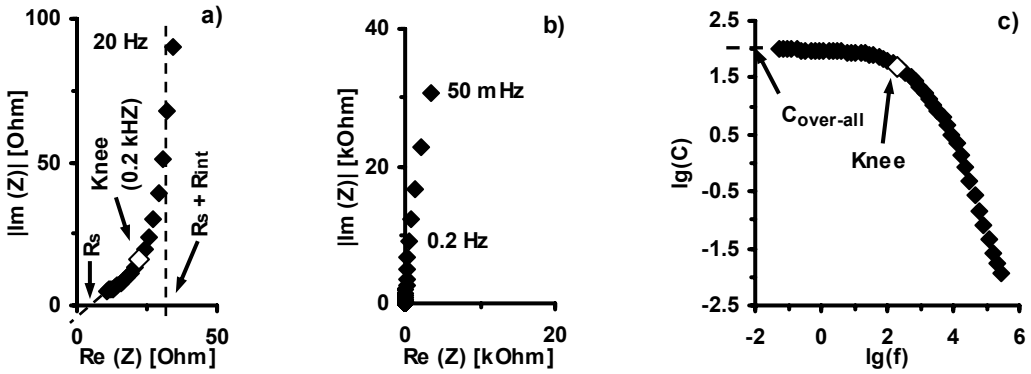

Figure 3.27. *a) High-frequency impedance, b) low-frequency impedance, and c) dispersion of capacitance with frequency of a MWCNT electrode (0.096 mg/cm², 0.1 M KCl, 0.5 V vs. Ag/AgCl, 10 mV amplitude sinusoidal wave, counter electrode: Pt-foil).*

The transition between the high- and the low-frequency region was characterized by a knee (*Figure 3.27 a)*). The intersection of the high- and the low-frequency branch defined the corresponding ‘‘knee frequency”. Above this characteristic frequency, the penetration depth of the modulating signal down the pore was shorter than the pore`s depth and the porous-electrode effect appeared. Below this frequency, the penetration depth of the modulating signal approached the pore`s depth, the electrode started to behave like a flat surface and capacitive behavior prevailed [Bar05, Bar03]. Therefore, the knee frequency was related to the deposit thickness of the electrodes.

Figure 3.28 shows that the knee frequency decreased with increasing specific deposit mass and consequently with increasing deposit thickness of the MWCNT arrays.

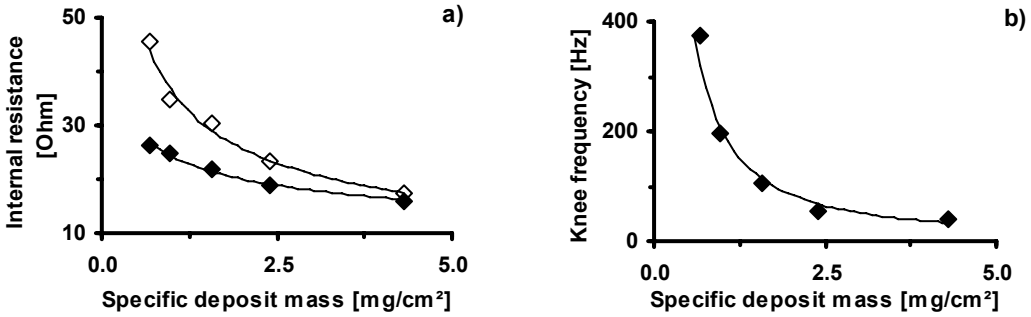

Figure 3.28. *a) Specific deposit mass-dependent internal resistance of MWCNT electrodes as determined graphically (♦) and by equivalent circuit A1 shown in Figure 3.29 (◊), 0.1 M KCl, 0.5 V vs. Ag/AgCl, b) specific deposit mass-dependent knee frequency of MWCNT electrodes.*

The frequency dependence of the capacitance was evaluated from the impedance data according to $C = -1/(\omega\, Im(Z)) = -1/(2\pi f\, Im(Z))$, where ω was the angular frequency and $f = \omega/(2\pi)$ the frequency of a measuring point and Im(Z) represented the imaginary part of the complex impedance at this frequency [Bar05]. Consistent with the porous nature of the electrodes, a dispersion of the capacitance with frequency was observed (*Figure 3.27c)*) [Bar03, Bar05]. As the penetration depth of the modulation signal decreased with increasing frequency, the capacitance increased with decreasing frequency but reached an almost constant value below the knee frequency, when the penetration depth of the modulation signal approached the pore`s depth and the over-all capacitance of the electrodes was exhausted. The weak frequency dependence at low frequencies – which caused the slightly inclined line at low frequencies in the Nyquist plot (*Figure 3.27 b)*) – was a deviation from the ideal

capacitance behavior and was attributed to the surface roughness of the MWCNT arrays (*Figure 3.27*) and the dispersion of pseudocapcitance with frequency [Bar05].

The over-all capacitance of the MWCNT electrodes as determined from the low-frequency impedance data (*Figure 3.27 c)*) was consistent with that determined from the CV experiments (*Figure 3.25*). Consequently, the specific surface area determined from the impedance data agreed well with that determined by CV (*Figure 3.26*).

Based on the above analyses of the CV and EIS measurements, the impedance spectra of the MWCNT electrodes were modeled with the equivalent circuit shown in *Figure 3.29*.

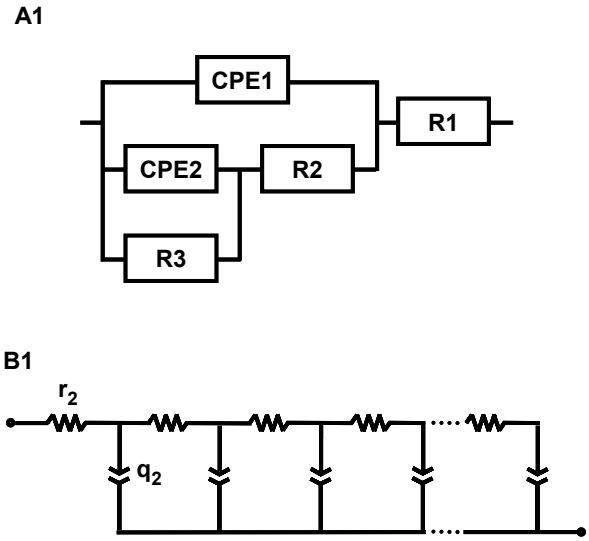

Figure 3.29. *Equivalent circuits used to model the capacitive impedance response of MWCNT array electrodes: ladder (A1) and transition line model (B1) (circuit elements as explained in the main text).*

Equivalent circuit A1 was a ladder consisting of the following elements [Bar05]: R1 was a faradaic resistance representing the bulk solution resistance. CPE1 was a constant-phase element representing the ionic double-layer and the pseudocapacity at

the macroscopic (external) electrode/electrolytic solution interface. R2 was a faradaic resistance associated with the internal resistance of the porous electrodes. CPE2 was a constant-phase element representing the ionic double-layer and the pseudocapacity at the internal surface of the porous electrodes. R3 was a potential-dependent leakage resistance. Constant-phase elements representing non-ideal capacitors were used to model ionic double-layers and pseudocapacitances to account for dispersive capacitance due to roughness of the electrode surface and frequency dispersion of pseudocapacitance. The impedance of a CPE was given by $Z_{CPE} = 1/(\omega_0 Q (i \omega/\omega_0)^{\alpha})$, where Q was a constant combining resistive and capacitive properties, ω_0 was a normalization factor to enable the use of the parameter Q with the dimension ´Farad´, and α was the CPE power with $-1 < \alpha \leq 1$ [Göh08]. For $\alpha = 1$ purely capacitive behavior was obtained. Model A1 was fitted to the measured impedance data using computer-aided complex nonlinear least squares fitting (CNLS) [Göh08].

Equivalent circuit B1 was a transition line model [Bis00]. Here, r_2 was a distributed resistance per unit length corresponding to the whole electrode area and describing the resistance of the flooded pores. The interphase, at which (capacitive or pseudocapacitve) charge may be stored, was described by dispersive capacitance as given by a constant phase element (CPE). q_2 was a constant which was related to a CPE and combined resistive and capacitive properties. The electrode impedance was given by: $Z = R_2(i\omega/\omega_L)^{-\beta/2} \coth[(i\omega/\omega_L)^{\beta/2}]$. Here $R_2 = Lr_2$ was the total resistance distributed in the pores, L was the thickness of the porous layer, ω_L was the knee frequency, and $0 < \beta < 1$. The knee frequency ω_L was defined as $\omega_L = 1/(R_2Q_2)^{1/\beta}$, whereat $Q_2 = Lq_2$ was the constant of a CPE with the impedance $Z = 1/(Q_2)(i\omega)^{-\beta}$. Model B1 did not account for bulk solution resistance. Therefore, for fitting the

impedance data to model B1, the graphically determined series resistance was subtracted from the measured impedance data. The parameters of model B1 (R_2 and ω_L) were also determined graphically.

Fits of equivalent circuits A1 and B1 to the experimental data provided sufficient results (*Figure 3.30*). This indicated the correct interpretation of the impedance measurements as both models essentially described the same physicochemical phenomena.

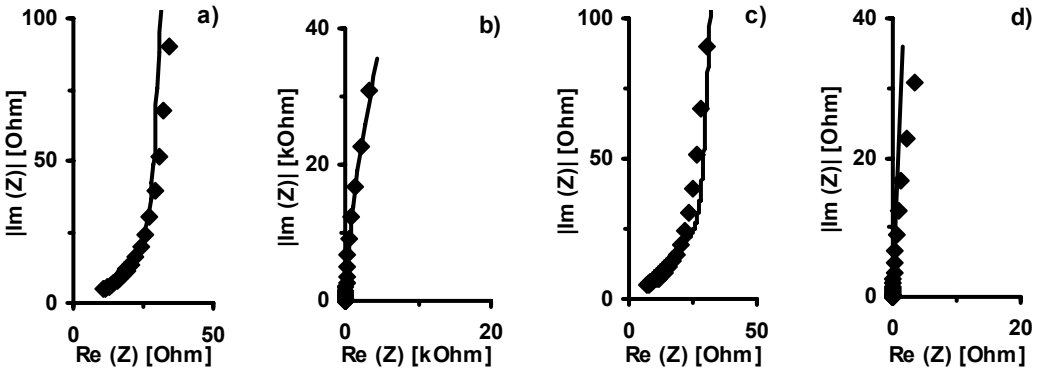

Figure 3.30. *Fits (solid lines) of equivalent circuit A1 (a) and b)) and equivalent circuit B1 (c) and d)) to measured impedance data (♦), experimental conditions indicated in Figure* ***3.27****.*

Using equivalent circuit A1, the different contributions to the capacitive impedance of the MWCNT array electrodes were analyzed in detail.

The average value of α was 0.96 for CPE1 and 0.94 for CPE2 indicating that both CPEs were essentially capacitive.

Figure 3.31 exemplifies the potential-dependence of the equivalent circuit elements of circuit A1 (*Figure 3.29 a)*). The capacitance as determined by CPE2 showed a potential-dependence reflecting the findings of the CV studies (*Figure 3.31 a)*). From

0 to 0.4 V vs. Ag/AgCl the capacitance passed through a maximum corresponding to pseudocapacitance due to surface faradic reactions. In the range from 0.4 to 0.7 V vs. Ag/AgCl the capacitance was almost constant, which was consistent with the constant current observed in the CV in this potential range. Above 0.7 V vs. Ag/AgCl the capacitance slightly increased due pseudocapacitance originating from surface faradaic reactions. The capacitance as determined by CPE1 showed the same potential-dependent characteristics as the capacitance determined by CPE2, but the potential-dependence was weaker indicating that the major part of the surface functionalities was located at the internal surface of the electrodes (*Figure 3.31 b)*).

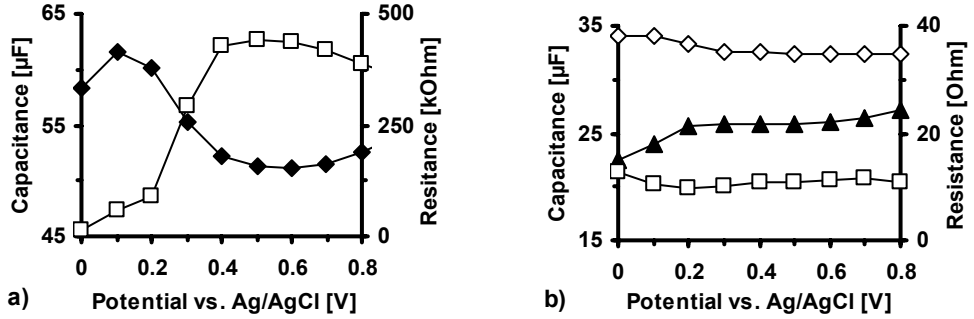

Figure 3.31. *Potential-dependence of the equivalent circuit elements of circuit A1 (Figure **3.29**): a) capacitance as determined by CPE2 (♦) and leakage resistance R3 (□), b) capacitance as determined by CPE1, internal resistance R2 (◊), and solution resistance R1 (□), MWCNT array electrode (0.096 mg/cm²), 0.1 M KCl, 0.5 V vs. Ag/AgCl.*

The leakage resistance R3 covered a range from 10 to 450 kOhm and showed a strong potential-dependence. The high values of the leakage resistance signified that the MWCNT electrodes basically behaved like a charge transfer blocking interface. The strong potential-dependence of the leakage resistance corresponded to the findings of the CV studies and indicated that pseudocapacitances were intimately related to and dependent on potential-dependent faradaic electron-transfer processes. In the potential

range from 0 to 0.4 V vs. Ag/AgCl, where pseudocapacitance due to surface faradic reactions was verified, the leakage resistance showed its lowest values. In the potential range from 0.4 to 0.6 V vs. Ag/AgCl, where the current basically originated from the formation of an ionic double-layer, the leakage resistance was almost constant and showed its extreme values indicating that the observed current essentially was of purely capacitive nature. In the potential range from 0.6 to 0.8 V vs. Ag/AgCl, where pseudocapacitance due to weak surface faradic reactions occurred, the leakage resistance slightly decreased. The bulk solution resistance R1 and the internal resistance R2 were almost potential-independent.

The capacitance as determined by CPE2 increased with the specific deposit mass of the MWCNT arrays (*Figure 3.25 b)*) confirming above explained results that the full amount of the deposited mass contributed to the capacitance of the MWCNT electrodes. The capacitance as determined by CPE1 initially increased with the specific deposit mass of the MWCNT arrays, but then reached a limiting value (*Figure 3.25 b)*). The limiting value was consistent with a constant external surface of the MWCNT electrodes. The initial increase indicated deposit thickness-dependent surface qualities which were attributed to the growth mechanism of the MWCNT arrays. Consistent with the porous nature of the electrodes, the capacitance attributed to the internal electrode surface (CPE2) clearly was the major part of the sum of the capacitances as determined by CPE1 and CPE2. This sum fairly agreed with the over-all capacitance as determined from the low-frequency impedance data and the CV experiments (*Figure 3.25 a)*). The deviations were attributed to statistical uncertainty in the fitted parameters and to the normalization of constant phase elements. The internal resistance of the electrodes R2 reasonably agreed with the graphically

determined internal resistance (*Figure 3.28*). The deviations were in turn attributed to statistical uncertainty in the fitted parameters. The solution resistance R1 and the leakage resistance R3 did not show a dependency on the specific deposit mass of the MWCNT arrays. At 0.5 V vs. Ag/AgCl, the average leakage resistance was 615 kOhm.

Electron Transfer (Faradaic) Characteristics

To study electron transfer (faradaic) characteristics of the MWCNT array electrodes, CV and EIS measurements were performed on aqueous 0.1 M KCl solutions containing 5 mM $K_4Fe(CN)_6$ as redox probe.

Figure 3.32 a) shows a typical CV of the redox reaction of the $Fe(CN)_6^{3-/4-}$ redox couple at a MWCNT electrode. The CVs were peak-shaped and the peak currents linearly increased with the square root of the sweep rate (*Figure 3.32 b)*). This corresponded rather to a macro-electrode with semi-finite linear diffusion of reactants to the electrode surface than to a nano-electrode ensemble, for which sigmoidal-shaped CVs due to spherical diffusion are typically. This was because the MWCNT electrodes had a pore size of tens of nm, which was smaller than the diffusion layer thickness (~$\sqrt{Dt}$, normally over microns). As a consequence, the diffusion layers at the individual MWCNTs overlapped and formed a diffusion layer that was linear (i.e. planar) to the geometric area of the MWCNT electrodes [Li02]. The absolute values of the anodic and the cathodic peak currents were approximately equal (*Figure 3.32 b)*). Moreover, the peak separation of the anodic and cathodic peak was large (0.2-0.5 V) and increased with increasing sweep rate (*Figure 3.32 c)*) signifying a high electrode resistance. This CV analysis indicated a quasi-reversible process likely

as a consequence of both the high charge transfer resistance at the MWCNTs (due to basal plane-like structure) and the slow diffusion through the pores [Li02].

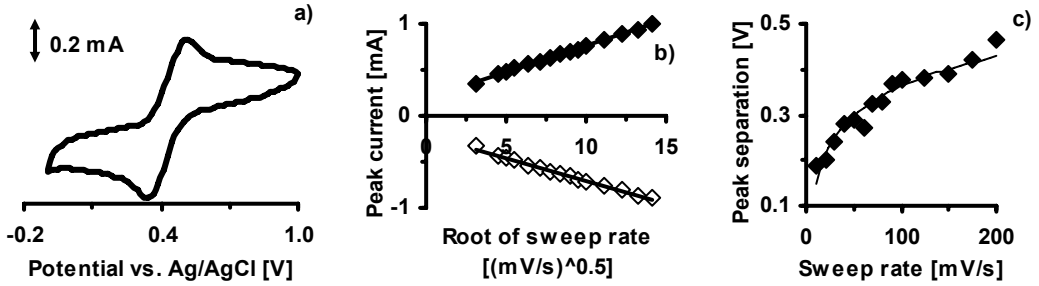

Figure 3.32. *CV studies of a MWCNT electrode (0.096 mg/cm²) in 0.1 M KCl containing 5 mM $K_4Fe(CN)_6$: a) peak-shaped CV (100 mV/s, half-wave potential: 0.45 V vs. Ag/AgCl, counter electrode: Pt-foil), b) anodic and cathodic peak currents in dependence on the square root of the sweep rate, c) separation of the anodic and cathodic peak in dependence on the sweep rate.*

Figure 3.33 a) shows the dependences of the peak currents and the peak separation on the specific deposit mass. The peak currents increased with the specific deposit mass as the active surface area increased with the specific deposit mass (*Figure 3.26*). The peak separation decreased with increasing specific deposit mass as the internal resistance (*Figure 3.33 b)*) and the charge transfer resistance (see below) of the electrodes decreased with the specific deposit mass.

Figure 3.34 exemplifies the frequency depended impedance of the redox reaction of the $Fe(CN)_6^{3-/4-}$ redox couple at the MWCNT electrodes. The impedance of the MWCNT electrodes showed the typical characteristics of an interfacial reaction in a pore surface [Bis00].

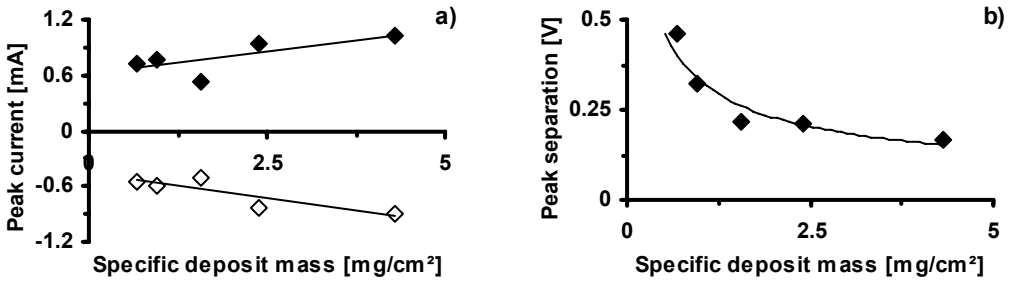

Figure 3.33. *Specific deposit mass-dependent a) peak current and b) peak separation of MWCNT array electrodes, CV studies, 5 mM $K_4Fe(CN)_6$ in 0.1 M KCl.*

In the high-frequency region (*Figure 3.34 a)*), the system with faradaic reaction showed the same behavior as the system without (*Figure 3.27 a)*). The impedance gave a straight line with a slope of about 45°, which was associated with the distributed resistance/capacitance (RC) network of the porous electrodes.

In the mid-frequency range (*Figure 3.34 b)*), the electron transfer resistance caused a depressed arc. This depressed arc was the manifestation of the interfacial reaction in the pore surface.

At lower frequencies (*Figure 3.34 c)*), the impedance gave a straight line with a slope of 45°, which is characteristic (at such frequencies) of mass transport limitation of a charge transfer process by linear diffusion in the solution interior (that is, between electrode surface and solution interior).

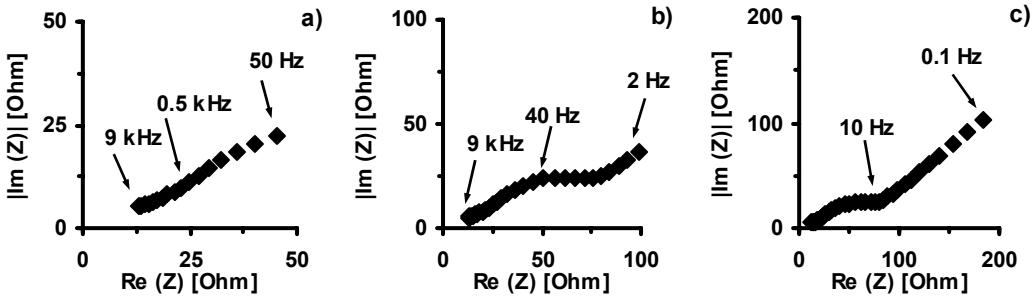

Figure 3.34. *a) High-, b) mid-, and c) low-frequency impedance of 5 mM $K_4Fe(CN)_6$ at a MWCNT electrode (0.096 mg/cm², 0.1 M KCl, 0.45 V vs. Ag/AgCl (half-wave potential), 10 mV amplitude sinusoidal wave, counter electrode: Pt-foil).*

Based on the analyses of the CV and EIS measurements and assuming that the electrochemical reaction took place only in the pore surface (This assumption was justified as the active surface area was a multiple of the geometric surface area (*Figure 3.26*)), the impedance spectra were analyzed with the equivalent circuits A2 and B2 shown in *Figure 3.35*.

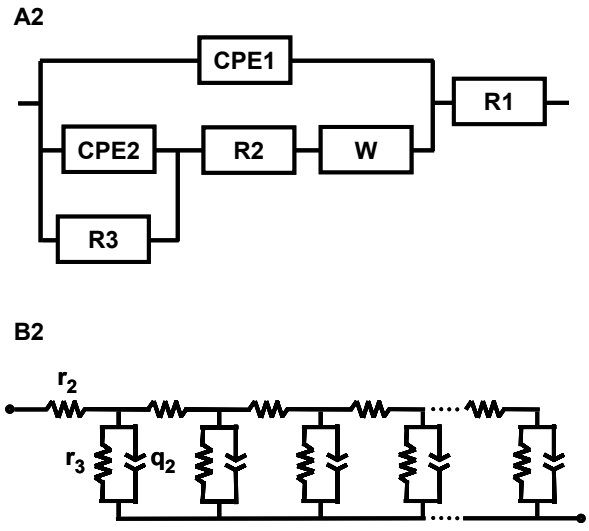

Figure 3.35. *Equivalent circuits used to model the faradaic impedance response of MWCNT array electrodes: ladder extended by a Warburg element (A2) and transition line model (B2) (circuit elements as explained in the main text).*

Equivalent circuit A2 was an extension of equivalent circuit A1 (*Figure 3.29*). In equivalent circuit A2, the elements R1, CPE1, R2, and CPE2 had the same meaning as in equivalent circuit A1. R3 was a faradaic electron transfer resistance associated with the interfacial reaction in the pore surface. W was the Warburg diffusional element representing the mass transport limitations due to linear diffusion in the electrolytic solution. The Warburg impedance was given by $Z_W = W/(\sqrt{(i\,\omega)})$, where $i = \sqrt{(-1)}$ and W was the Warburg parameter, which is proportional to the reciprocal of the electrode surface [Göh09]. Model A2 was fitted to measured impedance data using computer-aided complex nonlinear least squares fitting (CNLS) [Göh08].

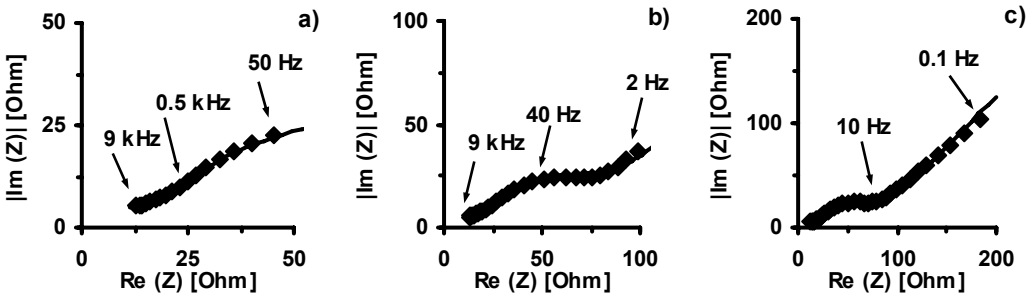

Figure 3.36. *Fit of equivalent circuit A2 (solid lines) to the faradaic impedance response of a MWCNT array electrode (♦), a) high-, b) mid-, and c) low-frequency impedance (experimental conditions indicated in Figure 3.34).*

In transition line model B2 [Bis00], the effect of an interfacial reaction in the pore surface was modeled by adding a parallel charge transfer resistance length r_3 to the interfacial impedance of model B1 (*Figure 3.29*). The electrode impedance then admited the form: $Z = [R_2R_3/(1 + i\omega/\omega_3)^{\beta}]^{1/2} \coth[(\omega_3/\omega_L)^{\beta/2} (1 + i\omega/\omega_3)^{\beta}]^{1/2}$. Here $R_3 = r_3/L$ was the total wall resistance, and $\omega_3 = 1/(R_3Q_2)^{1/\beta}$ is the characteristic frequency of the interfacial process. The quotient $\omega_3/\omega_L = (R_2/R_3)^{1/\beta}$ determined the

shape of the impedance spectra. For $\omega_L > \omega_3$ (or $R_3 > R_2$) a line at high frequency and a low frequency arc were obtained. Model B2 did not account for bulk solution resistance and mass transport limitations due to diffusion. Therefore, for fitting impedance data to model B2, the graphically determined series resistance was subtracted from the measured impedance data and the low frequency data corresponding to the mass transport limitation due to diffusion was not considered. The parameters of model B2 (R_2, R_3 and ω_L) were estimated.

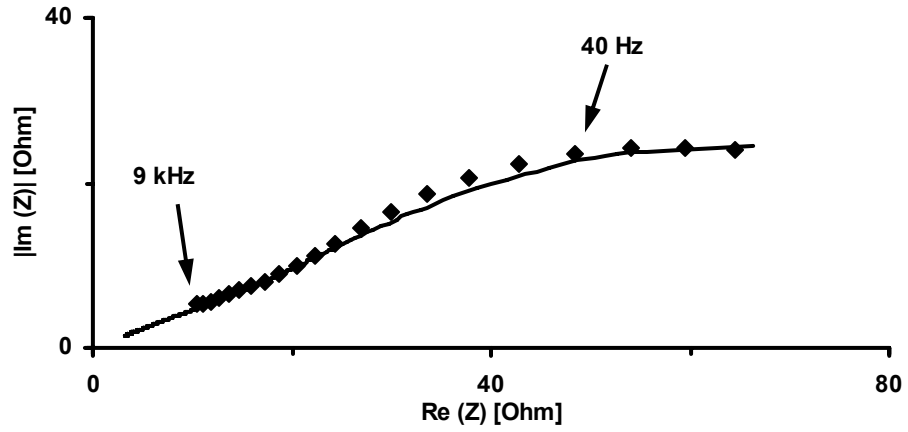

Figure 3.37. *Fit of equivalent circuit B2 (solid line) to the faradaic impedance response of a MWCNT array electrode (♦) (experimental conditions indicated in Figure 3.34).*

Fits of equivalent circuits A2 and B2 to the experimental data provided sufficient results (*Figure 3.36* and *Figure 3.37*). This indicated the correct interpretation of the impedance measurements as both models essentially describe the same physicochemical phenomena.

Using equivalent circuit A2, the contributions to the faradaic impedance of the MWCNT array electrodes were analyzed in detail.

The average value of α was 0.82 for CPE1 and 0.91 for CPE2 signifying that the CPEs were essentially capacitive. R1, CPE1, R2, and CPE2 showed the same dependency on the specific deposit mass of the MWCNT arrays as discussed above.

The Warburg parameter decreased with increasing specific mass (*Figure 3.38 a)*) and consequently with the active surface area of the MWCNT arrays as the Warburg parameter was proportional to the reciprocal of the active electrode surface.

The faradaic charge transfer resistance R3 decreased with the specific deposit mass of the MWCNT arrays (*Figure 3.38 b)*) as the number of surface defect sites and surface functional groups, which were responsible for much of the electrocatalytic activity of the MWCNTs [Tra08], increased with the specific deposit mass of the MWCNT arrays. The decrease of the electron transfer resistance and the internal resistance with increasing specific deposit mass of the MWCNT arrays explained the decrease of the peak separation with increasing specific deposit mass of the MWCNT arrays observed in the CV studies (*Figure 3.32*).

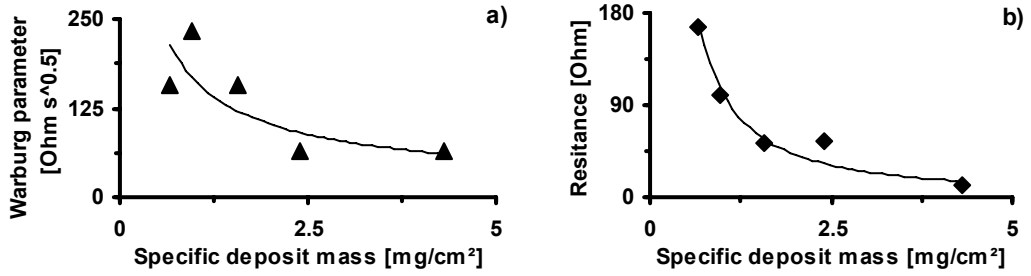

Figure 3.38. *a) Warburg parameter and b) electron transfer resistance R3 (as determined by equivalent circuit A2 (Figure 3.35)) of the redox reaction of the $Fe(CN)_6^{3-/4-}$ redox couple at MWCNT array electrodes in dependence on the specific deposit mass of the MWCNT arrays (5 mM $K_4Fe(CN)_6$ in 0.1 M KCl, 0.45 V vs. Ag/AgCl (half-wave potential)).*

3.2.3. Application of Well-aligned MWCNT Array Electrodes

Non-enzymatic glucose detection at the MWCNT array electrodes was studied by cyclic voltammetry and amperometry.

Figure 3.39 a) shows CVs of the electrocatalytic glucose oxidation at a MWCNT array electrode in 0.1 M NaOH and increasing glucose concentration (0-5 mM). The glucose oxidation occured at a remarkably negative potential of about -0.6 V vs. Ag/AgCl. The negative oxidation potential indicated a strong electrocatalytic activity of the MWCNT array electrodes regarding direct glucose oxidation.

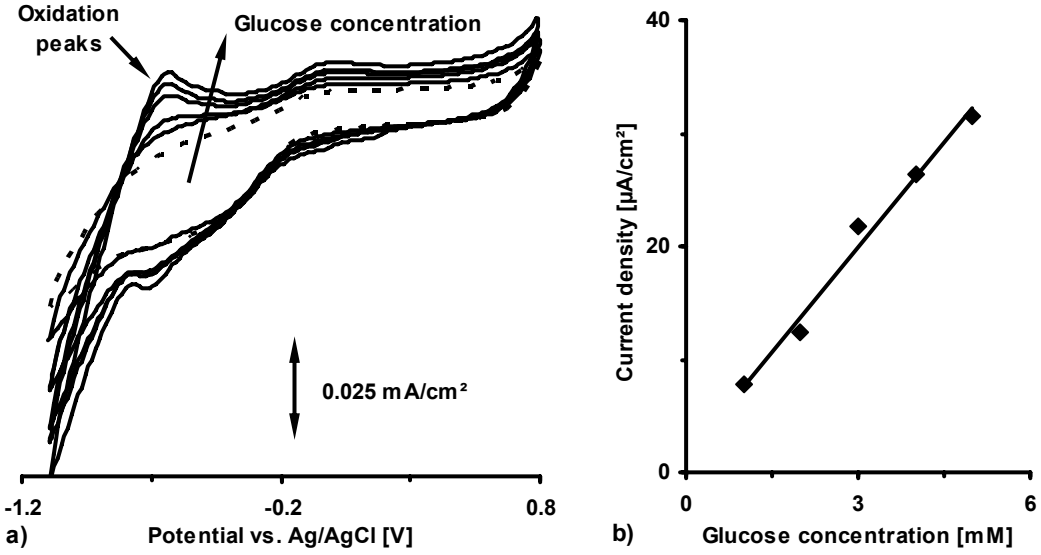

Figure 3.39. *a) CVs of the electrocatalytic glucose oxidation at a MWCNT electrode (glucose concentration: 0-5 mM, dotted line: background (0 mM glucose), 0.1 M NaOH, sweep rate: 100 mV/s, counter electrode: Pt-foil), b) dependence of the baseline corrected glucose oxidation peak (-0.6 V vs. Ag/AgCl) on the glucose concentration. The current density was estimated using the active surface area of the array electrodes (see chapter 3.2.2.).*

The baseline corrected oxidation peak current density of the CVs linearly increased with the glucose concentration within the physiological range of interest (*Figure 3.39 b)*), which ranges from about 3 mM to 8 mM glucose [Pec06].

Figure 3.40 a) shows the amperometric response of a MWCNT array electrode in 0.1 M NaOH to the successive addition of 0.8 mM glucose. In agreement with the voltammetric studies (*Figure 3.40 b)*), the amperometric current density linearly increased with glucose concentration. The array electrodes showed a good sensitivity of 12 µA/mM/cm². In addition, the array electrodes rapidly responded to the changes in glucose concentration.

All in all, well-aligned MWCNT array electrodes provide a promising opportunity to innovative non-enzymatic glucose sensors.

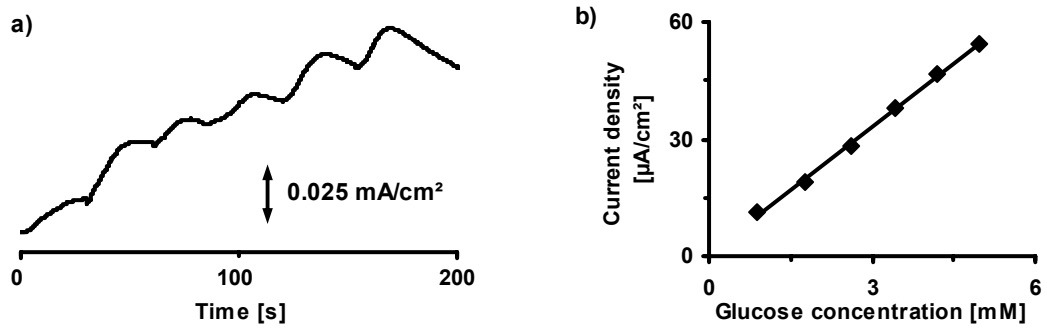

Figure 3.40. *Amperometric response of a MWCNT array electrode in 0.1 M NaOH to the successive addition of 0.8 mM glucose: a) current-time response, and b) dependence of the current density at the MWCNT electrode in dependence on the glucose concentration (two electrode circuit: counter/reference electrode: Au-foil, potential 0.1 V vs. Au).*

4. Summary

In this work, preparations, characteristics, and applications of dimeric fullerene oxides and well-aligned MWCNT arrays – both being carbon-based nanostructured materials – were developed. The main research results achieved in this work are summarized below.

4.1. Dimeric Fullerene Oxides

In this chapter, the preparations, physicochemical characteristics, and applications of dimeric fullerene oxides developed in this work are summed up.

Preparation of Dimeric Fullerene Oxides

Directed and specific syntheses and separations of preparative amounts of various dimeric fullerene oxides using conventional laboratory methods were developed:

- $C_{140}O$ was synthesized by solid-state thermolysis of C_{70}/C_{70}-oxide mixed powders and isolated from the resulting product mixtures nearly quantitatively (97 % purity) by precipitation.
- $C_{130}O$ was synthesized in yields of 20 % by solid-state thermolysis of a fullerene/ mixed powder containing C_{60}, C_{70}, C_{60}-, and C_{70}-oxide.

- Highly pure, soluble mono-, bis-, and tris-adducts of $C_{120}O$ were synthesized by a diazoalkane addition and a Bingel cyclopropanation reaction and separated from the resulting product mixture using preparative flash chromatography.
- Regio-controlled mono- and bis-functionalized dimeric fullerene oxides were synthesized by solid-state thermolysis of mixtures containing a functionalized epoxy-fullerene and a reactant fullerene.

The preparations developed in this work contribute to the utilization of dimeric fullerene oxides as precursors for further fullerene based materials, as materials in fullerene polymer science and organic electronics, and as model systems for investigation intramolecular charge transfer and interaction between electron spins in molecules.

Physicochemical Characteristics of Dimeric Fullerene Oxides

A series of dimeric fullerenes was comprehensively characterized for the first time. Oxidative and thermal properties, electronic absorption properties, and the electron acceptor strength of the dimeric fullerene oxides $C_{120}O$, $C_{130}O$, and $C_{140}O$, and the $C_{120}O$ mono-adducts **1** ($C_{120}OR'$) and **2** ($C_{120}OR''$) were determined and compared with C_{60}, C_{70}, equimolar C_{60}/C_{70} mixtures, $C_{60}R'$, and $C_{60}R''$.

- The oxidative and the thermal stability of the dimers were lower than those of monomeric comparison substances.
- Throughout the visible region, the C_{60} dimers $C_{120}O$, **1**, and **2** showed an enhanced absorption, which indicated the interaction of transition dipole

moments of the two fullerene-cages of the dimers. $C_{140}O$ showed a smaller HOMO-LUMO gap compared to C_{70}.

- The $C_{120}O$ derivatives **1** and **2** were less prone to reduction compared to $C_{120}O$.

The identified characteristics contribute to the elucidation of the structure-properties relationships of fullerenes.

Application of Dimeric Fullerene Oxides

The applicability of well-soluble, oligomeric fullerenes to organic electronics was verified by applying the $C_{120}O$ mono-adducts **1** ($C_{120}OR'$) and **2** ($C_{120}OR''$) as electron acceptor in BHJ solar cells and by proving intermolecular electron transfer for photoactive blends containing **1** as electron acceptor.

The dimeric fullerene oxides **1** and **2** enable studying the impact of longish fullerene oligomers on the performance of organic electronics such as organic photovoltaics, photodiodes, photodetectors, and field-effect transistors. In particular **1** enables a direct comparison with the most frequently used [60]PCBM ($C_{60}R'$).

4.2. Well-aligned MWCNT Arrays

In this chapter, the preparation, electrochemical characteristics, and application of well-aligned MWCNT array electrodes developed in this work are summarized.

Preparation of MWCNT arrays

Well-aligned MWCNT arrays were directly grown on silica substrates by thermal chemical vapor deposition and electrochemically purified by cyclic voltammetry. Electrochemically induced purification of as-grown MWCNT arrays represented a mild and on-line controllable method of purification in one exclusive step and is therefore an attractive option to commonly used wet and gas phase purification, in particular for electrochemical applications of MWCNT arrays.

The deposit thickness of the MWCNT arrays linearly depended on the deposit mass. Therefore, difference weighting was an easy way to estimate the deposit thickness of the MWCNT arrays.

Electrochemical Characteristics of MWCNT Array Electrodes

Capacitive and electron transfer characteristics of well-aligned MWCNT electrodes were determined using cyclic voltammetry and electrochemical impedance spectroscopy:

- Capacitance and active surface area of the MWCNT electrodes systematically increased with the specific deposit mass and accordingly with the deposit

thickness of the MWCNT arrays. The active surface area of the MWCNT electrodes was a multiple of the geometric area of the MWCNT arrays. This indicated that the full amount of the deposit mass of the arrays contributed to their capacitance.

- The capacitance of the MWCNT electrodes was composed of a capacitance originating from the internal and a capacitance originating from the external electrode surface. The capacitance originating from the internal electrode surface clearly was the major part of the over-all capacitance.
- The capacitance of the MWCNT electrodes further consisted of a capacitance due to the formation of an ionic double-layer at the electrode/electrolytic solution interface and pseudocapacitances due to surface faradic reactions of redox active surface functionalities.
- The effective internal resistance of the porous MWCNT electrodes decreased with increasing specific deposit mass and consequently with increasing deposit thickness of the MWCNT arrays, indicating a deposit thickness-dependent morphology.
- The MWCNT array electrodes were macro-electrode with semi-finite linear diffusion of reactants to the electrode surface.
- The electron transfer resistance of the MWCNT electrodes decreased with increasing specific deposit mass as the number of surface defect sites and surface functional groups, which were responsible for much of the electro-catalytic activity of the MWCNTs, also increased with the specific deposit mass of the MWCNT arrays.

All in all, the MWCNT array electrodes showed the typical characteristics of porous capacitor macro-electrodes with an electrocatalytically active surface.

The identified characteristics elucidate the structure-properties relationship of CNT array electrodes.

Application of MWCNT Arrays Electrodes

Well-aligned MWCNT array electrodes were applied to non-enzymatic glucose detection. MWCNT array electrodes showed a strong electrocatalytic activity and a high sensitivity regarding direct glucose oxidation. MWCNT array electrodes provide a promising opportunity to innovative non-enzymatic glucose sensors.

5. References

[Bac01] S.M. Bachilo, A.F. Benedetto, R.B. Weisman, *Triplet State Dissociation of C_{120}, the Dimer of C_{60}*, The Journal of Physical Chemistry B, 105 (2001) 9845-9850.

[Bal04] K. Balasubramanian, M. Burghard, K. Kern, *Carbon Nanotubes: Electrochemical Modification*, Dekker Encyclopedia of Nanoscience and Nanotechnology, Volume 1, J.A. Schwarz, C.I. Contescu, K. Putyera (Eds.), New York, Basel: Marcel Dekker, Inc., 2004.

[Bal06] K. Balasubramanian, M. Burghard, *Biosensors Based on Carbon Nanotubes*, Fresenius' Journal of Analytical Chemistry, 385 (2006) 452-468.

[Bal96] A.L. Balch, D.A. Costa, W.R. Fawcett, K. Winkler, *Electronic Communication in Fullerene Dimers: Electrochemical and Electron Paramagnetic Resonance Study of the Reduction of $C_{120}O$*, Journal of Physical Chemistry 100 (1996) 4823-4827.

[Bar00] J.N. Barisci, G.G. Wallace, R.H. Baughman, *Electrochemical Characterization of Single-Walled Carbon Nanotube Electrodes*, Journal of the Electrochemical Society 147 (2000) 4580-4583.

[Bar03] J.N. Barisci, G.G. Wallace, D. Chattopadhyay, F. Papadimitrakopoulos, R.H. Baughman, *Electrochemical Properties of Single-Wall Carbon*

Nanotube Electrodes, Journal of the Electrochemical Society, 150 (2003) E409.

[Bar05] E. Barsoukov, J.R. Macdonald, *Impedance Spectroscopy – Theory, Experiment, and Applications*, Weinheim: Wiley-VCH, 2005.

[Bec95] R.D. Beck, G. Bräuchle, C. Stoermer, M.M. Kappes, *Formation of C_{119} by Tthermal Decomposition of $C_{60}O$*, Journal of Chemical Physics, 102 (1995) 540-543.

[Bin93] C. Bingel, *Cyclopropylation of Fullerenes*, Chemische Berichte, 126 (1993) 1957.

[Bis00] J. Bisquert, G. Garcia-Belmonte, F. Fabregat-Santiago, N.S. Ferriols, P. Bogdanoff and E.C. Pereira, *Doubling Exponent Models for the Analysis of Porous Film Electrodes by Impedance. Relaxation of TiO_2 Nanoporous in Aqueous Solution*, Journal of Physical Chemistry B, 104 (2000) 2287-2298.

[Bon03] D.A. Bonnell, *Materials in Nanotechnology: New Structures, New Properties, New Complexity*, Journal of Vacuum Science and Technology A, 21 (2003) 194-206.

[Bra09] L. Brand, M. Gierlings, A. Hoffknecht, V. Wagner, A. Zweck, *Kohlenstoff-Nanoröhren – Technologieanalyse*, Düsseldorf: Zukünftige Technologien Consulting der VDI Technologiezentrum GmbH, 2009.

[Bri05] D.A. Britz, A.N. Khlobystov, K. Porfyrakis, A. Ardavan, G.A.D. Briggs, *Chemical Reactions Inside Single-walled Carbon Nano Test-tubes*, Chemical Communications, 1 (2005) 37-39.

[Che01] J.H. Chen, Z.P. Huang, D.Z. Wang, S.X. Yang, J.G. Wen, Z.F. Ren, *Electrochemical Synthesis of Polypyrrole-Carbon Nanotube Nanoscale Composites Using Well-aligned Carbon Nanotube Arrays*, Applied Physics A, Materials Science & Processing, 73 (2001) 129-132.

[Che02] J.H. Chen, W.Z. Li, D.Z. Wang, S.X. Yang, J.G. Wen, Z.F. Ren, *Electrochemical Characterization of Carbon Nananotubes as Electrode in Electrochemical Double-layer Capacitors*, Carbon, 40 (2002) 1193-1198.

[Che04] Q.L. Chen, K.H. Xue, W. Shen, F.F. Tao, S.Y. Yin, W. Xu, *Fabrication and Electrochemical Properties of Carbon Nanotube Array Electrode for Supercapacitors*, Electrochimica Acta, 49 (2004) 4157-4161.

[Cho08] C.-L. Choong, W.I. Milne, K.B.K. Teo, *Review: Carbon Nanotube for Microfluidic Lab-on-a-chip Application*, International Journal of Material Forming, 1 (2008) 117-125.

[Con06] M.J. O'Connell (Ed.), *Carbon Nanotubes: Properties and Applications*, Boca Raton: CRC Press, 2006.

[Cui06] H.-F. Cui, J.-S. Ye, X. Liu, W.-D. Zhang, F.-S. Sheu, *Pt–Pb Alloy Nanoparticle/Carbon Nanotube Nananocomposite: A Strong Electrocatalyst for Glucose Oxidation*, Nanotechnology, 17 (2006) 2334-2339.

[Cui07] H.-F. Cui, J.-S. Ye, W.D. Zhang, C.-M. Li, J.H.T. Luong, F.-S. Sheu, *Selective and Sensitive Electrochemical Detection of Glucose in Neutral*

Solution Using Platinum-lead Alloy Nanoparticle/Carbon Nanotube Nanocomposites, Analytica Chimica Acta, 594 (2007) 175-183.

[Den95] J.-P. Deng, C.-Y. Mou, C.-C. Han, *Electrospray and Laser Desorption Ionization Studies of $C_{60}O$ and Isomers of $C_{60}O_2$,* Journal of Physical Chemistry, 99 (1995) 14907-14910.

[Den96] J.-P. Deng, C.-Y. Mou, C.-C. Han, *$C_{180}O_2$, a V-shaped Fullerene Trimer*, Chemical Physics Letters, 256 (1996) 96-100.

[Dra00A] N. Dragoe, H. Shimotani, M. Hayashi, K. Saigo, A. de Bettencourt-Dias, A.L. Balch, Y. Miyake, Y.Achiba, K. Kitazawa, *Electronic Interactions in a New Fullerene Dimer: $C_{122}H_4$, with Two Methylene Bridges*, Journal of Organic Chemistry, 65 (2000) 3269-3273.

[Dra00B] N. Dragoe, K. Nakahara, H. Shimotani, L. Xiao, S. Tanibayashi, T. Higuchi, K. Kitazawa, *All-carbon [60]fullerene Oligomers of Pearl-necklace Type*, Fullerene Science and Technology, 8 (2000) 545-559.

[Dre01] M.S. Dresselhaus, G. Dresselhaus, P. Avouris, *Carbon nanotubes: Synthesis, Structure, Properties, and Applications*, Berlin (et al.): Springer, 2001.

[Dun03] L. Dunsch, P. Rapta, A. Gromov, A. Stasko, *In situ ESR/UV-vis-NIR Spectroelectrochemistry of C_{60} and Its Dimers C_{120}, $C_{120}O$ and $C_{120}OS$*, Journal of Electroanalytical Chemistry, 547 (2003) 35-43.

[Eis98A] H.-J. Eisler, F.H. Hennrich, E.Werner, A. Hertwig, C. Stoermer, M.M. Kappes, *Superdiatomics and Picosprings: Cage-Cage Vibrations*

in $C_{120}O$, $C_{120}O_2$, and in Three Isomers of $C_{130}O$, Journal of Physical Chemistry A, 102 (1998) 3889-3897.

[Eis98B] H.-J. Eisler, F.H. Hennrich, M.M. Kappes, *C_{120} and $C_{120}O$: Vibrational Spectroscopy and PM3 Calculations*, Electronic Properties of Novel Materials – Progress in Molecular Nanostructures, AIP Conference Proceedings, 442 (1998) 215-218.

[Ekl00] P. Eklund, A. Rao (Eds.), *Fullerene Polymers and Fullerene Polymer Composites*, Berlin (et al.): Springer, 2000.

[Elv93] S.W. McElvany, J.H. Callahan, M.M. Ross, L.D. Lamb, D.R. Huffman, *Large Odd-Numbered Carbon Clusters from Fullerene-Ozone Reactions*, Science, 260 (1993) 1632-1634.

[Fan04] H.-T. Fang, C.-G. Liu, C. Liu, F. Li, M. Liu, H.-M. Cheng, *Purification of Single-Wall Carbon Nanotubes by Electrochemical Oxidation*, Chemistry of Materials, 16 (2004) 5744-5750.

[For02] G.S. Forman, N. Tagmatarchis, H. Shinohara, *Novel Solid State Synthesis and Characterization of $(C_{70})_2$ Dimers*, Journal of the American Chemical Society, 124 (2002) 178-179.

[Fow07] P.W. Fowler, D.E. Manolopoulos, *An Atlas of Fullerenes*, New York: Dover Publications, 2007.

[Fow97] P.W. Fowler, D. Mitchell, R. Taylor, G. Seifert, *Structures and Energetics of Dimeric Fullerene and Fullerene Oxide Derivatives*, Journal of the Chemical Society, Perkin Transactions 2, 10 (1997) 1901-1905.

[Fra04] E. Frackowiak, *Carbon Nanotubes for Storage of Energy: Super Capacitors*, Dekker Encyclopedia of Nanoscience and Nanotechnology, Volume 1, J.A. Schwarz, C.I. Contescu, K. Putyera (Eds.), New York, Basel: Marcel Dekker, Inc., 2004.

[Fuj01A] K. Fujiwara, K. Komatsu, G.-W. Wang, T. Tanaka, K. Hirata, K. Yamamoto, M. Saunders, *Derivatization of Fullerene Dimer C_{120} by the Bingel Reaction and a ^{3}He NMR Study of ^{3}He@C_{120} Monoadducts*, Journal of the American Chemical Society, 123 (2001) 10715-10720.

[Fuj01B] K. Fujiwara, K. Komatsu, *First Synthesis of a Highly Symmetrical Decakis-adduct of Fullerene Dimer C_{120},* Chemical Communications, 19 (2001) 1986-1987.

[Fuj01C] M. Fujitsuka, H. Takahashi, T, Kudo, K. Tohji, A. Kasuya, O. Ito, *Photophysical and Photochemical Properties of $C_{120}O$, a C_{60} Dimer Linked by a Saturated Furan Ring*, Journal of Physical Chemistry A, 105 (2001) 675-680.

[Fuj02A] K. Fujiwara, K. Komatsu, *Mechanochemical Synthesis of a Novel C_{60} Dimer Connected by a Silicon Bridge and a Single Bond*, Organic Letters, 4 (2002) 1039-1041.

[Fuj02B] M. Fujitsuka, K. Fujiwara, Y. Murata, O. Ito, and K. Komatsu, *Photophysical and Photochemical Properties of Decakis-Adduct of C_{120} and Related Compounds*, Chemistry Letters, 5 (2002) 512-513.

[Gal92] P.K. Gallagher, Z. Zhong, *Some Applications of Thermal Analysis to Fullerenes*, Journal of Thermal Analysis, 38 (1992) 2247-2255.

[Gao00] M. Gao, S. Huang, L. Dai, G. Wallace, R. Gao, Z. Wang, *Aligned Coaxial Nanowires of Carbon Nanotubes Sheathed with Conducting Polymers*, Angewandte Chemie, 112 (2000) 3810-3812.

[Gar03] O.G. Garkusha, S.P. Solodovnikov, B.V. Loksh, *Thermal Degradation of the Polymer Obtained by Oxidation of C_{60} Fullerene by Oleum*, Russian Chemical Bulletin, 52 (2003) 1688-1692.

[Gie99] S. Giesa, J.H. Gross, R. Gleiter, A. Gromov, W. Krätschmer, W.E. Hull, S. Lebedkin, *$C_{120}OS$: The First Sulfur-containing Dimeric [60]Fullerene Derivative*, Chemical Communications, 5 (1999) 465-466.

[Göh08] H. Göhr, *Zahner IM6 user manual*, www.zahner.de, (2008) (lastly verified January 2009).

[Gon05] K. Gong, Y. Yan, M. Zhang, L. Su, S. Xiong, L. Mao, *Electrochemistry and Electroanalytical Applications of Carbon Nanotubes: A Review*, Analytical Sciences, 21 (2005) 1383-1394.

[Gro96] A. Gromov, S. Ballenweg, W. Krätschmer, S. Lebedkin, *Production and Thermal Decomposition of $C_{120}O$*, Fullerenes and Fullerene Nanostructures: Proceedings of the International Winterschool on Electronic Properties of Novel Materials Kirchberg, Austria, H. Kuzmany, J. Fink, M. Mehring, S. Roth (Eds.), Singapore: World Scientific: 1996, 460-463.

[Gro97A] A. Gromov, S. Lebedkin, S. Ballenweg, A.G. Avent, R. Taylor, W. Krätschmer, *$C_{120}O_2$: The First [60]Fullerene Dimer with Cages Bis-*

linked by Furanoid Bridges, Chemical Communications, 2 (1997) 209-210.

[Gro97B] A. Gromov, S. Ballenweg, S. Giesa, S. Lebedkin, W.E. Hull, W. Krätschmer, *Preparation and Characterisation of C_{119}*, Chemical Physics Letters, 267 (1997) 460-466.

[Gro97C] A. Gromov, S. Ballenweg, W. Krätschmer, S. Giesa, S. Lebedkin, *The C_{60}-$C_{60}O$ system: A Source of New Fullerene Derivatives*, Molecular Nonostructures: Proceedings of the International Winterschool on Electronic Properties of Novel Materials Kirchberg, Austria, H. Kuzmany, S. Roth (Eds.), Singapore: World Scientific: 1997, 96-100.

[Gro98] A. Gromov, S. Lebedkin, W.E. Hull, W. Krätschmer, *Isomers of the Dimeric Fullerene $C_{120}O_2$*, Journal of Physical Chemistry A, 102 (1998) 4997-5005.

[Har09] P.J.F. Harris, *Carbon Nanotube Science: Synthesis, Properties and Applications*, Cambridge (et al.): Cambridge University Press, 2009.

[Has97] K. Hasharoni, C. Bellavia-Lund, M. Keshavarz, G. Srdanov, F. Wudl, *Light-Induced ESR Studies of the Heterofullerene Dimers*, Journal of the American Chemical Society, 119 (1997) 11128-11129.

[Hey06] D. Heymann, R.B. Weisman, *Fullerene Oxides and Ozonides*, Comptes Rendus Chimie, 9 (2006) 1107-1116.

[Hey99] D. Heymann, R. Fokkens, N.M.M. Nibbering, *Stability of $C_{70}O$ in Toluene*, Fullerene Science and Technology, 7 (1999) 927-934.

[Hie08] C. Hierold, O. Brand, G.K. Fedder, J.G. Korvink, *Carbon Nanotube Devices: Properties, Modeling, Integration and Applications*, Weinheim: Wiley-VCH, 2008.

[Hir05] A. Hirsch, M. Brettreich, *Fullerenes – Chemistry and Reactions*, Weinheim: Wiley-VCH, 2005.

[Hon07A] Y. Honda, M. Takeshige, H. Shiozaki, T. Kitamura, M. Shkawa, *Excellent Frequency Response of Vertically Aligned MWCNT Electrode for EDLC*, Electrochemistry, 75 (2007) 586-588.

[Hon07B] Y. Honda, T. Haramoto, M. Takeshige, H. Shiozaki, T. Kitamura, M. Ishikawa, *Aligned MWCNT Sheet Electrodes Prepared by Transfer Methodology Providing High-power Capacitor Performance*, Electrochemical and Solid State Letters, 10 (2007) A106-A110.

[Hop04] H. Hoppe, N.S. Sariciftci, *Organic Solar Cells: An Overview*, Journal of Materials Research, 19 (2004) 1924-1945.

[Hop06] Harald Hoppe, Niyazi Serdar Sariciftci, *Morphology of Polymer/Fullerene Bulk Heterojunction Solar Cells*, Journal of Materials Chemistry, 16 (2006) 45-61.

[Hou08] P.-X. Hou, C. Liu and H.-M. Cheng, *Purification of Carbon Nanotubes*, Carbon, 46 (2008) 2003-2025.

[Hum04] J.C. Hummelen, *Website of the Dutch Polymer Solar energy Initiative*, http://solar.fmns.rug.nl/, 2004 (lastly verified February 2009).

[Hum95] J.C. Hummelen, B.W. Knight, F. LePeq, F. Wudl, *Preparation and Characterization of Fulleroid and Methanofullerene Derivatives*, Journal of Organic Chemistry, 60 (1995) 532-538.

[Ibr05] M. Al-Ibrahim, H.-K. Roth, U. Zhokhavets, G. Gobsch, S. Sensfuss, *Flexible Large Area Polymer Solar Cells Based on Poly(3-hexylthiophene)/Fullerene*, Solar Energy Materials & Solar Cells, 85 (2005) 13-20.

[Jaf99] M.S. Al-Jafaria, M.P. Barrowa, R. Taylorb, T. Drewello, *Laser-induced Gas-phase Synthesis of Dimeric C_{70} Oxides*, International Journal of Mass Spectrometry, 184 (1999) L1-L4.

[Jor08] A. Jorio, G. Dresselhaus, M.S. Dresselhaus (Eds.), C*arbon Nanotubes: Advanced Topics in the Synthesis, Structure, Properties and Applications*, Berlin (et a.): Springer, 2008.

[Kad00] K.M. Kadish, R.S. Ruoff (Eds.), *Fullerenes – Chemistry, Physics, and Technology*, New York (et al.): John Wiley & Sons, Inc., 2000.

[Kan07] X. Kang, Z. Mai, X. Zou, P. Cai, J. Mo, *A Sensitive Nonenzymatic Glucose Sensor in Alkaline Media with a Copper Nanocluster/Multiwall Carbon Nanotube-modified Glassy Carbon Electrode*, Analytical Biochemistry, 363 (2007) 143-150.

[Kap08] S. Kappel, *Herstellung und Erprobung von Katalysatoren für ausgerichtete Carbon-Nanotubes*, Technische Universität Ilmenau, Department of Chemistry, Diploma Thesis: 2008.

[Kaw97] S.-I. Kawabe, T. Kawai, R.-I. Sugimoto, E. Yagasaki, K. Yoshino, *Electrochemical Properties of Fullerene Derivative Polymers as Electrode Materials*, Japanese Journal of Applied Physics, 36 (1997) 1055.

[Khl05] A.N. Khlobystov, D.A. Britz, G.A.D. Briggs, *Molecules in Carbon Nanotubes*, Accounts of Chemical Research, 38 (2005) 901-910.

[Kie06] T. Kietzke, D. Egbe, H.-H. Hörhold, D. Neher, *Comparative Study of M3EH-PPV-Based Bilayer Photovoltaic Devices*, Macromolecules, 39 (2006) 4018-4022.

[Kim06] J.H. Kim, K.-W. Nam, S.B. Ma, K.B. Kim, *Fabrication and Electrochemical Properties of Carbon Nanotube Film Electrodes*, Carbon, 44 (2006) 1963-1968.

[Kno00] J. Knol, J.C. Hummelen, *Photodimerization of a m-Phenylenebis(arylmethanofullerene): The First Rigorous Proof for Photochemical Inter-Fullerene [2 + 2] Cycloaddition*, Journal of the American Chemical Society, 122 (2000) 3226-3227.

[Koe04] J. Koehne, J. Li, A.M. Cassell, H. Chen, Q. Ye, H.T. Ng, J. Han, M. Meyyappan, *The Fabrication and Electrochemical Characterization of Carbon Nanotube Nanoelectrode Arrays*, Journal of Materials Chemistry, 14 (2004) 676-684.

[Kom00A] K. Komatsu, K. Fujiwara, T. Tanaka, Y. Murata, *The Fullerene Dimer C_{120} and Related Carbon Allotrope*, Carbon, 38 (2000) 1529-1534.

[Kom00B] K. Komatsu, K. Fujiwara, Y. Murata, *The Fullerene Cross-dimer C_{130}: Synthesis and Properties*, Chemical Communications, 17 (2000) 1583-1584.

[Kom98] K. Komatsu, G.-W. Wang, Y. Murata, T. Tanaka, K. Fujiwara, K. Yamamoto, M. Saunders, *Mechanochemical Synthesis and Characterization of the Fullerene Dimer, C_{120}*, Journal of Organic Chemistry, 6 (1998) 9358-9366.

[Koo06] F.B. Kooistra, V.D. Mihailetchi, L.M. Popescu, D. Kronholm, P.W.M. Blom, J.C. Hummelen, *New C_{84} Derivative and Its Application in a Bulk Heterojunction Solar Cell*, Chemistry of Materials, 18 (2006) 3068-3073.

[Kra98A] M. Krause, L. Dunsch, G. Seifert, P.W. Fowler, A. Gromov, W. Krätschmer, R. Gutierez, D. Porezag, T. Frauenheim, *Vibrational Signatures of Fullerene Oxides*, Journal of the Chemical Society, Faraday Transactions, 94 (1998) 2287-2294.

[Kra98B] M. Krause, L. Dunsch, G. Seifert, A. Ayuela, A. Gromov, W. Kraetschmer, R. Gutierrez, D. Porezag, T. Frauenheim, *Raman and Infrared Signatures of $C_{120}O$: Experiments and Theoretical Predictions*, Molecular Nonostructures: Proceedings of the 11th International Winterschool, Kirchberg, Austria, H. Kuzmany, J. Fink, M. Mehring, S. Roth (Eds.), Singapore: World Scientific: 1998, 101-105.

[Kud02] T. Kudo, Y. Akimoto, K. Shinoda, B. Jeyadevan, K. Tohji, T. Nirasawa, M. Waelchli, W. Krätschmer, *Characterization and Structures of Dimeric*

C_{70} oxides, $C_{140}O$, Synthesized with Hydrothermal Treatment, Journal of Physical Chemistry B, 106 (2002) 4383-4389.

[Lan07A] M. Lang (Ed.), *Progress in Fullerene Research*, New York: Nova Science Publishers, 2007.

[Lan07B] F. Langa, J.-F. Nierengarten, *Fullerenes: Principles and Applications*, London (et al.): Royal Society of Chemistry, 2007.

[Laz04] V. Lazarescu, *Carbon Nanotube Electrodes*, Dekker Encyclopedia of Nanoscience and Nanotechnology, Volume 1, J.A. Schwarz, C.I. Contescu, K. Putyera (Eds.), New York, Basel: Marcel Dekker, Inc., 2004.

[Leb00A] S. Lebedkin, W.E. Hull, A. Soldatov, B. Renker, M.M. Kappes, *Structure and Properties of the Fullerene Dimer C_{140} Produced by Pressure Treatment of C_{70}*, Journal of Physical Chemistry B, 104 (2000) 4101-4110.

[Leb00B] S. Lebedkin, W.E. Hull, A. Soldatov, B. Renker, M.M. Kappes, *Dimerization of C_{70} Under High Pressure: Thermal Dissociation and Photophysical Properties of the Dimer C_{140}*, Molecular Nonostructures, Proceedings of the 14th International Winterschool on Electronic Properties of Novel Materials Kirchberg, Austria, H. Kuzmany, S. Roth (Eds.), AIP Conference Proceedings, 544 (2000) 77-80.

[Leb95] S. Lebedkin, S. Ballenweg, J. Gross, R. Taylor, W. Krätschmer, *Synthesis of $C_{120}O$: A New Dimeric [60]Fullerene Derivative*, Tetrahedron Letters, 36 (1995) 4971-4974.

[Leb98] S. Lebedkin, A. Gromov, S. Giesa, R. Gleiter, B. Renker, H. Rietschel, W. Krätschmer, *Raman Scattering Study of C_{120}, a C_{60} Dimer*, Chemical Physics Letters, 285 (1998) 210-215.

[Len08] M. Lenes, G.J.A.H. Wetzelaer, F.B. Kooistra, S.C. Veenstra, J.C. Hummelen, P.W.M. Blom, *Fullerene Bisadducts for Enhanced Open-circuit Voltages and Efficiencies in Polymer Solar Cells*, Advanced Materials, 20 (2008) 2116-2119.

[Li02] J. Li, A. Cassell, L. Delzeit, J. Han, M. Meyyappan, *Novel Three-Dimensional Electrodes: Electrochemical Properties of Carbon Nanotube Ensembles*, Journal of Physical Chemistry B, 106 (2002) 9299-9305.

[Lin04] Y. Lin, W. Yantasee, F. Lu, J. Wang, M. Musameh, Y. Tu, Z. Ren, *Biosensors Based on Carbon Nanotubes*, Dekker Encyclopedia of Nanoscience and Nanotechnology, Volume 1, J.A. Schwarz, C.I. Contescu, K. Putyera (Eds.), New York, Basel: Marcel Dekker, Inc., 2004.

[Loi06] A. Loiseau, P. Launois, P. Petit, S. Roche, J.-P. Salvetat (Eds.), *Understanding Carbon Nanotubes: From Basics to Applications*, Berlin (et al.): Springer, 2006.

[Mau03] G. Maurin, F. Henn, *Electrochemical Intercalation of Lithium into Multi Wall Carbon Nanotubes*, Dekker Encyclopedia of Nanoscience and Nanotechnology, Volume 10, H.S. Nalwa (Ed.), New York, Basel: Marcel Dekker, Inc., 2003.

[Mer05] A. Merkoçi, M. Pumera, Xavier Llopis, B. Pérez, M. del Valle. S. Alegret, *New Materials for Electrochemical Sensing VI: Carbon Nanotubes*, Trends in Analytical Chemistry, 24 (2005) 826-838.

[Mey05] M. Meyyappan (Ed.), *Carbon Nanotubes: Science and Applications*, Boca Raton, Fla. (et al.): CRC Press, 2005.

[Mou05] S.E. Moulton, A.I. Minett, G.G. Wallace, *Carbon Nanotube Based Electronic and Electrochemical Sensors – Review*, Sensor Letters, 3 (2005) 183-193.

[Muk01] K. Mukhopadyay, C.D Dwivedi, G.N. Mathur, *Quality Assessment of Fullerene Samples Using Thermal Technique*, Journal of Thermal Analysis and Calorimetry, 64 (2001) 765-771.

[Mur03] Y. Murata, A. Han, K. Komatsu, *Mechanochemical Synthesis of a Novel C_{60} Dimer Connected by a Germanium Bridge and a Single Bond*, Tetrahedron Letters, 44 (2003) 8199-8201.

[Nub96] B. Nuber, A. Hirsch, *A New Route to Nitrogen Heterofullerenes and the First Synthesis of $(C_{69}N)_2$*, Chemical Communications, 12 (1996) 1421-1422.

[Olm99] M.M. Olmstead, D.A. Costa, K. Maitra, B.C. Noll, S.L. Phillips, P.M. Van Calcar, A.L. Balch, *Interaction of Curved and Flat Molecular Surfaces. The Structures of Crystalline Compounds Composed of Fullerene (C_{60}, $C_{60}O$, C_{70}, and $C_{120}O$) and Metal Octaethylporphyrin Units*, Journal of the American Chemical Society, 121 (1999) 7090-7097.

[Osa96] S. Osawa, E. Osawa, M. Harada, *Internal Rotation in the Singly Bonded Dimers of Substituted C_{60}. A Molecular Lever*, Journal of Organic Chemistry, 61 (1996) 257-265.

[Par06] S. Park, H. Boo, T.D. Chung, *Electrochemical Non-enzymatic Glucose Sensors*, Analytica Chimica Acta, 556 (2006) 46-57.

[Pen97] S.G. Penn, D.A. Costa, A.L. Balch, C.B. Lebrilla, *Analysis of C_{60} Oxides and $C_{120}O_n$ (n = 1,2,3) Using Matrix Assisted Laser Desorption-ionization Fourier Transform Mass Spectrometry*, International Journal of Mass Spectrometry and Ion Processes, 169/170 (1997) 371-386.

[Pun08] N. Punbusayakul, L.J. Ci, S. Talapatra, W. Surareungchai, P.M. Ajayan, *Ultralong Aligned Multi-walled Carbon Nanotube for Electrochemical Sensing*, Journal of Nanoscience and Nanotechnology, 8 (2008) 2085-2090.

[Rei04] S. Reich, C. Thomsen, J. Maultzsch, *Carbon Nanotubes: Basic Concepts and Physical Properties*, Weinheim: Wiley-VCH, 2004.

[Res01] M.R. Resmi, S. Ma, R. Caprioli, T. Pradeep, *$C_{120}O_n$ from $C_{60}Br_{24}$*, Chemical Physics Letters, 333 (2001) 515-521.

[Rot05] S.V. Rotkin, S. Subramoney (Eds.), *Applied Physics of Carbon Nanotubes: Fundamentals of Theory, Optics and Transport Devices*, Berlin (et al.): Springer, 2005.

[Roy04] The Royal Society & The Royal Academy of Engineering, *Nanoscience and Nanotechnologies: Opportunities and Uncertainties*, www.nanotec.org.uk/index.htm (lastly verified February 2009).

[Roy06] S. Roy, H. Vedala, W. Choi, *Vertically Aligned Carbon Nanotube Probes for Monitoring Blood Cholesterol*, Nanotechnology, 17 (2006) 14-18.

[Sai98] R. Saito, G. Dresselhaus, M.S. Dresselhaus, *Physical Properties of Carbon Nanotubes*, Singapore: World Scientific, 1998.

[Sch95] G. Schick, K.-D. Kampe, A. Hirsch, *Reaction of [60]Fullerene with Morpholine and Piperidine: Preferred 1,4-Additions and Fullerene Dimer Formation*, Chemical Communications, (1995) 2023.

[Seg00] J.L. Segura, N. Martín, *[60]Fullerene Dimers*, Chemical Society Reviews, 29 (2000) 13-25.

[Sen04] S. Sensfuss, M. Al-Ibrahim, A. Konkin, G. Nazmutdinova, U. Thokhavets, G. Gobsch, D.A.M. Egbe, E. Klemm, H.-K. Roth, *Characterisation of Potential Donor Acceptor Pairs for Polymer Solar Cells by ESR, Optical and Electrochemical Investigations*, Organic Photovoltaics IV, Z.H. Kafafi, P.A. Lane (Eds.), Bellingham: Proceedings of SPIE, 5215 (2004) 129-140.

[Shi04] H. Shimotani, N. Dragoe, K. Kitazawa, *Fullerene Dimers*, Encyclopedia of Nanoscience and Nanotechnology, 3 (2004) 529-544.

[Sin06] N. Sinha, J. Ma, J. Yeaow, *Carbon Nanotube-Based Sensors*, Journal of Nanoscience and Nanotechnology, 6 (2006) 573-590.

[Sma01] R.E. Smalley, *Carbon Nanotubes: Synthesis, Structure, Properties and Applications*, Berlin (et al.): Springer, 2001.

[Smi95] A.B. Smith III., H. Tokuyama, R.M. Strongin, G.T. Furst, W.J. Romanow, B.T. Chait, U.A. Mirza, I. Haller, *Synthesis of Oxo- and*

Methylene-Bridged C_{60} Dimers, the First Well-Characterized Species Containing Fullerene-Fullerene Bonds, Journal of the American Chemical Society, 117 (1995) 9359-9360.

[Smi96] A.B. Smith III., R.M. Strongin, L. Brard, G.T. Furst, J.H. Atkins, W.J. Romanow, M. Saunders, H.A. Jiménez-Vázquez, K.G. Owens, R.J. Goldschmidt, *Synthesis and Characterization of the First $C_{70}O$ Epoxides: Utilization of ^{3}He NMR in Analysis of Fullerene Derivatives*, Journal of Organic Chemistry, 61 (1996) 1904-1905.

[Sol99] S.P. Solodovnikov, B.L. Tumanskii, V.V. Bashilov, V.I. Sokolov, S.F. Lebedkin, W. Krätschmer, *EPR Study of Cation Radicals of Fullerene Dimers C_{120} and $C_{120}O$*, Chemical Physics Letters, 303 (1999) 387-390.

[Sto03] M. Stoll, P.M. Rafailov, W. Frenzel, C. Thomsen, *Electrochemical and Raman Measurements on Single-walled Carbon Nanotubes*, Chemical Physics Letters, 375 (2003) 625-631.

[Tag02] N. Tagmatarchis, G.S. Forman, A. Taninaka, H. Shinohara, *Cross-Fullerene Dimers ($(C_{60})(C_{70})$): Solid-State Synthesis, Characterization and Mechanism*, Synlett, (2002) 235-238.

[Tak01] H. Takahashi, E. Matsubara, A. Kasuya, Y. Akimoto, T. Kudo, B. Jeyadevan, K. Tohji, *Efficient and Simple Preparation Method for Dimeric Fullerene Oxides*, Proceedings of the International Symposium on Cluster Assembled Mater, IPAP Conference Series, 3 (2001) 118-122.

[Tak98] H. Takahashi, K. Tohji, I. Matsuoka, B. Jeyadevan, A. Kasuya, S. Ito, Y. Nishina, T. Nirasawa, *Extraction and Purification of Dimeric Fullerene Oxides from Fullerene Soot*, Journal of Physical Chemistry B, 102 (1998) 5438-5443.

[Tan05] H. Tang, J. Chen, S. Yao, L. Nie, Y. Kuang, Z. Huang, D. Wang, Z. Ren, *Deposition and Electrocatalytic Properties of Platinum on Well-Aligned Carbon Nanotube (CNT) Arrays for Methanol Oxidation*, Materials Chemistry and Physics, 92 (2005) 548-553.

[Tan06] H. Tang, J. Chen, L. Nie, S. Yao, Y. Kuang, *Electrochemical Oxidation of Glutathione at Well-aligned Carbon Nanotube Array Electrode*, Electrochimica Acta, 51 (2006) 3046-3051.

[Tan08] C.K. Tan, K.P. Loh, T.T.L. John, *Direct Amperometric Detection of Glucose on a Multiple-branching Carbon Nanotube Forest*, Analyst, 133 (2008) 448-451.

[Tay98A] R. Taylor, A. Pénicaud, N.J. Tower, *Matrix Isolation of Fullerene-derived CO_2 at Ambient Temperature*, Chemical Physics Letters, 295 (1998) 481-486.

[Tay98B] R. Taylor, M.P. Barrow, T. Drewello, *C_{60} Degrades to $C_{120}O$*, Chemical Communications, 22 (1998) 2497-2498.

[Tia00] W.Q. Tian, A.M. Ren, J.K. Feng , J.G. Guo, C.C. Sun, *Theoretical Study on the Structures and Electronic Spectra of $C_{120}O_n$ (n = 1,2)*, International Journal of Quantum Chemistry, 79 (2000) 291-307.

[Tra08] J.E. Trancik, S. Calabrese Barton, J. Hone, *Transparent and Catalytic CarbonNanotube Films*, Nano Letters, 8 (2008) 982-987.

[Tro06] M. Trojanowicz, *Analytical Applications of Carbon Nanotubes: A Review*, Trends in Analytical Chemistry, 25 (2006) 480-489.

[Tsy04] D. Tsyboulski, D. Heymann, S.M. Bachilo, L.B. Alemany, R.B.Weisman, *Reversible Dimerization of [5,6]-$C_{60}O$*, Journal of the American Chemical Society, 126 (2004) 7350 -7358.

[Tu03] Y. Tu, Y. Lin, Z.F. Ren, *Nanoelectrode Arrays Based on Low Site Density Aligned Carbon Nanotubes*, Nano Letters, 3 (2003) 107.

[Tu05] Y. Tu, Y. Lin, W. Yantasee, Z. Ren, *Carbon Nanotubes Based Nanoelectrode Arrays: Fabrication, Evaluation, and Application in Voltammetric Analysis*, Electroanalysis, 17 (2005) 79-84.

[Wan05] J. Wang, *Carbon-Nanotube Based Electrochemical Biosensors: A Review*, Electroanalysis, 17 (2005) 7-14.

[Wan07] J. Wang, X. Sun, X. Cai, Y. Lei, L. Song, S.S. Xie, *Nonenzymatic Glucose Sensor Using Freestanding Single-Wall Carbon Nanotube Films*, Electrochemical and Solid-State Letters, 10 (2007) J58-J60.

[Wan08] X.B. Wang, K. Matheis, I.N. Ioffe, A.A. Goryunkov, J. Yang, M.M. Kappes, L.S. Wang, *High Resolution and Low-temperature Photoelectron Spectroscopy of an Oxygen-linked Fullerene Dimer Dianion: $C_{120}O_2^-$*, Journal of Chemical Physics, 128 (2008) 114370.

[Wei08] S. Wei, W.P. Kang, J.L. Davidson, J.H. Huang, *Supercapacitive Behavior of CVD Carbon Nanotubes Grown on Ti Coated Si Wafer*, Diamond and Related Materials, 17 (2008) 906-911.

[Wie03] M.M. Wienk, J.M. Kroon, W.J.H. Verhees, J. Knol, J.C. Hummelen, P.A. van Hal, R.A.J. Janssen, *Efficient Methano[70]Fullerene-MDMO-PPV Bulk Heterojunction Photovoltaic Cells,* Angewandte Chemie/International Edition, 42 (2003) 3371-3374.

[Wie93] H.G. Wiedemann, G. Bayer, *Thermoanalytical Investigations of Fullerenes*, Thermochimica Acta, 214 (1993) 85-91.

[Wil06] G.G. Wildgoose, C.E. Banks, H.C. Leventis, R.G. Compton, *Chemically Modified Carbon Nanotubes for Use in Electroanalysis*, Microchimica Acta, 152 (2006) 187-214.

[Win06] K. Winkler, A.L. Balch, W. Kutner, *Electrochemically Formed Ffullerene-based Polymeric Films*, Journal of Solid State Electrochemistry, 10 (2006) 761-784.

[Xie07] J. Xie, S. Wang, L. Aryasomayajula, V.K. Varadan, *Platinum Decorated Carbon Nanotubes for Highly Sensitive Amperometric Glucose Sensing*, Nanotechnology, 18 (2007) 65503-65600.

[Xie08] J. Xie, S. Wang, L. Aryasomayajula, V.K. Varadan, *Effect of Nanomaterials in Platinum-decorated Carbon Nanotube Paste-based Electrodes for Amperometric Glucose Detection*, Journal of Materials Research, 23 (2008) 1457-1465.

[Yam02] S. Yamauchi, T. Funayama, Y. Ohba, P. Paul, C.A. Reed, K. Fujiwara, K. Komatsu, *Direct Observation of Localized Excitation in the Lowest Excited Triplet State of Fullerene Dimers C_{120} and $C_{120}O$ by Means of Time-resolved Electron Paramagnetic Resonance*, Chemical Physics Letters, 363 (2002) 199-203.

[Ye03] J.-S. Ye, Y. Wen, W. Dezhang, L. Gan, G. Xu, F.-S. Sheu, *Selective Voltammetric Detection of Uric Acid in the Presence of Ascorbic Acid at Well-Aligned Carbon Nanotube Electrode*, Electroanalysis, 15 (2003) 1693-1698.

[Ye04] J.S. Ye, Y. Wen, W.D. Zhang, L.M. Gan, G.Q. Xu, F.S. Sheu, *Nonenzymatic Glucose Detection Using Multi-walled Carbon Nanotube Electrodes*, Electrochemistry Communications, 6 (2004) 66-70.

[Ye05A] J.S. Ye, X. Liu, H.F. Cui, W.D. Zhang, F.S. Sheu, T.M. Lim, *Electrochemical Oxidation of Multi-walled Carbon Nanotubes and Its Application to Electrochemical Double Layer Capacitors*, Electrochemistry Communications, 7 (2005) 249-255.

[Ye05B] J.S. Ye, H.F. Cui, X. Liu, T.M. Lim, W.D. Zhang, F.S. Sheu, *Preparation and Characterization of Aligned Carbon Nanotube-ruthenium Oxide Nanocomposites for Supercapacitors*, Small, 1 (2005) 560-565.

[Ye06] J.S. Ye, Y. Wen, W.D. Zhang, H.F. Cui, G.Q. Xu, F.S. Sheu, *Electrochemical Functionalization of Vertically Aligned Carbon Nanotube Arrays with Molybdenum Oxides for the Development of a*

Surface-charge-controlled Sensor, Nanotechnology, 17 (2006) 3994-4001.

[Yos99] M.Yoshida, F. Sultana, N. Uchiyama, T. Yamada and M. Iyoda, *Efficient Synthesis of Fullerene Dimers Containing a Fluoroalkyl Group*, Tetrahedron Letters, 40 (1999) 735-736.

[Yun06] Y.H. Yun, V. Shanov, M.J. Schulz, Z.Y. Dong, A. Jazieh, W.R. Heineman, H.B. Halsall, D.K.Y. Wong, A. Bange, Y. Tu, S. Subramaniam, *High Sensitivity Carbon Nanotube Tower Electrodes*, Sensors and Actuators B, 120 (2006) 298-304.

[Zha03] R.-S. Zhai, A. Das, C.-C. Han, T. Canteenwal, L.Y. Chiang, T.J. Chuang, *Stable Poly(fullerene oxide) Thin Films Derived from Hexanitro[60]fullerene*, Journal of Materials Chemitry, 13 (2003) 167-169.

[Zha04] Y. Zhao, Z. Chen, H. Yuan, X. Gao, L. Qu, Z. Chai, G. Xing, S. Yoshimoto, E. Tsutsumi, K. Itaya, *Highly Selective and Simple Synthesis of C_{2m}-X-C_{2n} Fullerene Dimers*, Journal of the American Chemical Society, 126 (2004) 11134-11135.

[Zha06] J. Zhang, J.K. Porfyrakis, J.M.R. Sambrook, A. Ardavan, G.A.D. Briggs, *Determination of the Thermal Stability of the Fullerene Dimers C_{120}, $C_{120}0$, and $C_{120}0_2$*, Journal of Physical Chemistry B, 110 (2006) 16979-16981.

[Zha08A] H. Zhang, G.P. Cao, Y.S. Yang, Z.N. Gu, *Capacitive Performance of an Ultralong Aligned Carbon Nanotube Electrode in an Ionic Liquid at 60 Degrees C*, Carbon, 46 (2008) 30-34.

[Zha08B] H. Zhang, G.P. Cao, Y.S. Yang, Z.N. Gu, *Comparison Between Electrochemical Properties of Aligned Carbon Nanotube Array and Entangled Carbon Nanotube Electrodes*, Journal of the Electrochemical Society, 155 (2008) K19-K22.

Appendix

Analytical Data

In the following paragraphs, analytical data of $C_{120}O$, $C_{140}O$, $C_{130}O$, **1** ($C_{120}OR´$), and **2** ($C_{120}OR´´$) are given.

$C_{120}O$: HPLC (Buckyprep) retention times [min]: 7.15 (1 mL/min toluene/ODCB (7/3, v/v) elution); 22.7 (1 mL/min toluene elution). MALDI-TOF MS (DCTB matrix) m/z: 1456.768 (M^-). IR (KBr) ν [cm^{-1}]: 1461 (m), 1455 (m), 1424 (m), 1383 (m), 1257 (m), 1217 (m), 1186 (m), 1179 (m), 1163 (m), 1098 (s), 1059 (w), 1031 (s), 1014 (s), 958 (m), 848 (s), 806 (m), 763 (m), 745 (m), 709 (m), 668 (m), 605 (m), 587 (w), 572 (s), 563 /m), 549 (s), 526 (s), 478 (s). UV-vis (ODCB) λ_{max} [nm]: 294, 326, 418 (shoulder), 696 (weak).

$C_{140}O$ (isomeric mixture): HPLC (Buckyprep) retention times [min]: 12.95, 14.11 (1 mL/min toluene/ODCB (7/3, v/v) elution); 60.4, 62.9, 66.7, 72.2, (1 mL/min toluene elution). MALDI-TOF MS (DCTB matrix) m/z: 1696.792 (M^-). IR (KBr) ν [cm^{-1}]: 1568 (w), 1566 (w), 1454 (s), 1429 (s), 1313 (w), 1247 (w), 1214 (w), 1151 (w), 1122 (m), 1074 (m), 1033 (m), 1014 (m), 935 (w), 838 (w); 794 (m), 669 (m), 658 (w), 638 (w), 576 (m), 534 (m), 469 (w), 455 (w). UV-vis (ODCB) λ_{max} [nm]: 284, 314, 342, 406, 462.

$C_{130}O$ (isomeric mixture): HPLC (Buckyprep) retention times [min]: 9.3, 9.7 (1 mL/min toluene/ODCB (70/30, v/v) elution); 38.1, 40.2, 42.1 (1 mL/min toluene elution). MALDI-TOF MS (DCTB matrix) m/z: 1576.381 (M^-). IR (KBr) ν [cm^{-1}]: 1732 (m), 1699 (w), 1650 (m), 1633 (s), 1496 (m), 1455 (s), 1430 (s), 1376 (w), 1261 (w), 1201 (w), 1180 (w), 1153 (w), 1062 (s), 1027 (s), 842 (w), 794 (w), 746 (m), 698 (s), 576 (m), 526 (s). UV-vis (ODCB) λ_{max} [nm]: 294, 332 (very weak and broad shoulder).

1 ($C_{120}OR´$, isomeric mixture): HPLC (Buckyprep) retention times [min]: 12.3, 13.0 (1 ml/min toluene elution); 352, 364, 380, 409, 446 (0.1 mL/min toluene/ cyclohexane (1/1, v/v) elution). IR (KBr) υ [cm^{-1}]: 1737 (s), 1627 (m), 1598 (w), 1492 (m), 1456 (s), 1444 (s) 1432 (s), 1371 (m), 1330 (w), 1245 (m), 1155 (m), 1101 (m), 1031 (s), 964 (w), 848 (m), 804 (m), 765 (m), 702 (m), 547 (m), 526 (s), 478 (m), 403 (w). MALDI-TOF MS (DCTB matrix) m/z: 1646.836 (M^-). ^{1}H-NMR: ($CDCl_3$/TMS, 400 mHz): δ [ppm]: 7.0-7.52 (phenyl; 5 H), 3.61, 3.68 ($OC\underline{H}_3$; 3 H), 2.36 ($C\underline{H}_2CO_2Me$; 2 H), 1.56 ($C\underline{H}_2CH_2CO_2Me$; 2 H), 1.25 ($PhCC\underline{H}_2$; 2 H). UV-vis (ODCB) λ_{max} [nm]: 287, 325, 368 (shoulder), 418 (shoulder), 689 (weak).

2 ($C_{120}OR´´$, isomeric mixture): HPLC (Buckyprep) retention times [min]: 9.3, 9.6 (1 mL/min toluene elution); 243, 246, 255, 266 (0.1 mL/min toluene/cyclohexane (1/1, v/v) elution). MALDI-TOF MS (DCTB matrix) *m*/z: 1726.876 (M^-). IR (KBr) *υ* [cm^{-1}]: 1743 (s), 1456 (m), 1452 (m), 1427 (m), 1373 (w), 1267 (m), 1240 (s), 1182 (m), 1099 (m), 1065 (w), 1034 (s), 964 (w), 849 (m), 744 (m), 577 (w), 550 (w), 526 (s). ^{1}H-NMR: ($CDCl_3$/TMS, 400 mHz): δ [ppm]: 4.4, 3.54, 1.54, 1.27, 0.88. UV–vis (ODCB) λ_{max} [nm]: 285, 326, 416 (shoulder), 703 (weak).